The Effects of Hydrogen Ion Irradiation on Mechanical Properties of SiC-Based Materials Using an MC40 Cyclotron

By Philip Peter George Baldock

A Thesis Submitted to the University of Birmingham for the Degree of Masters of Research

Department of Metallurgy and Materials

University of Birmingham

November 2013

ABSTRACT

An MC40 cyclotron was outfitted for performing focused ion beam exposure to materials that are being investigated for use in the nuclear industry. Apparatus in the form of a vacuum chamber with internal heating element and cooled aperture system was installed and used successfully. Several silicon carbide based materials were processed into samples and tested mechanically as received. Analogous samples were prepared and exposed to proton irradiation either as 1 μA per cm^2 for 5 hours in air at 400°C, or 0.3 μA per cm^2 for 4 hours in vacuum at 85 °C. After irradiation these were tested mechanically by the same methods as non-irradiated samples so that changes between non-irradiated and irradiated samples could be investigated. Computational models were constructed to estimate the temperatures reached in the samples during irradiation and the TRIM software was used to model displacement damage through the materials tested. Within the accuracy of the experiments performed, no significant change in flexural strength of composite materials was observed but a significant increase was found in the tensile strength of KD-1 fibres after irradiation.

ACKNOWLEDGEMENTS

Aspects of this work required a diverse range of skills, many of which could not be taught to the author over the timescale in which this work was done. Shuang Zhao of the National University of Defence Technology (Hunan province, China) manufactured the composite materials tested (both PCS and LPVCS) and KD-1 fibres. Dennis Formosa operated the nanoindenter. Chris Simpson provided training for the Vickers microhardness indenter and Chris Cooper provided training for use of the fibre testing machines and the scanning electron microscope. My supervisors Brian Connolly and Clive Ponton provided invaluable guidance, support and insight throughout the project.

CONTENTS

3. MATERIALS INVESTIGATED AND EXPERIMENTAL SETUP

9. APPENDICES

LIST OF ILLUSTRATIONS

Appendix Figures

LIST OF TABLES

Appendix Tables

1. INTRODUCTION

1.1. Program Objectives

The scope of this project includes the development of a facility for ion irradiation to simulate damage caused by the radiation conditions in a nuclear reactor and the development of testing methods for numerous SiC based materials to investigate different aspects of the behaviour of the composites intended for use as cladding in the nuclear industry. The collection of useful data from irradiation experiments requires knowledge of both the dose rate and the temperature during irradiation [16, 19, 25]. Developing the setup consisted of a computational element in calculating the dose rate (in displacements per atom or dpa) using the TRIM code [57] and particle ranges using the SRIM code for materials tested and in theoretical modelling of the temperature distribution in the sample during irradiation (experimental determination of this directly was prohibitively difficult with the resources available). The objective of mechanical testing was to look for changes in mechanical properties between non-irradiated and irradiated specimens. Non-irradiated SiC-based materials were prepared and mechanically tested using the equipment available. Equivalent samples were then prepared and subsequently irradiated and tested by the same methods – looking for discrepancies between these data was the objective rather than accurate determination of mechanical properties themselves in both states (which is more difficult). From the need for thin composite samples for flexural testing to a novel approach to clamping nuclear-grade fibres for tensile testing, the mechanical tests of this project often had to use non-standard sample dimensions and testing equipment better suited to other materials. Mechanical testing of samples were

utilised as best as possible to the capabilities of the equipment available in order to establish the feasibility of each method for further study in the area of fine ceramic fibre composites. Materials investigated were chosen so that they would provide information about likely fibre material for reinforcement of SiC/SiC composites and material similar to matrix material to represent a composite matrix (this concept is outlined in figure 1). Irradiation was performed using a proton beam from an MC40 cyclotron. Table 1 outlines the specific materials tested in this study. Off-the-shelf SiC/SiC composites are prohibitively expensive for a project of this kind so before KD-1 fibre composite availability was secured it was expected that actual mechanical testing of SiC fibre composites would not be feasible. Figure 1 illustrates the original program concept, where comparing mechanical tests between irradiated and non-irradiated SiC based fibres and bulk materials (sintered α-SiC) would permit inference about their behaviour as a composite system. In practice there are numerous difficulties with attempting a quantitative version of this approach, for instance the fibre-matrix interface properties play a critical role [24, 41-43] in the mechanical properties of a composite as a whole and cannot be evaluated from testing fibre and matrix alone. A large body of work exists [31, 32, 41-43] exploring fibre-matrix interphase property changes under irradiation so that insight into composite material behaviour under irradiation can still be gained qualitatively from testing fibres and matrix material separately (e.g. [10, 19, 25]).

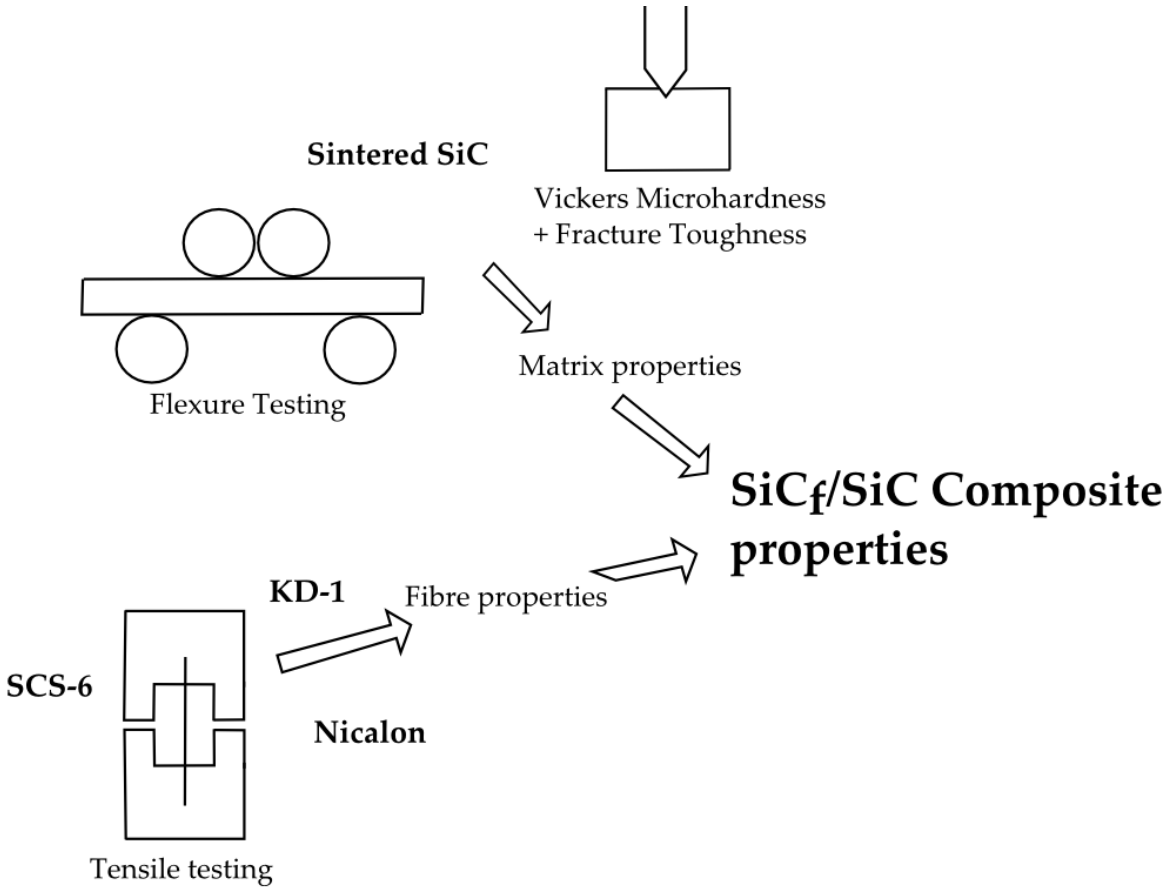

Figure 1
As illustrated in the diagram, the original concept forthis project was to infer property changes in SiC/SiC fibre composites after ion irradiation by mechanically testing irradiated and non-irradiated aerospace grade SiC fibres (and eventually nuclear grade SiC fibres) and bulk SiC material (see section 3.4.1. for details of mechanical tests performed).

Table 1
Work matrix of all mechanical testing and x-ray tomography performed that provided useful data (notched toughness tests were attempted but found to be impractical with thin samples).

Material	**Tension**	**4-Point Flexure**	**Vickers Indents**	**Nanohardness Indents**	**X-Ray Tomography**
SCS-6 fibre	X				
Nicalon nuclear grade fibre	X				
KD-1 nuclear grade fibre	X				
Hot pressed α-SiC			X		
Pressureless sintered α-SiC		X	X		
Polycarbosilane (PCS) KD-1 Fibre Composite		X		X	X
LPVCS KD-1 Fibre Composite		X		X	X

1.2. The Need for Advanced Materials in Proposed Generation IV Nuclear Reactors

Many projects are currently funded in the nuclear energy community for the investigation into the potential of a number of new reactor schemes that may provide energy effectively if they can be commercialised. These include fusion, molten salt reactors, accelerator driven fast reactors and many others (see e.g. Snead [1-10, 39, 40]). Conditions during operation for reactor components are problematic for modern materials in several respects depending on application: in breeders, accelerator driven spallation devices and for fusion, the radiation damage sustained over the lifetime of a reactor is as much as two orders of magnitude more than those conditions prevalent in Gen I reactors (see e.g. the Triple Beam conference at Lawrence Livermore (2009)[11]). Designs involving molten salts such as the TAURO concept [2, 4, 8, 12] not only require a high radiation resistance but a high corrosion resistance. A higher temperature of operation leads to higher thermodynamic efficiency, hence creep resistance at higher operating temperatures is also important for many Gen IV applications [5-7]. Several materials are under investigation for use in these challenging environments, one of which is SiC in the form of woven fibre composites. SiC composites have progressed greatly over the past 20 years (compare, for instance, Snead et al (1998)[24] reporting significant changes in mechanical properties at ~1 dpa (or similarly) [1,2, 31] to modern composites e.g. Hinoki et al (2002) [23] or Katoh et al (2010) [35]) to the point of being near application readiness (e.g. Katoh et al (2007)[8] or [14-16] etc.). Modern composites demonstrate a high radiation resistance as well as minimal reduction of material properties at elevated temperatures [30, 31]. Table 2, taken directly from the Lawrence Livermore workshop concerning nuclear materials research,

summarises the proposed operating conditions for the new reactor design proposals relative to Gen I reactors.

Table 2
Taken directly from Lawrence Livermore workshop [11] concerning nuclear materials research, summarising the relative operating conditions of materials required for future reactsors. Helium concentration combined with radiation damage of the scale relevant for Generation IV reactors has yet to be realised for thick samples.

	Fission (Gen I)	**Fission (Gen IV)**	**Fusion (DEMO/PROTO)**	**Spallation (ADS)**
Structural alloy Tmax	<300 °C	300–1,000 °C	550–1,000 °C	140–600 °C
Max dose for core internal structures	~1 dpa	~30–200 dpa	~150 dpa	50–100 dpa
Max helium concentration	0.1 appm	~3–40 appm	~1,500 appm (~10,000 appm for SiC)	~5,000 appm/fpy
Max hydrogen concentration			~6,750 appm	50,000–100,000 appm/fpy
Neutron Energy Emax	<1–2 MeV	<1–3 MeV	<14 MeV	Several hundred MeV

Potential components intended for manufacture include control rod sleeves (e.g. Snead et al)[10] in very high pressure reactors (VHPR) as well as blanket modules for the main 3 competing fusion blanket designs [2]: DREAM (Drastically Easy Maintenance) and ARIES, which use a helium coolant and solid Li_2O pebbles and the TAURO liquid lead-lithium system (for which SiC composites have performed well, e.g. Riccardi et al [7] or [40]). SiC composites were also being researched for use in fuel cladding as a component of the TRISO (tri-structural isotropic) fuel pellet system [10] as part of systems such as the PBMR (pebble bed modular reactor) or more recently the NGNR (next generation nuclear reactor), where a layer of Chemical Vapour Deposited (CVD) SiC provides mechanical stability against outgassing and void-induced swelling in the porous carbon layer

beneath. Figure 2 shows the TRISO concept (a) as well as an SEM cross-section of a TRISO pellet after heavy irradiation (b). SiC is therefore a strong candidate in a reactor system for components requiring mechanical stability under high levels of radiation and temperature.

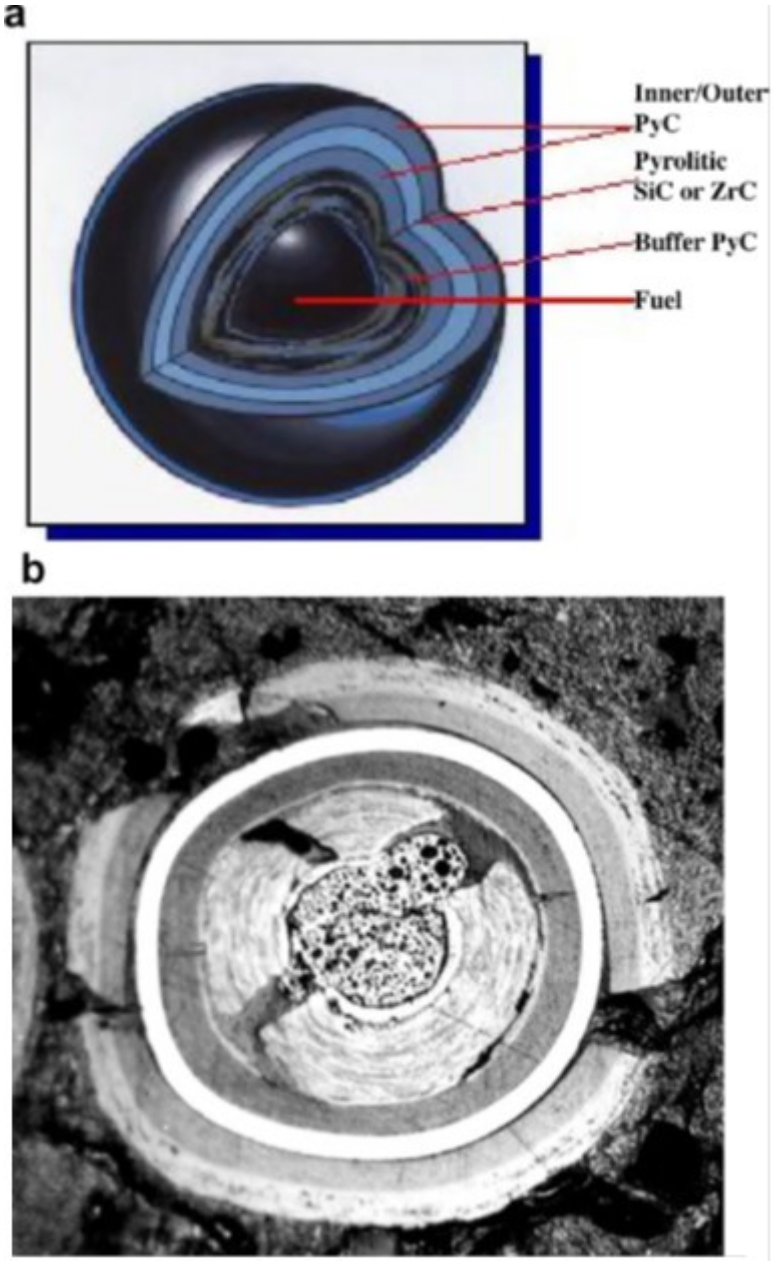

Figure 2
Taken directly from Snead et al (2007) [10], the TRISO fuel pellet system concept (a) and a cross-section of a heavily irradiated TRISO pellet (b). The CVD SiC layer, shown unbroken in white in (b), acts as a seal and source of mechanical integrity for the porous pyrolytic carbon and fuel inside (which cracked due to voidage and outgassing during irradiation).

1.3. SiC Reactor Applications Overview

1.3.1. Specific Requirements for Testing Under Nuclear Reactor Conditions

Most significant amongst the required properties for structural materials within Generation IV nuclear reactors are resistance to high temperatures/creep, corrosion and damage from intense ionising radiation (including void induced swelling and degradation of material properties)[3-10]. The properties of Silicon Carbide based materials thus make them attractive for these applications. However, the primary radiation type in nuclear reactors, fast neutrons, presents many difficulties for directly testing material samples. Firstly, they cannot be focused (so that a large portion of the neutrons from the source are not useful for the experiment) and most of the kinetic energy carried by a particular neutron interacting with a material sample escapes with the neutron (since they interact only rarely)[47]. These characteristics require either a prohibitively high power neutron source or very long exposure times for a material sample to be tested. Neutrons also tend to cause high induced radioactivity (activation) in materials exposed to them (in the case of SiC, this is mostly ^{28}Si transmuting to ^{27}Al, which is a gamma emitter (e.g. Fenici et al (1998)[2] or [1]). By contrast, charged particles are easily focused so that the entire output of a source may be directed onto a small material sample and most of their energy is deposited in the sample, so that exposure times and required source fluences may be greatly reduced. Activation does also occur for incident charged particles but can be less significant per unit dpa [52]. Using an ion beam for testing of components is therefore an attractive concept provided that the differences between neutron and ion radiations are well understood (as discussed in section 2.3.2).

1.3.2. Properties and Suitability of SiC for Gen IV and Fusion Applications

SiC has seen widespread application in high temperature and high corrosion roles (such as cladding, e.g. Bragg-Sitton et al (2013) [14] or [10, 15, 40, 41]). The Young's modulus of SiC is high compared even to other refractory ceramics such as alumina [48-50], retaining material properties and good oxidation resistance up to high temperatures which has facilitated its use in crucibles. SiC also has a high corrosion resistance, so that SiC based fibres are well suited to the reinforcement of materials designed for use in harsh environments. It has over 250 polytypes (e.g. Reidel and Chen (2010) [50]), with the majority of them labelled collectively as "$\boldsymbol{\alpha}$" when produced in bulk for mechanical uses except when a particular polytype is needed; this typically happens when their properties are relevant to the semiconductor industry (since their band gaps differ [49]). The β polytype, however, possesses the properties most sought after in the nuclear energy sector owing to its high radiation resistance compared to α (e.g. Charpentier)(2010)[39, 40]. The β crystal type forms preferentially when crystallised at temperatures below 2100 ^{o}C [40, 50]. It is a Zincblende cubic structure (similar to diamond) and under the correct conditions has a very high resistance to radiation damage [10, 41]. SiC is most resistant in the 1:1 stoichiometric ratio of silicon to carbon. Even small amounts of oxygen present in a SiC-based material can lead to the formation of glassy phases under irradiation which can change the fibre-matrix interphase in the systems for which β-SiC has intended structural applications (fibre composites)[1-4]. Table 3 summarises the conditions required in the ARIES, DREAM and TAURO reactor proposals.

Table 3
Taken directly from Abe et al (2008) [13], comparison of proposed cladding systems studied in the JUPITER-II program.

System	Flibe system	Vanadium alloys/Li	SiC/SiC /He
Candidate structural material	Ferritic, ODS vanadium alloy	(Vanadium alloy) V–4Cr–4Ti	SiC/SiC composite
Coolant	Flibe (He)	Liquid Li	He
Breeding materials	Flibe	Li	Li2O etc.
Typical blanket design	FFHR liquid blanket	ARIES-RS liquid blanket	DREAM gas cooled blanket
Activation	Medium low	Low	Very low
Inlet/outlet	450/550 (700) ◦C	330/610 ◦C	500/800 ◦C
Temperature and heat flux	Medium	High	Medium
Thermal efficiency	37%	45%	50%
Issues for power reactor	Flibe technology Redox control	MHD drop Li technology	Thermal conductivity hermeticity
Materials system issues	Corrosion	Ceramic coating fabrication	H, He production fabrication

In practice it was found to be very difficult with the facilities available (the MC40 cyclotron) to produce radiation doses similar to those expected in the nuclear industry for SiC. Over a reactor lifetime, for example, a cladding component in a generation IV reactor may be exposed to doses from 30-200 dpa [as in table 2]. SiC is a good candidate for development of a setup for radiation degradation research because of its low activation [1-8], potential for irradiation to be performed over a wide variety of temperatures/in atmosphere because of its refractory and oxidation resistant properties, better if not spectacular radiation resistance as compared to many materials [8-10, 13-16]. When a material is bombarded with ions as in this study a small number of its constituent nuclei will interact with beam ions to become radioactive. For materials containing elements such as titanium or iron, the residual radioactivity left after irradiation can be high

enough as to make it unsafe for handling or require prohibitively long periods of time for the radioactivity to fall to safe levels. During this study a thin titanium sheet was trialed for use as a beam energy degrader and exhibited more than 20 times the residual activity of SiC samples tested (200 μSieverts/hour 3 days after irradiation compared to 10 μSieverts/hour 3 days after irradiation for PCS composite samples with similar activities measured for all other irradiated SiC based materials in this study 3 days after irradiation). SiC is far superior to steel in this respect, particularly for long lived radioactivity [2] which is important for reducing the cost of decommissioning reactors. Frequently, depending on conditions during irradiation, SiC samples were tested that become safe to handle (provided appropriate care is taken) over a time period of a week or less.

Several methods of testing and characterisation were pursued over the course of this project. Mechanical testing was performed using flexure, notched toughness, tension, nanohardness and Vickers microhardness methods. Characterisation was performed using X-Ray tomography and optical microscopy. Flexure and notched toughness tests (in 4-point and 3-point bending, respectively) were chosen because it is difficult to grip composite samples for tensile testing. Destructive testing of fibre composite samples in tension permits observations in fibre pullout to be made on the facture surfaces after testing (e.g. [35, 63]. Dogbone specimens are typically used to this end, but these are difficult to manufacture and waste material, which was of limited supply for this project. 4-point flexure has the advantage of giving pure bending during testing over a wide tested area between the internal grips.

The following failure modes are possible for a fibre composite with a crack already initiated (adapted from Dharani)(1990)[20] with a unidirectional weave. Though the quantitative analysis by Dharani would be no longer applicable, local to a fibre bundle in the material the mechanisms of failure for a multidirectional fibre weave should be the same as for a unidirectional weave:

- Extension of a bridged matrix crack (cracking of the matrix parallel to the fibre direction). The predominance of this mode may indicate greater fibre strength when compared to matrix strength.[20]
- Delamination of the matrix from the fibres. This mode is controlled predominantly by the strength of the fibre-matrix interface.(see e.g. Snead [24])
- Fracture of fibres that bridge the original crack.
- Compressive failure of the composite.

Notched Toughness permits changes in fibre bonding strength to be observed as differences in the stress-strain profiles generated during notched toughness testing. This testing method has the added benefit of testing only a very small volume of the material so that 3-point bending in the centre of each separated piece of a composite sample already broken in flexure could be performed with minimal influence from the 4-point flexure break. In practice, it was found to be difficult to implement this because the samples were so thin that the samples were deflected away during testing so that no useful data could be collected from notched toughness testing in this work.

2. LITERATURE REVIEW

2.1. Manufacturing Techniques for Modern Structural SiC Products

2.1.1. Preference for Composites for Structural Applications

The most useful characteristics of SiC, being its retention of material properties at high temperatures and good corrosion and radiation resistance, are offset by those common to ceramic materials that make them difficult to use directly in mechanical applications. Particularly, monolithic SiC has a low toughness. This limits its potential use as a structural material (particularly for nuclear reactors, gas turbine engines, etc.)[49]. Hence research efforts for potential structural applications are primarily directed towards the production of composites, in which typically a group of fine SiC fibres is bonded together in a matrix [1-10].

The production of fibre reinforced composites requires the fibre and matrix to have similar thermal and mechanical properties so that the bonding between them does not fail in operation. There is essentially a trade-off made in composite design with poor bonding between matrix and fibre providing lower modulus but greater toughness and conversely a higher degree of bonding results in superior elastic moduli but lower toughness (Bertrand and Pailler (2004) [5]). If the thin interphase between fibre and matrix is changed during operation, therefore, it can potentially cause drastic changes in the behaviour of the material as a whole [41-44]. Hence for high temperature applications, where significant expansion occurs, if the fibre behaves in a way dissimilar to the matrix (for instance differing coefficients of thermal expansion) it can lead to decoupling and

subsequent change in mechanical properties away from the design criteria of the component. For high radiation damage applications, SiC is also used for the matrix material due to similar considerations (differences in radiation induced swelling between fibre and matrix can also lead to mechanical failure), especially for potential nuclear applications. In advanced SiC composite materials, the matrix-fibre interface is achieved through use of micrometer-scale coatings applied to the fibre. These are also often chosen such that cracks in the matrix of the composite are deflected upon meeting the coating and result in the formation of many smaller local cracks in the matrix, acting to absorb energy and hence increase the toughness of the composite [41-44].

2.1.2. SiC Based Fibres

For aerospace applications, particularly titanium reinforcement, many companies provide SiC fibres with fine metallic cores around which SiC is grown by chemical vapour deposition. This method permits a high degree of control over the axial structure of the deposited material. The Sigma brand fibre produced by TISICS Ltd. [22] (as depicted in the SEM image figure 3) and SCS-6 fibre from Speciality Materials Inc. [23] (as depicted in the SEM image figure 4) are of this type. In these examples, a tungsten filament and a carbon filament (respectively) act as a base for chemical vapour deposition (CVD) of SiC.

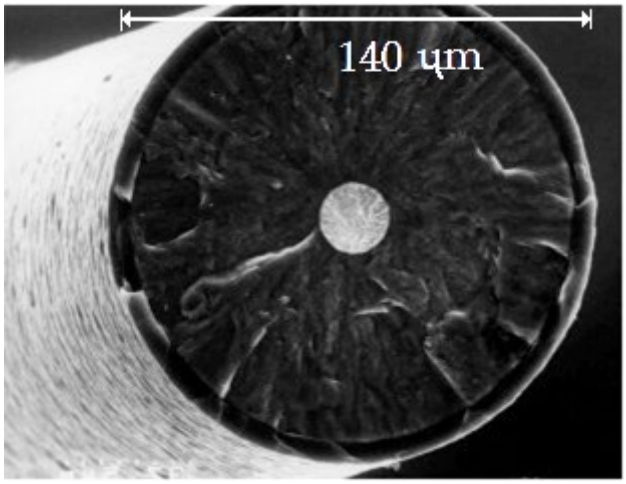

Figure 3
Taken directly from TISICS Ltd website[22], this figure depicts is an SEM image of cross-section of Sigma fibre produced by TISICS Ltd.

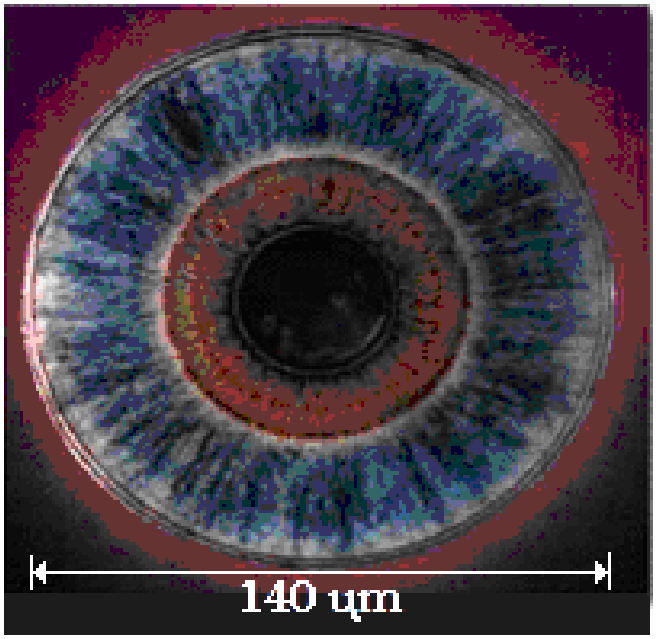

Figure 4
Taken directly from the website of Speciality Materials Inc., [23], the figure depicts the cross-section of SCS-6 fibre which was one of the materials investigated in this study.

The disadvantages of this type of SiC fibre tend to be reduced performance at very high temperatures and resistance to ionising radiation (i.e. Scholz, who observed changes in creep behaviour in SCS-6 below even 0.07 dpa [36]). Sigma brand fibre also begins to exhibit decoupling between the internal tungsten core and the surrounding β-SiC sheath at temperatures above ~1000°C [22]. Another disadvantage of growth from core filaments for composites is large diameter, which tends to be on the order of 100 µm. This is too thick for weaves on the scale of nuclear components. Nuclear grade fibres tend to be manufactured instead by pyrolysis of a polymer precursor, such as polydimethylsilane (as described extensively in Bunsell and Piant[18]), or polycarbosilane in this work (National University of Defence Technology, China) [61] which is first spun into a fibre of desired dimensions. The market for these is dominated by the Hi-Nicalon and Tyranno families of fibres produced by Nippon Carbon and Ube Heavy Industries, respectively, on which the majority of research on radiation effects into SiC has been performed over recent years

(e.g. [24-35]). Generally this type of fibre is far more difficult to produce than those grown around a fine metallic core as is demonstrated by figure 5, which is a TEM image showing the micro-structure of a Hi-Nicalon fibre [18]. There, β-SiC grains are surrounded by regions of disordered Si-C atoms that had not fully crystallised, as well as islands of free carbon. The small amount of excess Oxygen in Hi-Nicalon is thought to reside in the β-SiC grain boundaries also visible in figure 5. These factors are thought to account for the properties of Hi-Nicalon SiC fibre being significantly different from what is expected of pure stoichiometric β-SiC fibre (discussed extensively by Bunsell and Piant)(2006) [18].

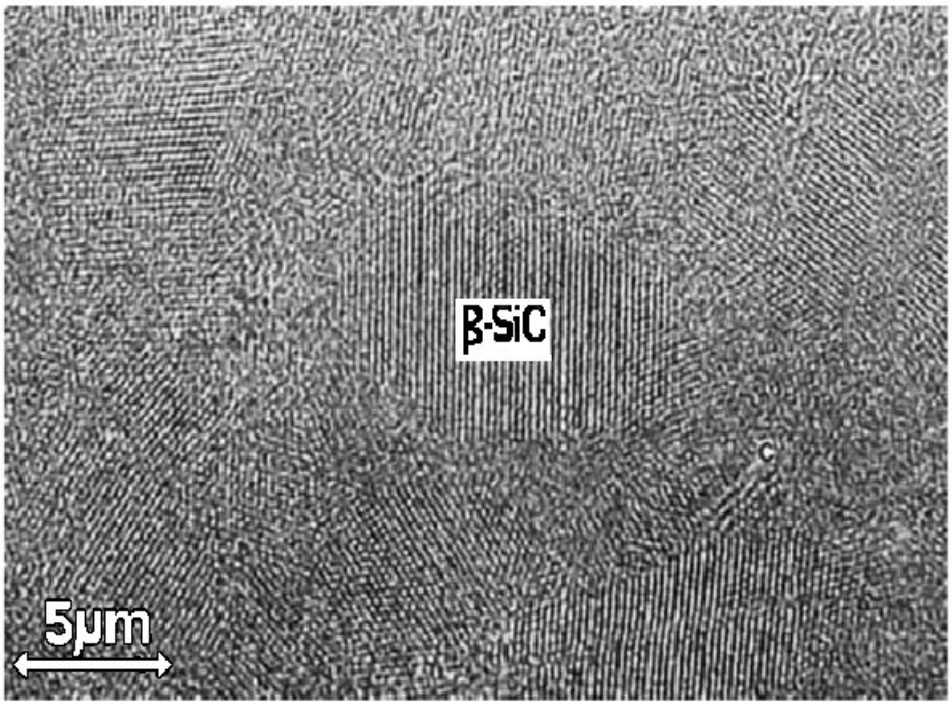

Figure 5
Taken directly fromBunsell and Piant [18], a high resolution TEM image of the structure of the Hi-Nicalon thin fibre. The β-SiC regions are about 10 nm across, surrounded by poorly ordered Si-C phases and turbostratic carbon.

In the modern versions of these brands, refinements to production techniques offer truly sintered, near-stoichiometric SiC (a feat achieved only relatively recently [18]). In the case of Ube Industries, Pyrolysis is carried out in a 2-step process to produce the Tyranno SA1 and SA3 brands. Firstly, by heating to ~1200°C to permit the decomposition of oxide phases and out-gassing, particularly of CO. In the second step, the fibre is sintered at ~1600°C using a thin aluminium coating over the precursor as a sintering aid. Nippon Carbon's Hi-Nicalon Type-S is produced instead via an intermediary process of electron irradiation during heating to induce the scission of Si-H and C-H bonds in the precursor and permit Si-C bonds to form in their stead, resulting in a near stoichiometric fibre without sintering aids. Further heating at 1500°C in a hydrogen rich atmosphere removes excess carbon from the structure. The properties of these fibres are summarised in tables 4 and 5, together with those of Sylramic fibre produced by COI Ceramics that has similar applications.

Table 4
Taken directly from Bunsell and Piant [18] summarising the different brands of SiC fibre suitable for reactor applications, showing the slight variations in stoichiometry and its corresponding effect on density due to differing manufacturing processes involved with each as discussed above.

	Manufacturer	**Elemental Composition (wt%)**	**Density (gm/cc)**	**Average Diameter (μm)**
Tyranno SA 1	Ube Ind.	68Si +32C + 0.6Al	3.02	11
Tyranno SA 3	Ube Ind.	68Si +32C + 0.6Al	3.1	7.5
Sylramic	COI Ceramics	67Si + 29C +0.8O + 2.3B + 0.4N + 2.1Ti		10
Hi-Nicalon Type-S	Nippon Carbon	69Si + 31C +0.2O		12

Table 5
Taken directly from Simon and Bunsell(1986)[33] summarising the different room temperature material properties of each fibre type.

	Room temperature Axial Thermal Conductivity W/m.K	**Room Temperature Strength (GPa)**	**Room Temperature Young's Modulus (GPa)**
Tyranno SA 1	65	2.8	375
Sylramic	46	3.2	400
Hi-Nicalon Type-S	18	2.5	400

2.2. Radiation Damage in SiC

2.2.1 Irradiation and High Temperature Creep Experiments

Over recent years, there has been extensive research into ceramic materials for nuclear applications, using several different irradiation and material property characterisation techniques. Direct neutron irradiation was carried out on Tyranno SA and Hi Nicalon Type-S fibres at 7.7 dpa and 800 ^{o}C by Hinoki et al (2002) [19]. Material testing in that study involved 4-point flexural tests, with SEM performed on the fracture surfaces created. Testing there was performed on bare fibres, Chemical Vapour Infiltrated (CVI) composites and Chemical Vapour Deposited (CVD) bulk SiC. Here it is stated that the primary difficulties surrounding the use of SiC fibre composites in high radiation applications concern the interface between matrix and fibre (but see also [41-44]). This is attributed to be due to volumetric changes which tend to occur in SiC as a result of radiation effects at different rates depending on the impurities in the SiC material. In this way, a fibre that expands differently to its surrounding matrix was found, by Snead et al [42] to exhibit poor inter-facial properties. Some of this was attributed to volumetric change in SiC fibre (shrinkage due to irradiation-induced grain growth) and matrix (expansion due to point defects) but contributions due to irradiation induced oxidation and swelling of the graphite interface then used between fibres and matrix were thought to dominate (see also e.g. Snead) [32, 42]. Nuclear applications tend to require SiC matrix composites with high purity fibre (as discussedin section 2.2.1.) and matrix, together with a high degree of homogeneity in material composition between the two for this reason. Trends in research (circa 2002 e.g. [5-7]) in SiC/SiC manufacture are directed towards near stoichiometric SiC, particularly with lower oxygen content and SiC based interfaces

between fibre and matrix instead of graphite based. Matrix composites were made on site via use of forced-flow thermal gradient CVI (FCVI) (i.e. Snead et al)(1998)[24] at Oak Ridge National Laboratory, though a pyrolitic carbon interface was applied to the fibres by CVI prior to forming the composite. The nominal thickness of this inter-facial layer is quoted as between 150 and 500 nm. Irradiation of samples was performed using the HFIR 14J capsule at Oak Ridge National Lab with a fluence of $7.7*10^{25}$ neutrons/m^2 (for incident neutron energy > 0.1 MeV). The composites tested were 2.2 millimetres thick such that properties gathered from them were likely to accurately model those of a full scale ceramic composite component used in an application under the radiation and temperature conditions described. Composites were cut into 30x6x2.2 mm^3 strips in order that four point flexural tests could be performed, from which the majority of quantitative evidence was obtained. The composites were found to be mostly unaffected by neutron irradiation at this dose and temperature. The inherent problem with using a neutron source for irradiation testing is that the intensity of neutrons required to cause large doses (representative of operation over the lifetime of a Fusion/Gen IV reactor as in table 2) is prohibitively large due to the low ionisation rate of neutron radiation in matter (primary knock-on events from fast neutron interactions in a material are sparse, most of the neutron's energy is carried off with it when it leaves the sample, as discussed below)(see e.g. Nelson et al) (1970) [46]. Hence only a dpa of 7.7 was achieved in these tests in total after the full period of exposure, perhaps an order of magnitude less than that expected to be encountered over the lifetime of a Gen IV nuclear reactor [11].

In a separate study, Katoh et al [25] performed a similar experiment with the same fibres and comparable neutron irradiation conditions (4.5-7.7*10^{25} neutrons/m^2) with the addition of charged particle irradiation at up to ~200 dpa. This was done using Si^{2+} ions at 5.1 MeV, which provides potentially very realistic modelling (see section 2.3.2) of neutron effects in a SiC composite. This is because almost all the ionisation caused by fast neutrons is from primary knock-on ions produced from the material atoms (e.g. Was) [51]. Hence for fast neutron radiation in a nuclear reactor, in effect, the majority of ionisation is done by energetic Si and C nuclei produced randomly in the sample. Unfortunately, the penetrability of Si ions at 5.1 MeV is very small, so that by 2500 nm (2.5 um) the Si ions are stopped entirely. Compared to experiments involving neutron irradiation alone, the effects of greater radiation intensity could be studied by this method [45-47]. The findings of Katoh et al in this study [25] are summarised in table 6. The formation of dislocation loops was observed from condensations of defect clusters at temperatures about ~600^{o}C. At very high radiation depositions (30-100 dpa) and temperatures (1400^{o}C) Frank Faulted loops of mean diameter 13-36 nm were observed. Frank faulted loops are formed by collapse of a cluster of vacancies into a toroidal shape (see e.g. Hull [73]). Typically a group of vacancies merge (due to surface tension on the boundary of the cluster, a single large void is energetically favoured over a series of small point dislocations)[73] and then the stress across the boundary of the vacancy cluster tends to collapse it into a loop.

A separate type of dislocation was observed but not conclusively characterised – some clusters of defects were detected that may have been dislocations but could not be clarified because of the small defect sizes involved with previous studies [45]. Due to an

absence of a detectable streak in the electron diffraction patterns taken in this study, it was surmised that Frank faulted loops were not the dominant type of dislocation in the samples tested. The conclusion there was that at least two distinct types of dislocation structure condense in SiC in these regimes of temperature and relative radiation damage. Figure 6 shows the relative temperature and dose regimes for black spots, loops and voids. The data from Katoh et al in table 6 supports the following qualitative trends for defect behaviours in SiC under irradiation:

- Defect density increases weakly with increasing dose but decreases strongly with increasing temperature during irradiation (temperature can anneal radiation damage in SiC).
- Cavity density increases strongly with temperature and weakly with dose and cavity radius increases weakly with dose and possibly with temperature.

Care must be taken when looking for quantitative trends in such data due to the limitations associated with sample sizes – for example, the 6 dpa, 300 ^{o}C sample took $1.2x10^{7}$ seconds (around 5 months) to irradiate. Variation in defect size and population between randomly sampling areas on a specimen may also be present.

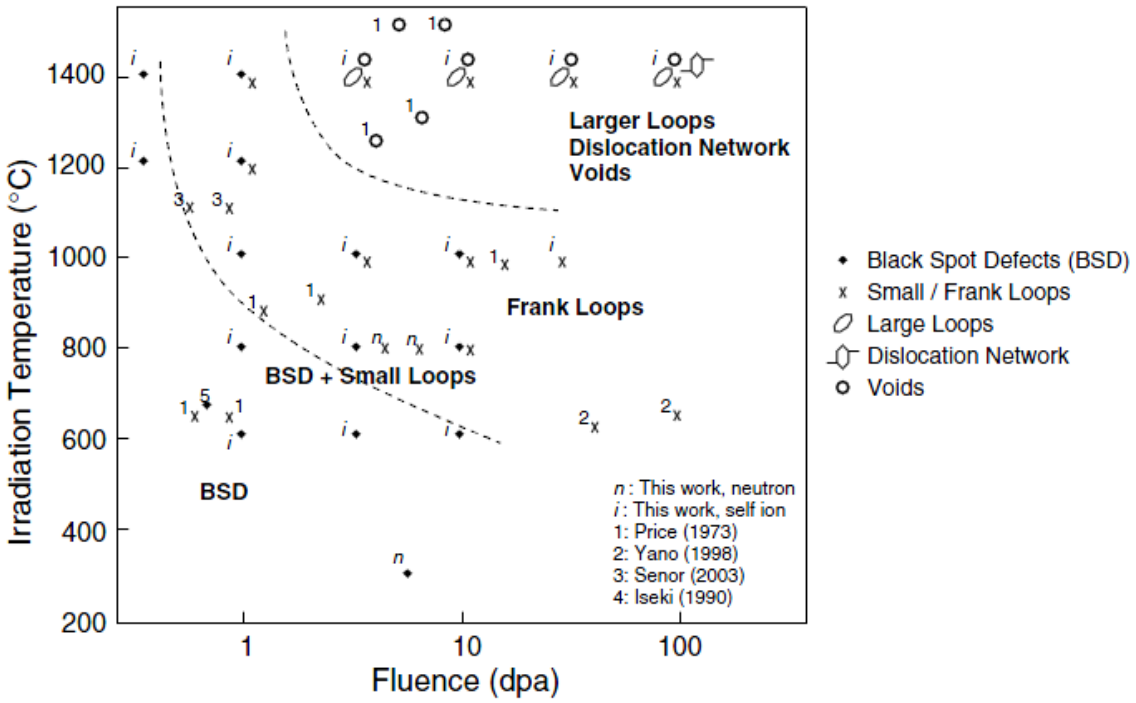

Figure 6

Taken directly from Katoh et al [25], this figure shows how the differing regimes of temperature and radiation damage measured by Katoh and compiled from similar studies are correlated with the prevalence of differing species of defect.

Table 6
Table from Katoh et al [25] showing the relative temperature and radiation domains of different defect populations as in figure 6.

		Black Spot/Loops			Cavities	
Irradiation Temp (°C)	Dose (dpa)	Type	Density (m^{-3})	Radius (nm)	Density (m^{-3})	Radius (nm)
Neutron ($0.5x10^{-6}$ dpa/s, HFIR, ORNL)						
300	6	Black spots	$2.2x10^{24}$	<0.5 a	Not detected	N/A
800	4.5	Mix	$2.6x10^{23}$	1.3	Not detected	N/A
800	7.7	Mix	$3.3x10^{23}$	1.5	Not detected	N/A
Ion (~$1x10^{-3}$ dpa/s, 5.1 MeV Si2+, DuET, Kyoto University)						
600	10	Black spots	not measured	not measured	Not detected	N/A
800	10	Mix	not measured	22	Not detected	N/A
1000	10	Loops	$2.6x10^{21}$	~2	$<1x10^{20}$	1.6
1400	10	Loops	$2.3x10^{21}$	~5	$2.0x10^{22}$ (b)	~2
1400	30	Loops	$2.3x10^{21}$	12	$1.3x10^{24}$ (b)	~3
1400	100	Loops	$5.2x10^{21}$	18.1	$1.8x10^{24}$ (b)	~4

One of the principle utilities of a fibre reinforced SiC/SiC composite is "fibre pull-out" during fracture, which acts to retard the propagation of a crack so as to combat a catastrophic brittle failure [48]. Hinoki et al [19] observed the fibre pull-out visible along a SiC/SiC composite fracture surface electron microscope for Hi-Nicalon and Tyranno SA composites in non-irradiated samples and irradiated samples at 7.7 dpa and 800°C, finding no appreciable change in extent of the pull-out in either case. Katoh et al [34]

report a slight increase in average pull-out length (from 5-10 um to 5-20 um) after irradiation at ~570°C / 2.2 dpa & ~1000°C / 5.3 dpa. In that study, samples of irradiated bare SiC fibre also underwent tensile testing to provide characteristic strengths for each temperature and irradiation considered. The characteristic strength of neutron irradiated SiC/SiC increased for sample conditions below 770°C / 3.3 dpa (from 2.03 GPa to 2.20 GPa for Tyranno SA3), after which (the next tested conditions were 910°C / 5.3 dpa) this property suffered a marked decrease (to 1.74 GPa for SA3). This behaviour was found to be significant even for comparatively low dose – for 280°C / 0.6 dpa the SA3 composite had a characteristic strength of 2.5 GPa. Despite the significant changes observed for SiC fibres, the SiC/SiC composite samples exhibited no such behaviour, with essentially no change (within the error quoted, though typical sample sizes were around 4 for each temperature and dose tested) in tensile properties under cyclic loading up to ~3.5 dpa & 780°C for the Tyranno SA3 composite. A significant drop in ultimate tensile stress for Hi-Nicalon Composite was recorded for up to 610°C/2.8 dpa, but these were done with relatively small sample sizes. By comparison, the behaviour was measured at 1000°C/5.3 dpa using a much larger sample size (20 compared to ~4) to give a result not appreciably different from a non-irradiated sample.

2.2.2. Computational Methods for Ion Irradiation Modelling

Computational methods are often used in conjunction with experiment in studies involving radiation damage of the types discussed here. For some applications it is indispensable, for instance the calculation of the equivalent displacements per atom (dpa) for a particular irradiation run. This notation allows for useful comparison of different regimes of radiation dose on materials for different types of radiation. In order to find the average number of times a lattice atom is displaced (which is precisely the dpa), computational methods are the only option. One particular code called SRIM/TRIM (Stopping/Transport of Radiation In Matter) [57] is used often in academic research (e.g. Katoh et al) [34] or [45, 47].

With the potential understanding of ion behaviour in materials that programs such as SRIM can provide, an experiment using charged particles may be made to well imitate the damage caused by high energy neutrons. As discussed extensively by Nelson et al [46], the major difference between neutron and charged particle radiation is in the primary recoil spectra (illustrated in figure 7). Neutrons interact far more rarely with a material and (in effect) exclusively with nuclei, but usually an interaction results in a lattice atom being scattered from its site at high energy. The radiation damaged caused by such 'primary knock-on' entities is in effect identical to that of an ion of the same element as the scattered lattice atom being produced in that location. For high energy charged particles incident on a material, the majority of interactions with the lattice also result in scatterings of lattice atoms, except that these tend to produce primary knock-on ions at much lower energy.

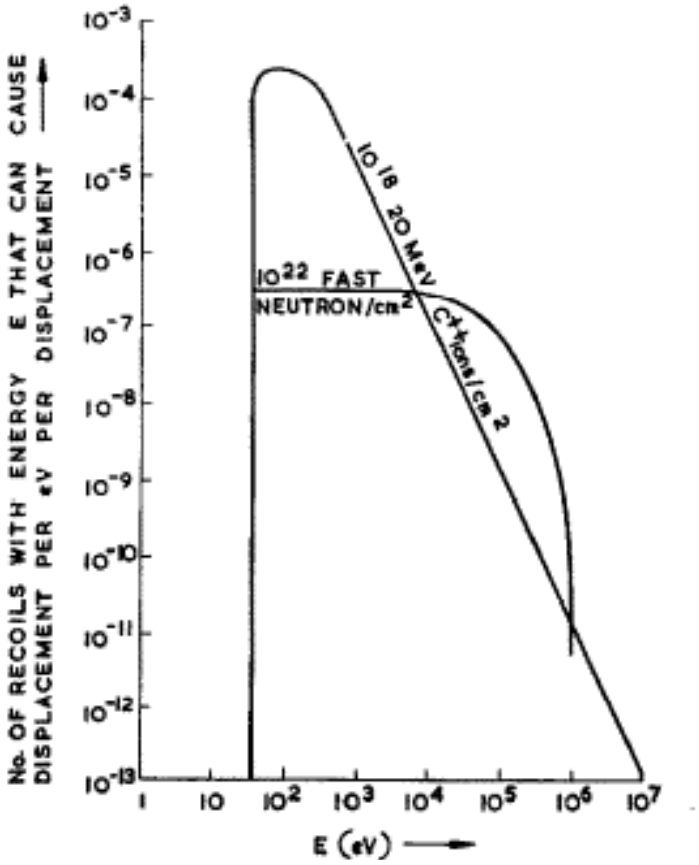

Figure 7
Taken directly from Nelson et al [46], this illustrates the difference in primary recoil spectra between fast neutrons and charged particle radiation, with many more low energy primary knock-on atoms for charged particles, as described above.

This can be accounted for provided an adequate knowledge of the energy loss of charged particles through a medium is known. Energy loss per unit distance tends to increase as the kinetic energy of an ion decreases. The rate of ion energy loss through a material is well approximated by the following Bethe formula (see e.g. Was)[51]. For particle speeds much less than the speed of light, as is well approximated in this case, as per equation 1.

$$-\frac{dE}{dx} = \frac{4\pi n z^2}{m_e v^2} \cdot \left(\frac{e^2}{4\pi\epsilon_0}\right)^2 \cdot \left[\log\left(\frac{2m_e v^2}{I}\right)\right]$$

Equation 1
Bethe formula for rate of energy loss of an ion moving through a material [51],
where z = charge of ion (Coulombs) , e = electron charge (Coulombs), m_e = electron mass, v = particle velocity, ε_0 = the vacuum permittivity, n = electron density in target material and I = the mean excitation potential of the material through which the ion travels.

Using the Bethe formula above, at lower energies (~10 MeV for protons) the energy loss of a beam ion is proportional to 1/(velocity)^2[51] so that at around the stopping distance the radiation displacement damage is much higher than in the material previously passed as in figure 8. There, Nelson et al used C^{2+} ions which were calculated to give an equivalent dose level of ~106 incident neutrons per ion at peak dose, which was over a distance of about a micrometre just before their stopping distance. After this, the C^{2+} ions thermalise and become incorporated into the material. Similar behaviour is displayed by lighter nuclei such as hydrogen, except with lower peak damage and higher penetration. In this way locally strong ionisation similar to that caused by primary knock-on ions from neutrons may be mimicked by an ion beam, with the depth of the material most affected by the ion beam changing depending on the incident energy. This can in principle be altered during operation, for instance via a degrader block placed along the beam path to decrease the energy of the beam ions as they pass through it. It may therefore be possible to scan through the depth of a material and deposit beam ions evenly whilst still strongly irradiating the sample.

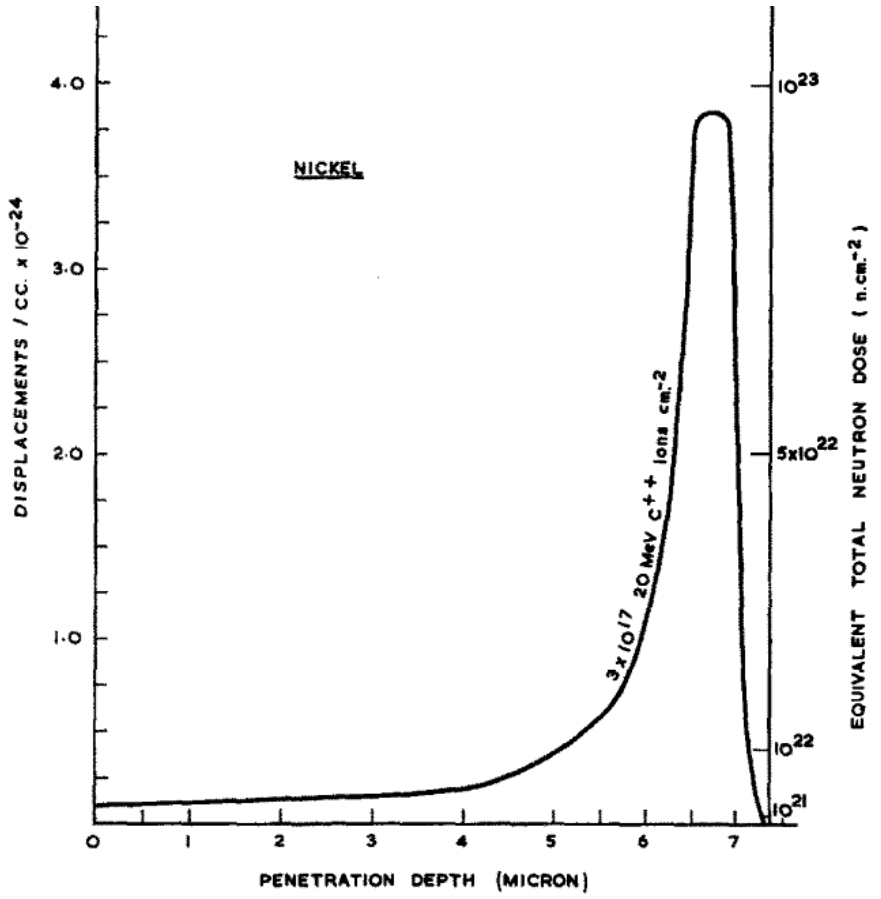

Figure 8
Here Nelson et al [46] describe the large increase in displacements per unit depth at low energies for incident ions near the total stopping distance.

The second advantage to ion beams for irradiation research is that when the ions in the beam stop they will be trapped in the material. If the incident ions are helium or hydrogen, the production of these by transmutation in a neutron irradiated source can also be mimicked within the material. For these considerations to be adequately addressed, the microscopic behaviour of charged particles within the tested material must be well modelled analytically or numerically. The energy loss of light ions in materials is often well approximated as being continuous over the path of the ion [51]. However, only a discrete number of interactions actually occur for each ion, so that the passage of ions through a material can vary greatly from ion to ion (see TRIM simulations done in this

work in appendix A for examples in ion scattering through SiC). The effect of this on analytical calculations, for example using the Bethe formula, is to smear out predictions of stopping distance for incident ions. SRIM and TRIM use Monte-Carlo simulation by calculating the effects of individual ion paths through a material (the average damage being collected to form dpa vs depth plots as in appendix A or section 3.5.2.), hence these phenomena can be taken into account [57]. Figure 9 shows the damage profile of a Si ion stopping in SiC, where the deposition behaviour can be directly seen, with negligible loss to the material at shallow depths up to a broad damage peak at a depth of about 2 μm. Typically this is how ion irradiation has been used in the literature for SiC – minimal penetration but very high damage to surface layers [24, 34, 35]. However, for metals it is different e.g. Nagakawa et al [68] used 17 MeV protons. For targets made of heavier elements (like steels), the damage done per ion is higher and the penetration depth lower so that higher energy protons are more suitable for heavier target materials like steels. Table 7 (taken directly from Miro et al) [36] provides a summary of ion irradiation parameters in typical studies of ion radiation effects in SiC materials. Using the strategy outlined above (low energy ion beam and a very thin sample), the altered stoichiometry of the irradiated volume of a SiC sample can have as much as 2.37% He (Beaufort et al) [38].

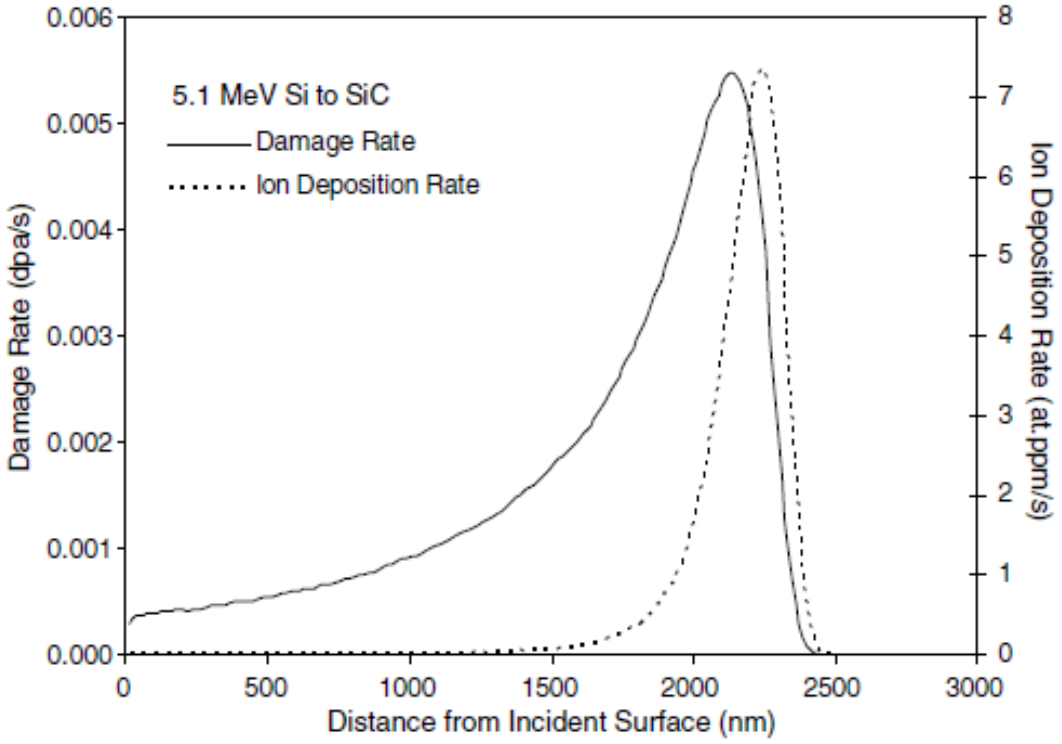

Figure 9
Taken directly from Katoh et al [36] modelled using the TRIM software with Si^{2+} ions bombarding SiC.

Table 7
Taken directly from Miro et al[36]. The table summarises data compiled for He implantation in SiC as of 2011 for low dpa exposures.

Authors	**Sauvage et al**	**Beaufort et al.**	**Zhang et al.**	**Smith et al.**	**Oliviero et al.**	**Miro et al**
Samples	6H-SiC	4H-SiC	4H-SiC	6H-SiC	6H-SiC and 4H-SiC	6H-SiC and 4H-SiC
Energy (KeV)	500	1600	40	40	3(Max)	3000
Fluence (1/cm^2)	5*10^15	5*10^16	5*10^15	1.17*10^16	1*10^15 (Max)	1*10^15
R (micrometers)	1.2	3.65	0.2	0.199	0.024	8.59-8.52
Vacancies/ Ion-nm	0.31	0.3	0.355	0.355	0.8	0.16
dpa	0.16	1.44	0.18	0.43	0.08	0.17
[He] (at.%)	0.35	2.37	0.55	1.28	0.46	0.33
[He]/dpa	2.19	1.65	3.06	3	5.75	1.94
TEM observations	No bubbles at 1573 K	Bubbles at 1773 K	Bubbles at 1173 K	-	-	-
NRA results	No He left at 1573 K	-	-	Migration at 1273 K	-	-

2.3. Previous Mechanical Testing of Nuclear Composites

2.3.1. Creep Testing

The primary conditions under which the structures being researched will operate as components in a nuclear reactor are comprised of a continuous stress applied at very high temperatures and under irradiation. The creep behaviour of materials for some nuclear applications (particularly those relevant for SiC) is thus important - a typical setup can be found in e.g. Peter et al [37], for high temperature testing in an inert atmosphere. There, the specimens are shaped in a dogbone configuration, to allow for easy clamping on the rig (as in figure 10). Resolution of creeping strain in the sample is realised through extensometers within the clamps. Proximity of the clamps to the specimen allows for thermal equilibrium to be reached between them and the sample and thermocouples within the clamp can measure temperature directly. For extension to irradiated creep tests, a gap must be left for exposure of the sample to the incident radiation. In this case, measurement of temperature must be done by indirect means such as IR sensor (since it is higher in the isolated central region of a test sample) and maintenance of the temperature during the creep must be performed using e.g. helium gas or variable temperature radiator, as in Nagakawa et al [68].

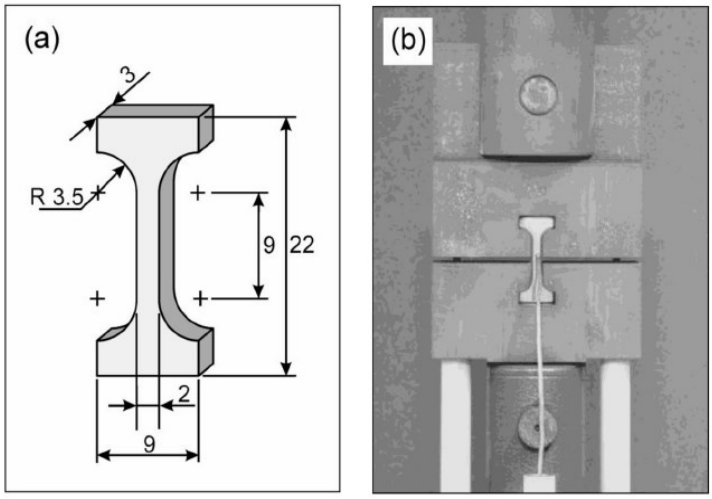

Figure 10
Diagram for setup used by Peter et al [37] taken directly from that source. The dogbone configuration is often used for SiC specimens for testing in tension. The geometry of the clamps would have to be altered for an in situ irradiation-creep design so as to permit the incidence of ions upon the sample but otherwise may look very similar to this.

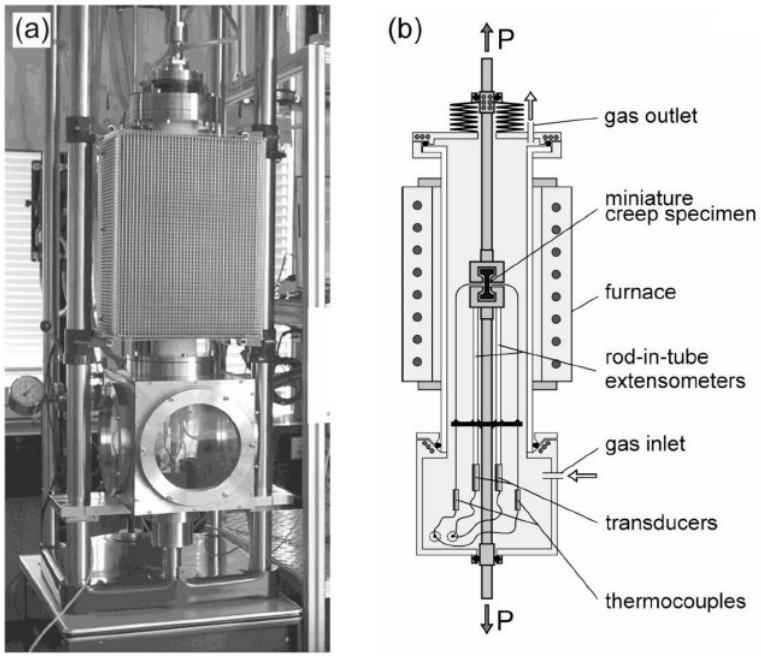

Figure 11
The full apparatus used by Peter et al [37] – the size, on the order of a metre, makes inclusion in a cyclotron setup potentially difficult.

2.3.2. Torsion Testing

Torsion setups tend to be far simpler to produce and more compact than creep rigs, size usually being an issue for vacuum environments, requiring large and costly pressure vessels and associated pumps. Whilst it may be preferable for applications to test ceramic fibres at high temperature and controlled exposure to oxygen (see e.g. Hasegawa et al [4] for importance of degradation mechanisms for fibre coatings as a mechanism that changes the mechanical properties of composites under irradiation in oxidising atmospheres), in practice maintaining the temperature of the specimen is done using a radiator for which an inert atmosphere is essential (else a helium jet is used, which also requires isolation from atmosphere). Use of a very thin/evacuated atmosphere also permits the use of delicate instruments in order to obtain high accuracy. As an example of this, Nagakawa et al [68] crept F82H steel in torsion at 300^{o}C using a highly sensitive setup; an angular resolution of about 0.001 degrees was obtained, corresponding to resolution in sample shear strain of $7*10^{-8}$. As shown in figure 12, this was achieved using a laser reflected off a thin mirror that turned with the sample, small angular displacements altering the destination of the beam corresponded to measurable decreases in detected intensity.

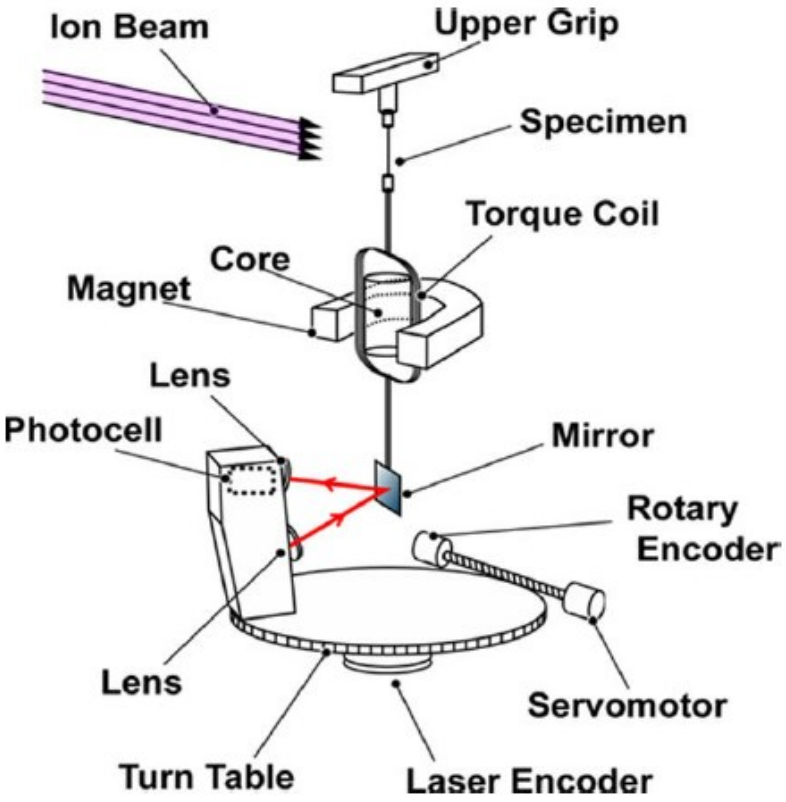

Figure 12
Torsion rig as used by Nagakawa et al [68]. Rotation of the turntable permits correction to changes in received laser flux so that the detection apparatus can move with the shearing sample. The main advantage of this set-up is relative compactness and ease of construction compared to a creep rig.

3. MATERIALS INVESTIGATED AND EXPERIMENTAL SETUP

3.1 Experimental Work and Irradiations Performed

3.1.1. Experimental Work Performed

Table 8 summarises the experimental work done in the project from which data was collected.

Table 8
Work matrix of all mechanical testing and x-ray tomography performed.

Material	Tension	4-Point Flexure	Vickers Indents	Nanohardness Indents	X-Ray Tomography
SCS-6 fibre	X				
Nicalon	X				
KD-1	X				
Hot pressed			X		
Sintered		X	X		
PCS KD-1 Fibre Composite		X		X	X
LPVCS KD-1 Fibre Composite		X		X	X

3.1.2. Irradiations Performed

Table 9 summarises the irradiations performed on materials investigated.

Table 9

Doses for all irradiation runs used in mechanical testing.

Material	Irradiation Condition 1	Irradiation Condition 2	Irradiation Condition 3
SCS-6 fibre	0.0007 dpa (5 hours (1 uA/cm^2)) 400 °C air		
Pressureless sintered α-SiC	0.0007 dpa (5 hours (1 uA/cm^2)) 400 °C air		
Hot pressed α-SiC	0.0007 dpa (5 hours (1 uA/cm^2)) 400 °C air	[2]	
Nicalon		0.0007 dpa (5 hours (1 uA/cm^2)) 400°C air	0.0014 dpa (10 hours (1uA/cm^2)) 400°C air
KD-1	0.00021 dpa (3600 uC (0.3 uA 4 hours)) vacuum 80°C[1]	0.0007 dpa (5 hours (1 uA/cm^2)) 400°C air	0.0014 dpa (10 hours (1uA/cm^2)) 400°C air
PCS KD-1 Fibre Composite	0.00021 dpa (3600 uC (0.3 uA 4 hours)) vacuum 80°C[1]		
LPVCS KD-1 Fibre Composite	0.00021 dpa (3600 uC (0.3 uA 4 hours)) vacuum 80°C[1]		

[1]In practice, the temperature during vacuum irradiation was measured to reach 80°C adjacent to the target. This may be due to an inadequate representation of the thermal conductivity through the heating element connecting the target to the chamber wall.

[2]Hot pressed α-SiC was irradiated with α-particles at 12 MeVs, 1 μA per cm^2 for 1 hour and was found to have crumbled into smaller pieces, so that no mechanical testing was done on this sample.

3.2. Justification for Tests Chosen

Several SiC-based ceramic materials were each mechanically tested in the as-recieved forms and after irradiation. The irradiated samples were exposed to a beam of ions from an MC40 cyclotron at elevated temperature and then mechanically tested under the same conditions as the non-irradiated specimens so that a comparison could be made. The materials chosen were intended to represent the components of SiC/SiC fibre composites proposed for use in nuclear reactors. Thus, bulk sintered SiC and hot pressed α-SiC were used in this work for their similarity to a typical SiC-SiC composite matrix, while SCS-6 and Nicalon SiC fibres were chosen to provide information about the SiC fibres used in these composites. As has been done in the literature [24,30,32] mechanical tests focused on spotting degradation of the material itself under irradiation (through bend tests, indentation tests and tensile tests). The results of this testing could then be compared to those in the literature for reactor grade materials and potential changes in creep behaviour inferred.

3.3. Materials Investigated

3.3.1. Sintered α-SiC

Bulk sintered α-SiC, manufactured by Carborundrum Co. [71] was mechanically tested in this project. Table 10 summarises the properties of this type of α-SiC material. Formed at temperatures around 2000 ^{o}C, the sintering temperature is well above the limit beyond which the cubic lattice structure (β-SiC) stops being favoured thermodynamically over the other polytypes (which is around 1700 ^{o}C [49]). This material is very hard and has high elastic moduli (Young's Modulus around 400 GPa) and a porosity at around 2%, with typical pore sizes observed (see figure 13) to be from submicron sizes to around 10 ***μm*** in diameter. Comparing typical surface samples after polishing to 3μ diamond in figures 13 and 14, the microstructure of the hot pressed SiC used in this study was found to have less porosity and finer pores.

Table 10
Taken directly from Pierson [49], table showing typical material properties for α-SiC prepared through sintering or hot pressing.

	Sic content (% by weight)	Density (grams/cc)	Porosity	Young's Modulus (Gpa)
Sintered and Hot Pressed SiC	>98%	3.15-3.21	<1%	420-460

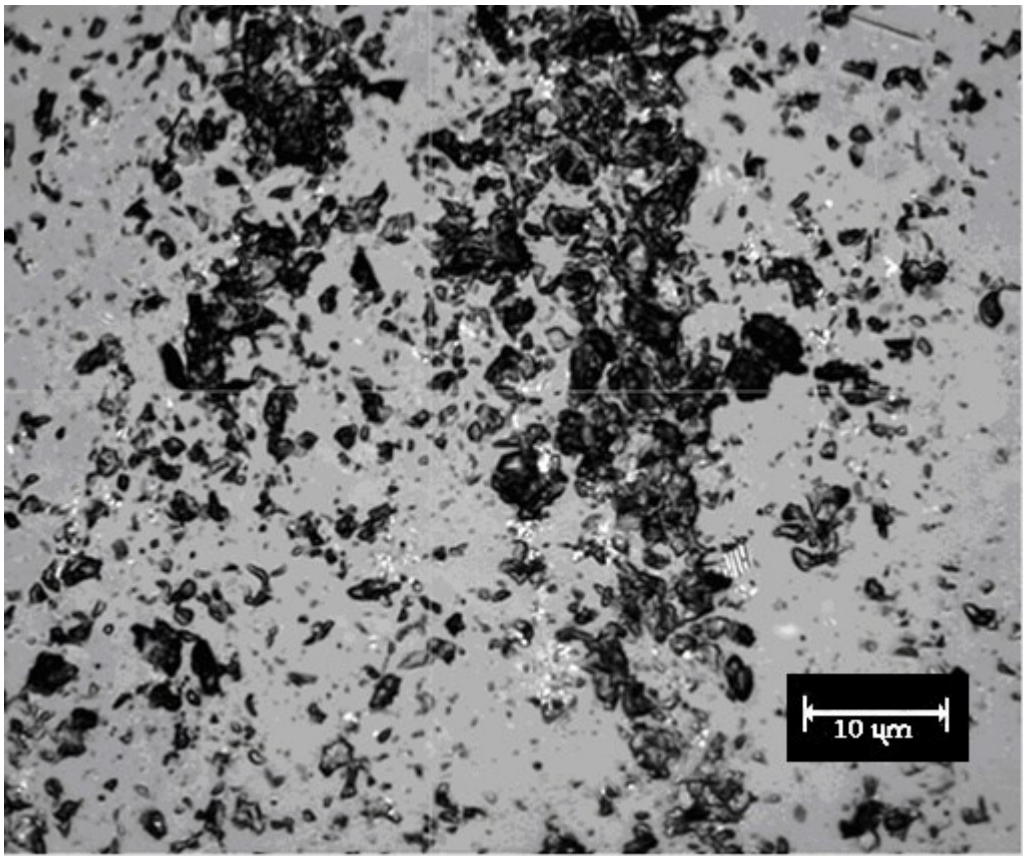

Figure 13
Surface structure of sintered α-SiC as polished up to a 3-µm finish using a diamond suspension. Image taken using an optical microscope.

3.3.2 Hot Pressed α-SiC

A higher purity SiC with lower porosity and smaller pore size can be produced by hot pressing. Unfortunately, densification by hot pressing up to the full theoretical density requires temperatures and pressures similar to those needed for diamond synthesis (~3.5 GPa, 2300 ^{o}C, Riedel and Cheng (2010) [50]). In practice, the graphite tools used for this can deliver pressures up to around 35 MPa but require sintering aids to operate, so that any hot pressed α-SiC material will contain some mix of around 0.5-3% Boron, Alumina, Beryllium Oxide and several other sintering agents [48-50]. Leftover sintering aids in sintered and hot pressed α-SiC can potentially present radioisotope activation problems and may contribute to a different behaviour under irradiation to pure α-SiC. The tradeoff is between the superior mechanical properties of hot pressed α-SiC and its greater expense compared to pressureless sintered α-SiC.

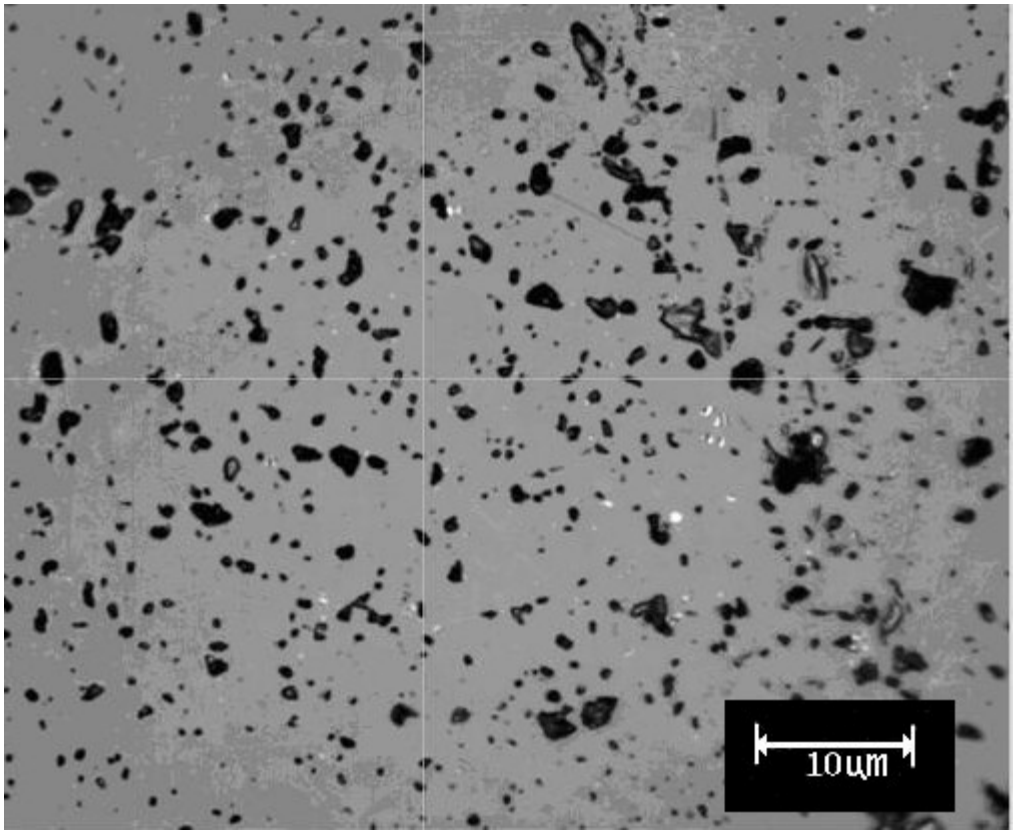

Figure 14
Observed microstructure of hot pressed α-SiC. Whilst similar in appearance to α-SiC, the pore size tends to be smaller and the surface easier to indent. Image taken using an optical microscope.

3.3.3. SCS-6 SiC Based Fibre

For aerospace applications, particularly titanium reinforcement, many companies provide SiC fibres with fine metallic cores around which SiC is grown by chemical vapour deposition. This method permits a high degree of control over the axial structure of the deposited material. One of the fibres investigated was of this type, produced by Speciality Materials Inc. It is intended for use primarily as reinforcement in the aerospace industry for turbine blades with titanium-based material as a matrix. For SCS-6, a carbon mono-filament is immersed in a gaseous Silicon Carbide environment within a furnace (information from Speciality Materials website) (2013) [22]. Its internal composition is controlled to deliver superior properties in this role (as in figure 15) – by slowly depositing layers of material, carbon content is varied with depth to give the optimal mechanical properties, summarised here in Table 11. This illustrates the versatility of such a manufacturing process, where the axial composition of a SiC fibre can be finely controlled.

Table 11
Material properties of SCS-6 SiC based fibre, taken from a technical presentation available on the Speciality Materials Incorporated Website (2013) [22].

Material Properties of SCS-6 SiC Based Fibre	
Diameter (μm)	140
Tensile Strength (MPa)	3450
Modulus (GPa)	400
Density (g/cm^{-3})	3.0

This material is well suited to the advantages of cyclotron radiation sources with the facilities provided due to its large diameter, ease of availability and non-uniform internal structure. With differing populations of Silicon and carbon in close proximity, it was thought that migration of carbon atoms could be observed (carbon being about twice as likely to be liberated from its lattice site as silicon under irradiation as discussed in section 2.2.2. on absorbed dose).

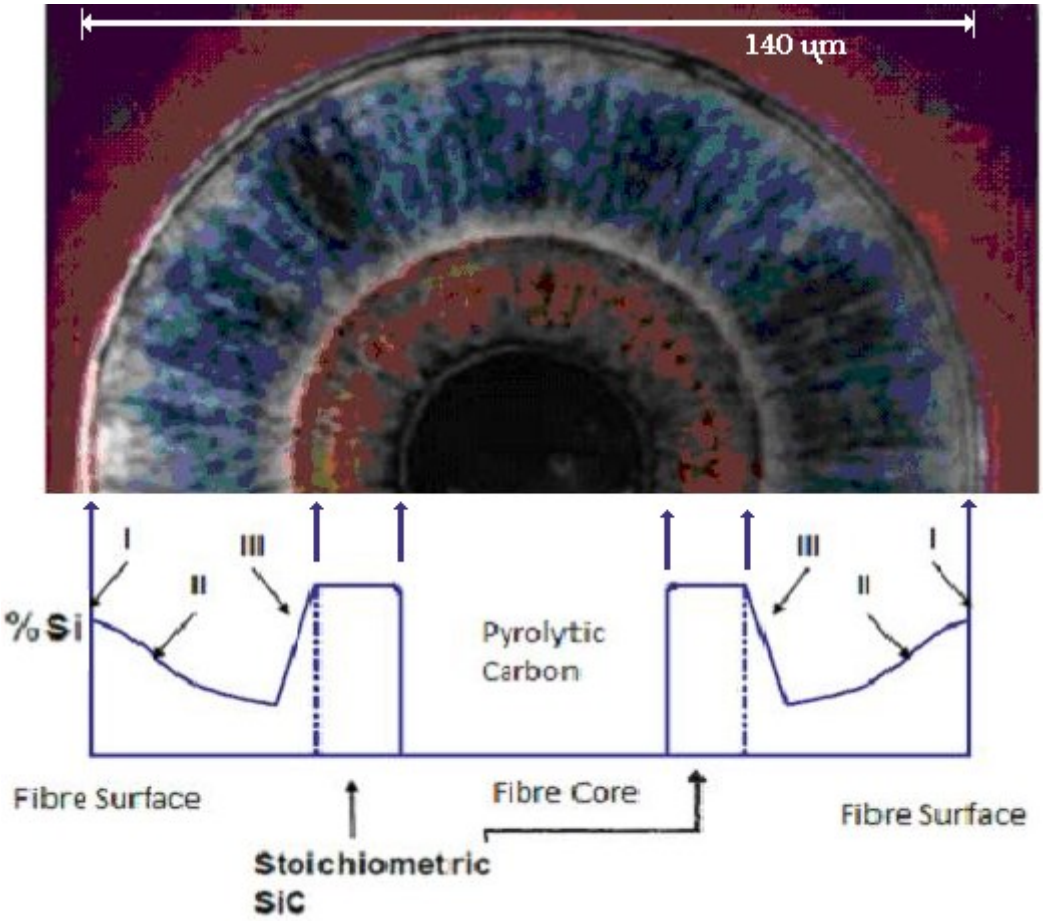

Figure 15
Internal characteristics of SCS-6 SiC fibre, the image is composed of content from a Speciality Materials Inc. presentation [22] on SCS-6 with an SEM cross-section of the fibre aligned with a plot of SiC composition with depth taken from the same source. Near stoichiometric β-SiC is grown directly onto the central carbon fibre core. This is surrounded by an inner gradient of reduced Si content to maintain filament strength (iii). From there towards the surface (ii and i), the silicon content is gradually increased.

3.3.4. KD-1 SiC Based Fibre

Produced by the National University of Defence Technology (NUDT) in China, KD-1 is the fibre reinforcement used in all composite materials tested in this project. It is made from the pyrolysis of a polycarbosylane precursor, a process which leaves a large proportion of oxygen in the fibre [61]. This may effect the potential usage of KD-1 based composites for high dose nuclear applications, since oxygen content has been correlated with the formation of glassy phases across interface boundaries between fibre and matrix in SiC/SiC composites under irradiation [41,42] as discussed in section 2.2.1. Table 12 outlines the properties of KD-1 fibres.

Table 12
Summary of mechanical properties of KD-1 fibres (Shuang et al, National University of Defence technology (NUDT), private communication, 2013)

Mechanical Properties of KD-1 SiC based Fibre	
Trademark	**KD-I**
Fibre diameter	13.3 μm
Density	2.45 gm/cc
Tensile Strength	1.8-2.2 GPa
Tensile Modulus	150-200 GPa

3.3.5. Nicalon SiC Based Fibre

Produced by Nippon Carbon Co., Nicalon fibre is composed of fine β-SiC crystals within a mixture of silicon, carbon and oxygen, as discussed in section 2.2.1. Table 13 summarises the typical attributes of this fibre.

Table 13
Taken from Bunsell and Piant [18], mechanical properties of Nicalon fibres.

Mechanical Properties of Nicalon	
Fibre diameter	14 μm
Density	2.55 gm/cc
Composition	57%Si : 32%C : 12%O
Tensile Strength	3.0 GPa
Tensile Modulus	210 GPa
Thermal Conductivity (300 K)	2.97 W/m.K
Thermal Conductivity (773 K)	2.20 W/m.K

3.3.6. KD-1 Fibre Composites

3.3.6.1 Production Process by Polymer-Infiltration-Pyrolysis

Composite materials were produced by weaving KD-1 SiC fibre into a 3D structure and then infiltrating a polymer precursor for SiC into the weave. The KD-1 fibres in this structure were first given a thin pyrocarbon layer by chemical vapour deposition to a thickness of 0.5 μm. Polycarbosylane solution was then vacuum impregnated into the fibre weave and left to dry. Consolidation of the composite was performed using a sealed chamber and a pressure of 9 MPa and temperature of 180 ^{o}C (the softening point of polycarbosilane) for 1 hour. Once infiltrated, the composite was pyrolysed at 1100 ^{o}C in an inert argon atmosphere to produce a SiC matrix that grows between the fibres. In practice, this process was repeated multiple times using the change in weight of the material to gauge how much extra SiC matrix has been added each time. The material was considered complete when the weight gained after pyrolysis was less than 1% (typically after 10 infiltration-pyrolysis cycles).

Two different materials were produced by this process. The PCS material is made using polycarbosilane, whereas the LVPCS material is made using a liquid polycarbosilane solution with active Si-H and $CHCH_2$ groups. The decreased viscosity in LPVCS resulted in better infiltration of the fibre perform and hence a higher density matrix was produced. (Shuang et al, private communication, 2013).

3.3.6.2 PCS Composite

PCS composites are formed [41] via a multiple step polymer infiltration and pyrolysis (PIP) process with consolidation, involving the pyrolysis of a SiC yielding polymer (polycarbosilane). KD-1 fibres were wound in a 3D structure (the weave was made in four directions in order to give close to isotropic mechanical properties). For the reasons described in 3.3.6.1., PCS has larger and more numerous voids when compared with LPVCS (Shuang et al, private communication, 2013, confirmed also in this work via x-ray tomography as in section 4.3.7.)

3.3.6.3 LPVCS Composite

As an alternative to polycarbosilane, liquid polycarbosilane with active Si-H and $CHCH_2$ groups was used as a polymer precursor in the LPVCS composites [41]. As compared to PCS composites, LPVCS composites have a much higher fibre density (since it penetrates fibre bundles more readily) and much lower porosity with smaller pore size, mostly concentrated around the fibre bundles themselves (Shuang et al, private communication, 2013, confirmed also by x-ray tomography in section 4.3.7. as above).

3.3.7. The Current State-of-the-Art Reactor Grade SiC Material

Composite materials considered for reactor use are manufactured by the nanopowder infiltration and transient eutectic (NITE) process, which delivers a low porosity, high density and mechanical properties. High Nicalon Type S and Tyranno SA are the current most advanced fibres, close to stoichiometrically SiC with very few impurities, especially oxygen [18, 64]. Ion irradiation is performed using multiple complimentary ion sources – helium and hydrogen implantation are achieved with those beams simultaneously with a separate beam for damage. Radiation damage is achieved using heavier ions; ideally, silicon or carbon can be used to avoid adding impurities that would otherwise not be added during neutron irradiation but the peak damage from much heavier ions like gold can be much greater. For all 3 types of beams the accelerating method tends to involve electrostatic acceleration, providing ion energies in the few MeV range and ion currents in the milliAmpere range[11, 45-47].

3.4. Experimental Methods

3.4.1. Mechanical Tests and Characterisation Methods Used

3.4.1.1. Fracture Toughness (by Vickers Indent)

Using crack lengths from indentations to measure fracture toughness is potentially far more convenient than using a standard destructive toughness test. It can be done quickly and simply without significantly damaging the specimen. In the case of the hot pressed α-SiC before and after irradiation, the very obvious change in the frequency and relative size of indentation induced cracking in the specimens makes this particularly relevant here. As discussed in Kruzic and Ritchie (2003)[54], the uncertainty inherent in this method only gives a value of fracture toughness to within an error of around 30%.

$$\boldsymbol{K = X\left(\frac{E}{H}\right)^{\frac{1}{2}}\frac{P}{a^{\frac{3}{2}}} = 0.016\left(\frac{400}{29}\right)^{\frac{1}{2}}\frac{1}{a^{\frac{3}{2}}} = \frac{0.06}{a^{\frac{3}{2}}}}$$

Equation 2
This expression[54] gives the indentation fracture toughness Kc in terms of Young's Modulus E, Vickers hardness H, applied force P, a normalising factor X (~0.016 +/-0.004) and crack length a.

For hot pressed α-SiC, the fracture toughness in equation 2 is given using E ~ 400 GPa, P = 1 N for all the hot pressed α-SiC tests. Testing in this work put the hardness at ~ 29 GPa. Substituting these values for E and P gives the expression on the far right hand side of equation 2.

3.4.1.2. Vickers Microhardness

Indents were performed using a Vickers Micro-hardness machine with 0.020 kgf and 0.1 kgf loads for sintered α-SiC and hot pressed α-SiC, respectively. The machine used was manufactured by Durascan. Low loads are necessary for the bulk materials studied because cracks tend to initiate from the edges at higher loads. Samples were polished, as for bend testing, to a 3 $\boldsymbol{\mu m}$ finish using a diamond suspension.

For α-SiC, the proximity of pores and the scale of induced cracking upon indentation was large enough that only very low loads could be used, which made measuring of the indents difficult on the machine available (so that only about 1 in 4 indents could be both found and measure properly). The hot pressed α-SiC fared better but at 0.1 kgf load often induced cracking and displayed significant variations in local porosity (examples of which can be seen in figure 16) contributing to the large standard deviation observed.

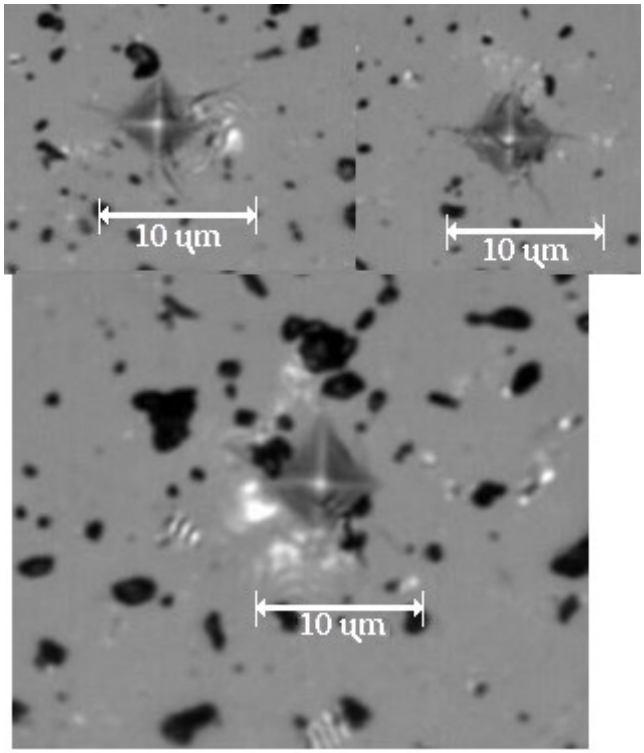

Figure 16
(a, b and c respectively, from top left going clockwise)
Typical Indents on the irradiated hot pressed α-SiC initiated cracks. In part (a) the cracks can clearly be seen deflecting around a sintering aid left in the structure from processing.

3.4.1.3. Nano-Indentation

Microhardness indentation is problematic for SiC because of the tendency observed for cracking to occur around most indents. The equations used to find the microhardness are invalid if cracking occurs at the borders of the indent (since the formation of cracks requires energy that would otherwise have contributed to indent depth, so that a cracked specimen is softer than the indent dimensions suggest). Nanoindentation can use much lower loads and hence escape these problems.

A Vantage system (product of the Micro Materials company)[74] was used to perform all nanoindents in this study. The general technique was originally proposed by Oliver and Pharr[55] as a means of testing brittle materials.

An automatic nanoindenter was used to record stress vs indentation depth profiles on exposed fibre and matrix surfaces on PCS and LPVCS materials, non-irradiated and irradiated. The load used was 500 mN with a cubic pyramid indenter geometry. Load vs displacement graphs were produced for random exposed and fibre faces for PCS and LPVCS samples. A number of factors other than inhomogeneity in the samples contributed to the standard deviation observed in the maximum indentation depth for each sample:

- Samples were polished to a 3 μm finish, which is close to the dimensions of the indenter.
- Fibres ran at around a 45^{o} angle into the material rather than being stacked vertically with respect to the indenter – the centre of each fibre was chosen as the target for indentation but the machine is rated for an error of around +/- 2 μm so it

is possible that some fibre indents had a different effective fibre depth directly below the indenter (as in figure 17).

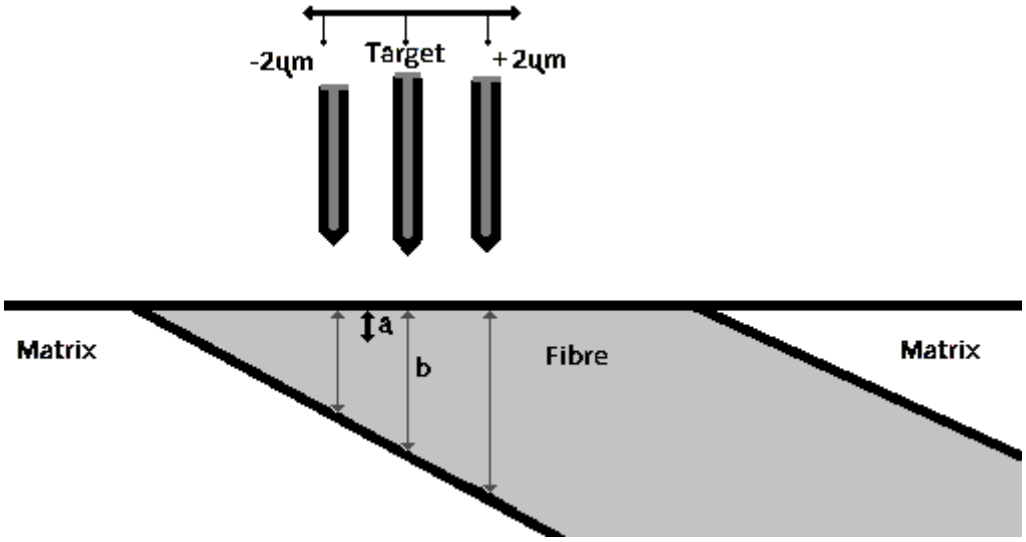

Figure 17
Diagram showing how uncertainty in indenter position can lead to different effective fibre depth – in most cases fibre depth should be several times larger than maximum indentation depth.

3.4.1.4. 4-Point Flexure

The bulk sintered-SiC samples were broken in flexure. Choice of 4-point over 3-point bending was determined by the larger total stressed area. 4-point bend tests offer the significant advantage (over 3-point bends) of a more uniform bending moment over the central region and provide distributed contact loads across the central two rollers[53]. This is important particularly for brittle samples such as those investigated here because it tends to counteract discrepancies between loading configurations between different test runs whereas (particularly for small samples) the shear component present in 3-point tests cannot easily be separated. The dimensions chosen are outlined in figure 18. Flexure was performed using an Instron 5566 with a 5 kN load cell. Polishing was achieved using a RotoPol-22 automatic polishing machine (from the Struers company). Bending was performed with a crosshead displacement of 0.05 mm/min. Samples were polished to a 3 **μm** finish using a diamond suspension and ground individually to their specified dimensions. Samples were of dimensions 4.8x18x0.9 mm in the format (width W)x(length L)x(depth d) with the greatest variation between specimens being in thickness, which varied by about +/- 5% and was accounted for in converting load to surface stress. A low thickness was necessary owing to the limited penetration power of protons in the experiment; 0.9 mm was chosen because a sample this thick because it was thought that this may be representative of larger composite structures (0.9 mm is about 64 fibre widths at 14 μm each) and was in practice just thick enough to be practical to prepare.

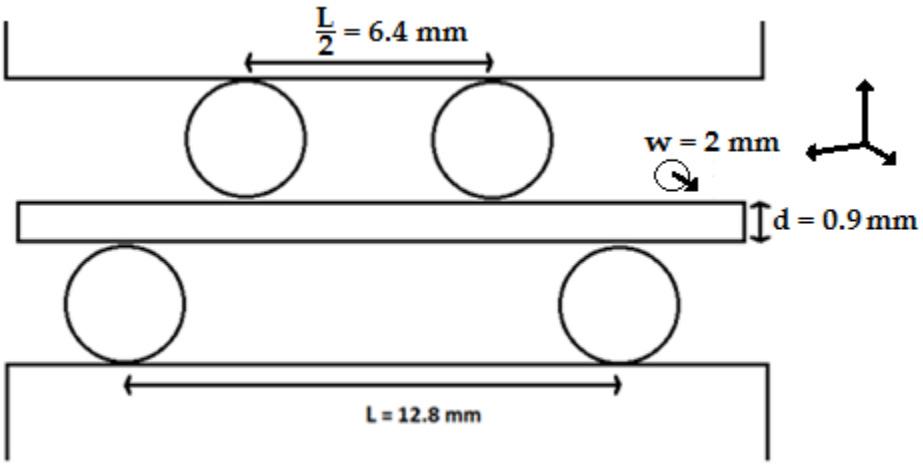

Figure 18
Dimensions of grips used for 4-point flexure.

Owing to the small size of the samples (necessary for the conditions of the test) achieving uniform dimensions was prohibitively difficult. Thus, a variation of less than around +/- 5% in the thickness was observed from specimen to specimen, together with a much smaller variation in thickness along the width of each specimen in the range of tens of microns (deemed insignificant). The variation in thickness was accounted for by normalising the load measured during the test as surface stress for each specimen with equation 2. Sintered α-SiC samples were irradiated with protons at 22 MeVs, 1.25 μA /cm^2 for 5 hours for an average dose on the polished (tensile) side of ~0.0065 dpa at ~700 K. Testing of irradiated samples was carried out within an isolated environment (clear plastic) as shown in figure 19.

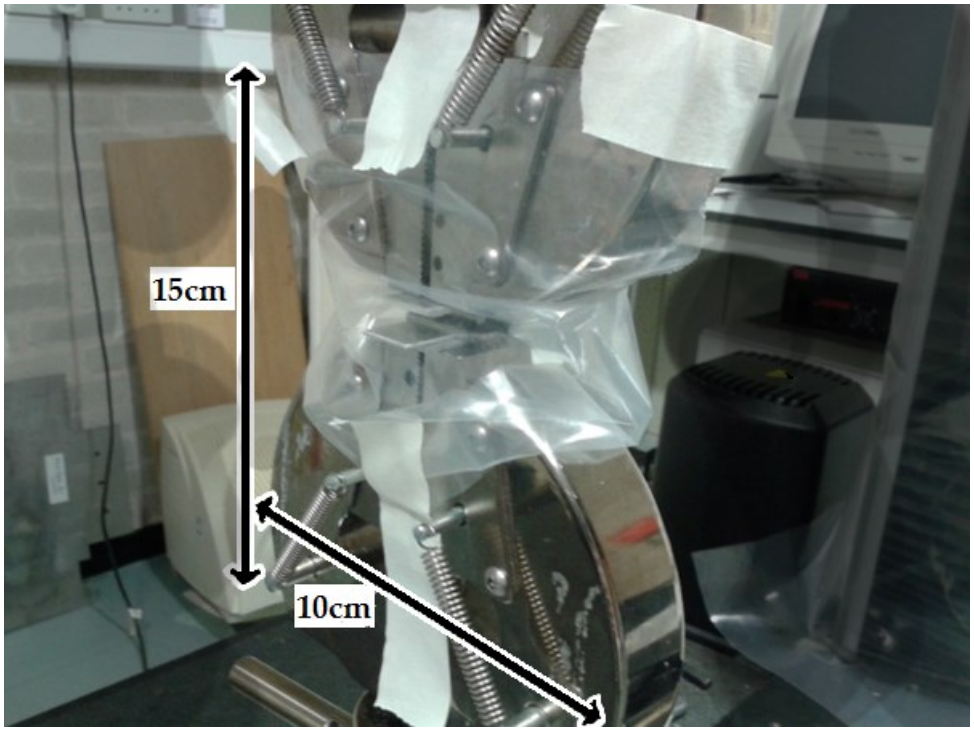

Figure 19
Flexure to failure of irradiated materials was performed in an environment isolated by transparent plastic bag to prevent any dust particles from within the sample entering the air upon sample failure.

3.4.1.5. Tensile Strength

Fibres were tested according to ASTM C 1557 – 03 (2013) [66]. For Nicalon and KD-1 fibres, the mounting tab method described was used. A thin card was cut into small strips 3 cm long by 1 cm wide with a central gap 1 cm long by 0.6 cm wide (as in figure 20, after Nozawa et al [29]). The function of the tab is to permit handling of very thin fibres and attachment to fixtures, which is otherwise prohibitively difficult. Fibres were attached at either end of the tab using locktite superglue and the tab was placed in the grips of the tensile test machine. After being secured, the tab is cut on either side so that the fibre can be loaded by the machine. For KD-1, testing was performed using a 1 Newton load cell (with the rig shown on figure 21) at a rate of elongation of 0.2 mm/minute on non-irradiated samples, vacuum irradiated samples and air irradiated samples (as described in section 3.1.2.). SCS-6 fibres were broken using an ESH servo-hydraulic testing machine with a1 kN load cell and a 100 Newton range and a rate of elongation of 0.05 mm/minute (as in figure 22). Irradiations were carried out using a degrader to achieve the same peak dose as for α-SiC of 0.0007 dpa at 400 ^{o}C.

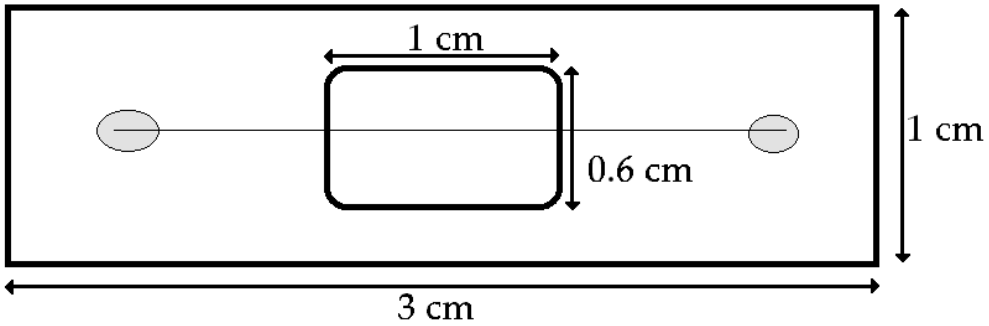

Figure 20
Mounting tab geometry as used for KD-1 and Nicalon fibres tested in tension.

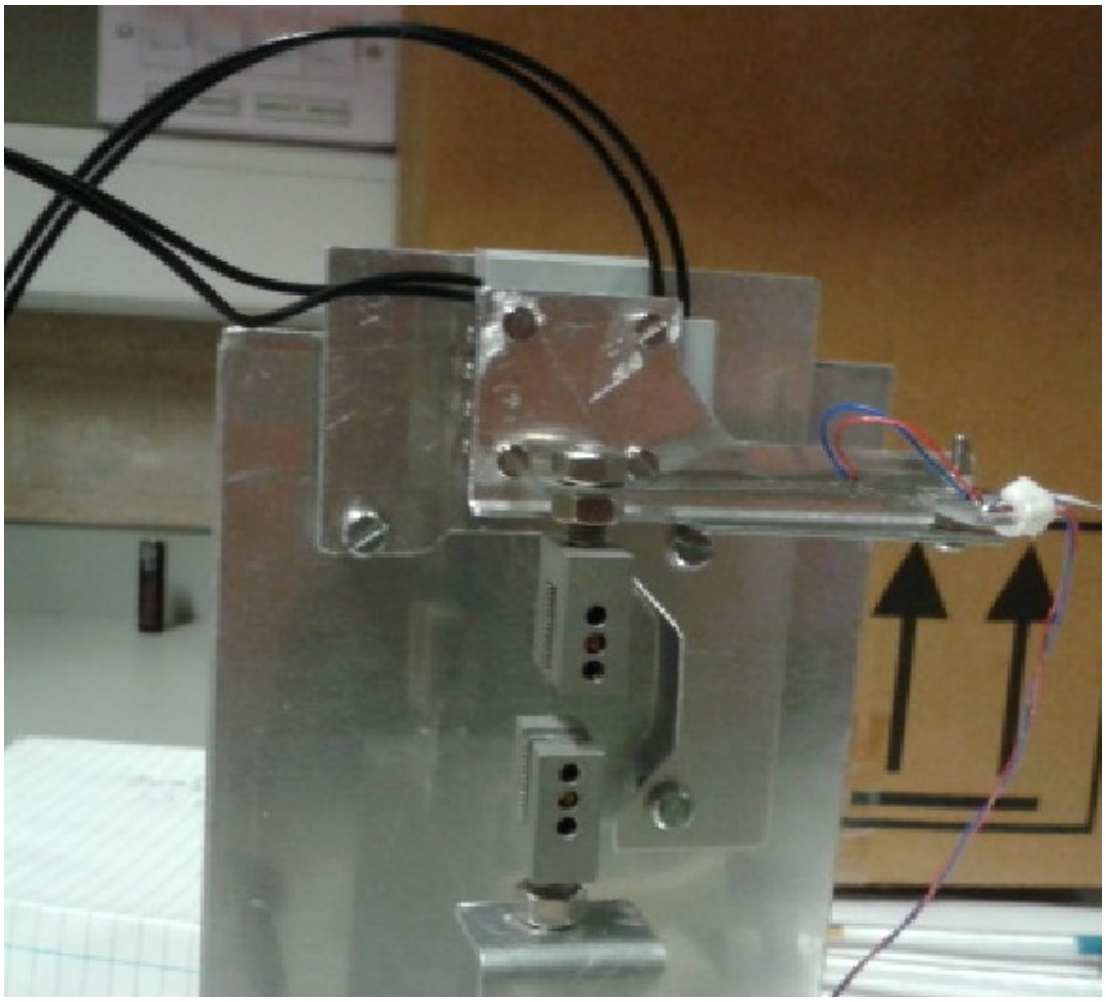

Figure 21
Thin fibre tensile tests were performed with this setup.

Figure 22
ESH machine used for testing SCS-6 fibres in tension, grips not shown.

3.4.2. Weibull Analysis of Vickers Microhardness and Thin Fibre Tensile Test Results

The results from Vickers indentation in α-SiC were fitted to a Weibull cumulative distribution function. This choice of distribution is common in experimental statistics because of the high generality of the Weibull fit; many functions (the true distribution of hardness values among them) can be well approximated using a Weibull plot (e.g. Dodson)[62]. In practice, this is done by plotting the log of the experimental data against the left hand side (LHS) of equation 3. A linear fit of the graph this creates can then be decomposed to obtain α and β using the right hand side of equation 3. Generating the LHS of equation 3 is typically done using an approximation of F(x) such as the median rank, which is (i – 0.3)/(N+0.4) where i is the rank of the measurement x and N is the total number of measurements (as detailed in B. Dodson (1994)[62]).

$$F(x) = 1 - e^{-\left(\frac{x}{\alpha}\right)^{\beta}}$$

$$\frac{1}{1 - F(x)} = e^{\left(\frac{x}{\alpha}\right)^{\beta}}$$

$$\ln\left(ln\left(\frac{1}{1 - F(x)}\right)\right) = \beta \ln(x) - \beta\ln(\alpha)$$

Equation 3
Weibull cumulative distribution function F(x) has a shape determined by parameters α and β.

In practice, the parameters α and β are derived from experiment to produce a distribution that approximates the experimental results. With f(x) representing the probability of performing a test of a material property (in this case Vickers hardness) on a material that gives result x a particular failure, the interpretation of these components is as follows; β, the Weibull modulus, represents the variability in this material property. A high β indicates a low degree of variation (so that the Vickers hardness in this case could be represented well using a single value), whereas a low β indicates a high degree of variability. α, the shape parameter, stretches the distribution. Compared to the normal distribution, the Weibull distribution can (using the parameters derived from the results data to be fitted) fit a wider variety of function shapes than the normal distribution. (see e.g. Dodson[62]).

3.4.3. Student T-Test for Vickers Microhardness Test Results

A Student T-Test was used to compare irradiated and non-irradiated data from the Vickers microhardness measurements. The 2-tailed Student's T-Test used in this work compares the likelihood of two samples of data being from the same distribution (hence the same mean value). The form used via Excel is detailed in equation 4. Using this function, two sets of data with different sample sizes can be compared to find the probability that they belong to the same distribution.

$$t = \left(\frac{1}{\sqrt{\frac{1}{n_1}+\frac{1}{n_2}}}\right)\left(\frac{\overline{X_1}-\overline{X_2}}{\sqrt{\frac{\left(\left(\sigma_{X_1}\right)^2+\left(\sigma_{X_2}\right)^2\right)}{2}}}\right)$$

Equation 4
The Student T-Test, where t is the probability that the two samples of data belong to the same distribution, n_1 and n_2 are the number of samples taken from group 1 and group 2, respectively, $\overline{X_1}$ and $\overline{X_2}$ are the means of each group and σ_{X_1}, σ_{X_2} are the standard deviations of each group.

3.4.4. Irradiating Material Samples using the MC40 Cyclotron

3.4.4.1 Ion Source

Ion beams can come in a range of energies, ion species and currents depending on ion source. The intended application must be matched to the facilities available in order to conduct the most productive tests. The ion source used for this study was an MC40 cyclotron (as in figure 23). It is capable of giving an output of up to 20 μA of protons at an energy of 40 MeVs (mega electron volts), which represents a much lower current range but much higher energy range than one of the main competing accelerator types (an electrostatic accelerator) used for materials science irradiation research. The cyclotron relies on orbital resonances of accelerated ions trapped in a magnetic field to drive them to high energies using intense radio waves (see e.g. [52] for more information). This means that only a distinct number of energies can be extracted from a cyclotron reliably (approximately 12 MeVs, 24 MeVs and 36 MeVs in this case) though in practice there are other resonances that can be accessed at the cost of much lower current and much greater effort (such as 3 MeVs). By contrast, an electrostatic accelerator can tune its energy quite precisely as well as delivering much higher currents. However, electrostatic accelerators become increasingly more expensive the higher the energy they can operate at so that in practice they only operate up to a few MeV. Electrostatic accelerators are therefore well suited to surface irradiation of materials made of light elements (where great amounts of damage can be caused) and cyclotrons are better suited to penetrating irradiations (particularly for metals which are much more difficult to penetrate with ions). Thus a cyclotron is particularly well suited for emulating the radiation conditions present in the

high altitude/space environment. Fundamentally the limit on currents possible with either system is due to the way in which ions are produced; using a filament at high voltage to strip atoms of their outer electrons exerts tremendous stress on the filament itself.

Figure 23
MC40 cyclotron taken from [69] with capability of up to 40 MeV beam energy, beam spreading over target areas in excess of 2 cm by 2 cm and currents up to 60 μA.

3.4.4.2. Air Irradiation with Waterblock

Air irradiations were performed using the water block setup illustrated in figure 24. Cooling is provided both from room temperature water circulated through the block itself as well as air blown across the aperture. Care must be taken in practice with this setup in clamping SiC samples since they are easily cracked under the stresses of the clamp/may be susceptible to increases of this stress due to thermal expansion when the beam is running. To counteract this, the samples were wrapped in a thin layer of aluminium (whose effect on the beam energy was taken into account when designing the incident beam energy to get 10 MeV protons after passage through the aluminium foil).

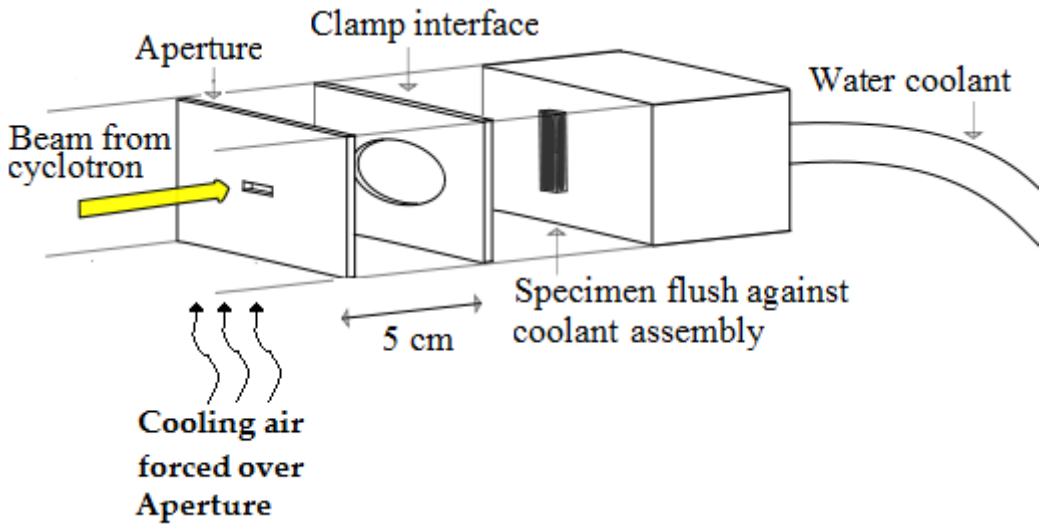

Figure 24
The mount for holding samples during irradiation is cooled using room temperature water through the water block and a jet of air across the aperture.

3.4.4.3. Chamber for Vacuum Irradiation

A steel vacuum chamber was converted for vacuum irradiation of samples. In practice this was much more difficult to implement than the air irradiation equipment. An aperture was manufactured in order to control the beam dimensions incident on the target. The beam energy dissipated (as heat) through the apertures was roughly twice that dissipated in the sample. Since the aperture parts have to be electrically insulated from each other in practice by silicon rubber (which would not withstand high temperatures), active cooling was required. This was done using thin coolant pipes routed through a flange on the side of the chamber (as in figure 25). A heating element was used as the mount for the samples to be irradiated so that the samples could be heated directly to a desired temperature. An ion beam from the cyclotron (a) is made to fit a rectangular area using the apertures (c), which are a pair of aluminium blocks around 2 cm thick. Bore holes were made in these blocks to permit the passage of cooling air from outside the chamber via piping (b) that is connected via flange to an external air pump (e). The target is mounted directly to the front face of a heating element (d) which may be heated up to around 700 ^{o}C if a more robust aperture is installed. In practice it was found that the silica gel insulation for this aperture was too delicate to survive the highest temperatures of the heating element in the vacuum chamber. For low temperature runs the heating element acts as a good conductor and heat bath for the target.

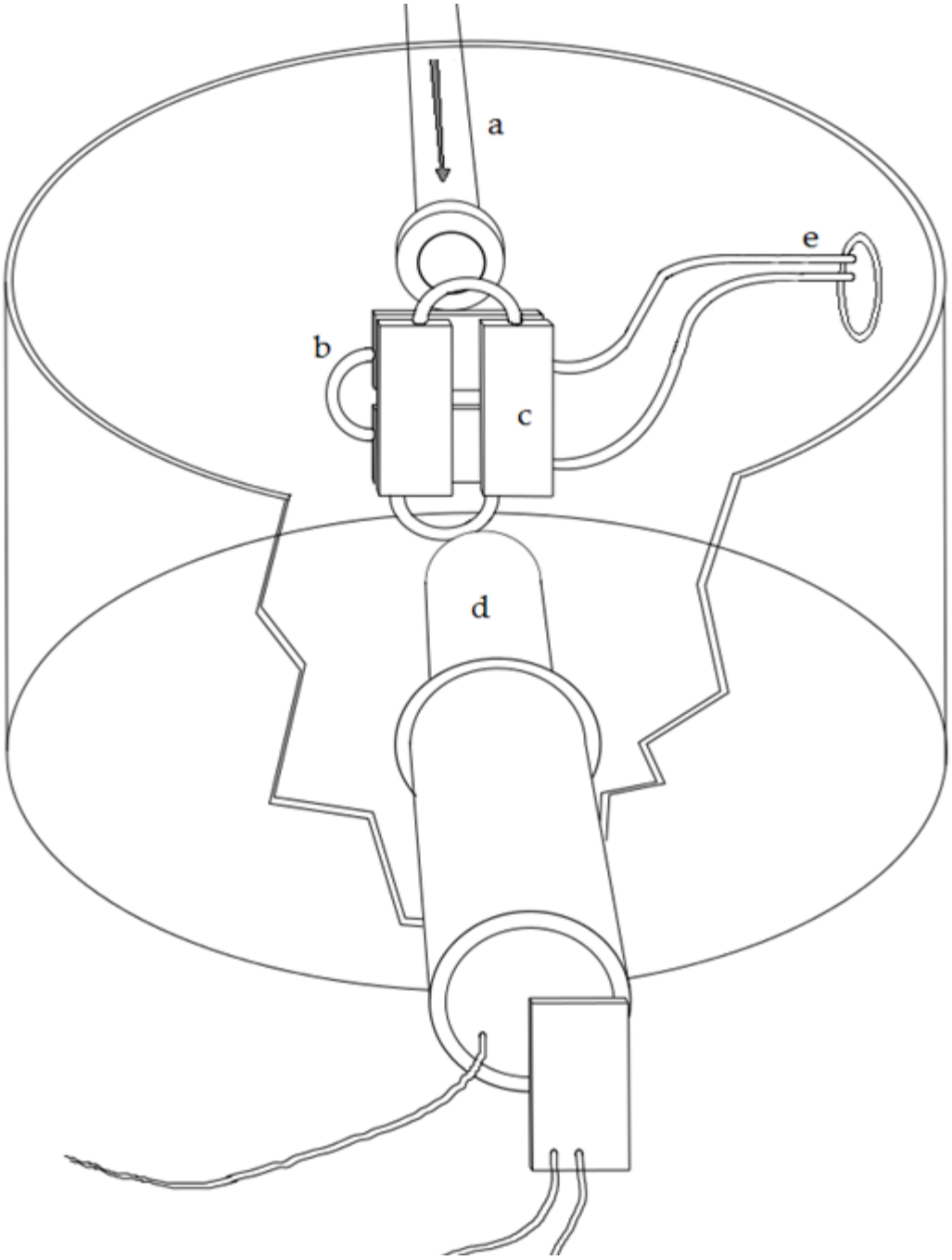

Figure 25
Vacuum irradiation was performed using a sealed chamber. An ion beam from the cyclotron (a) is permitted to enter the chamber. The beam must be trimmed to a rectangular shape (since it is naturally a more irregular shape closer to elliptical) which is performed using an aperture (c) cooled by air supplied by sealed coolant pipes (b) and routed through a flange in the chamber wall (e) to be pumped externally. The rectangular beam profile then reaches the target mounted (via an intermediary copper block) to the heating element (d).

The components inside the chamber directly in the path of the beam (the apertures and target face) must be electrically insulated from the chamber body in order that the beam current absorbed in each aperture face and the target face can be measured. To this end, a thin PTFE sheet was used behind the copper block at the target face and silica gel between the apertures (as in figure 26). The setup within the chamber during operation (including alumina heat-shield and pipes for air cooling of apertures) is shown in figure 27.

Figure 26
Picture of internal setup of the vacuum chamber without air coolant pipes attached to the aperture or alumina insulator over heating element. The copper layer to which the sample being irradiated is mounted directly is insulated using a thin PTFE sheet from the heating element. Thermocouples were attached to the degrader and target face.

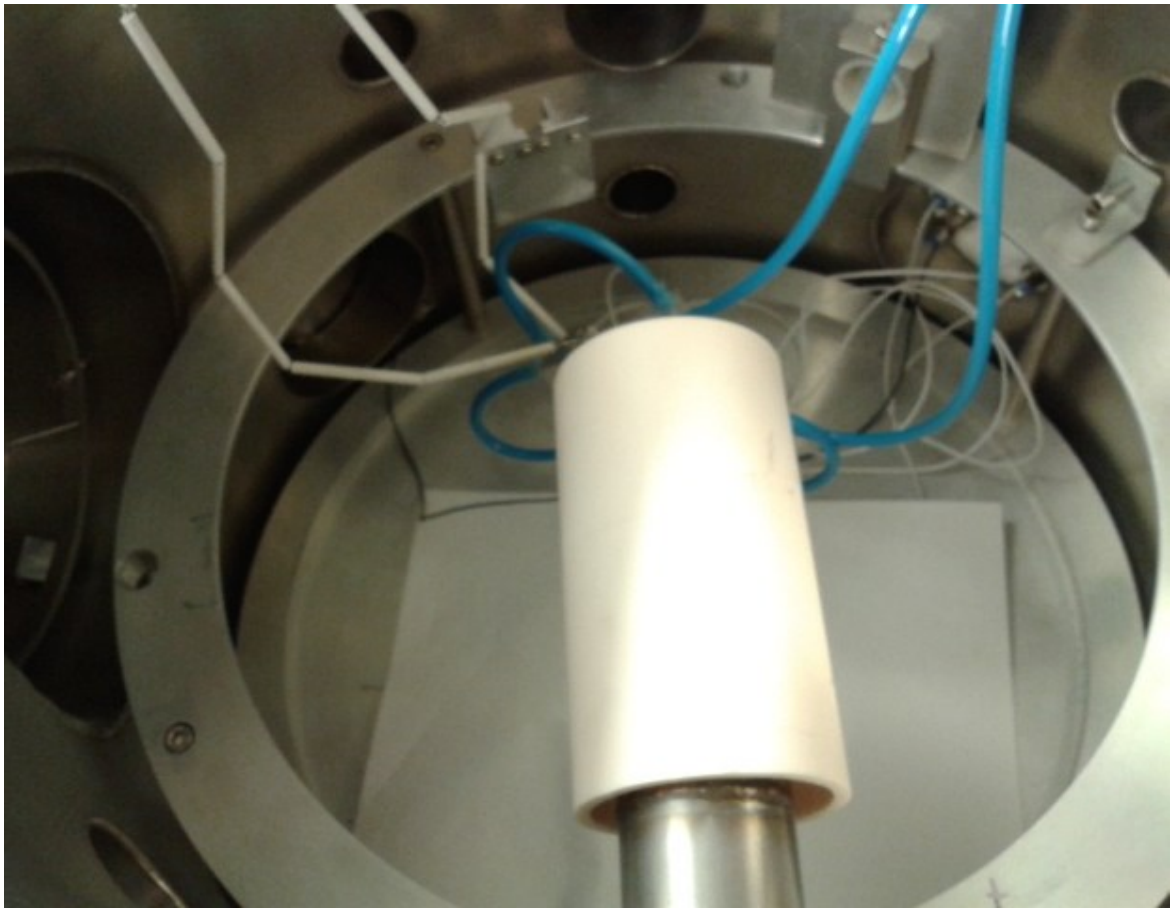

Figure 27
Here the setup is shown with alumina insulator and air coolant pipes in place. The alumina insulating sleeve both improved the maximum temperature attainable with the heating element and provided some protection for the coolant pipes (which could not be brought above ~100°C).

3.5. Computational Modelling

3.5.1. Modelling Temperature of Sample during Irradiation

3.5.1.1. Finite Difference Scheme for Waterblock Setup

It is important to know the temperature of the samples during irradiation since mechanical changes during irradiation are also dependant on temperature [24,25,30-32,34,35]. Owing to the compactness of the setup a direct measurement of the temperature during operation with a thermal camera was not possible. Also it was conjectured that radiation from the experiment during operation may be enough to damage such a camera, which were prohibitively expensive to test this with. Using a thermocouple is also difficult since a reading must be taken slightly away from the surface on which the beam is incident (the effect on the operation of a thermocouple with an ion beam directly on it is unknown) so that the temperature in the centre of the sample must be inferred. It was thought that computer modelling could address this issue indirectly. The equations for heat conduction, whilst often difficult to solve by hand, have a relatively straightforward physical interpretation (for the finite element version of this as used here see e.g. R. Leveque [56]). For the majority of a material where no heat production occurs, equation 5 holds – the left hand side, for each infinitesimal point in a material, just takes the average temperature of it and neighbouring infinitesimal points and replaces the original value with this average. If a computer program can be used to do this many times with the temperature at each point in a large lattice representing the system to be modelled, eventually it will tend to settle into a steady state no matter what the geometry or starting values are.

Hence, so long as equation 5 holds, repeating this procedure should eventually give the correct temperature distribution for the system. This is commonly called a relaxation method.

$$\frac{\partial^2 T}{\partial x^2} + \frac{\partial^2 T}{\partial y^2} + \frac{\partial^2 T}{\partial z^2} = 0$$

Equation 5
Laplace's equation is perfect for computational modelling provided the system satisfies the right conditions.

The reason this works is that the Laplacian (left hand side (LHS) of equation 5) tends to smooth any function it is performed on – equilibrium occurs when all temperature differences in the system are as small as possible (smooth). A model that takes into account the full features of the system must be based around equation 5 but also take into account the considerations outlined in table 14. Convective heat transfer with air across the front of the specimen is very difficult to model without being able to measure its effect directly. Inclusion of this may give corrections to the simulated temperature during air irradiation. The inhomogeneous version, relevant for the vacuum irradiation setup, of Laplace's equation is more difficult to solve. In equation 6, the additional term (called the inhomogeneous term) represents the continuous addition of heat dissipated by the ion beam as it stops in the sample. In practice, the heat production term was added after averaging for each cell in the model where heat is generated. Averaging cells without heat generation was done as per equation 5.

Table 14
Special features of the model for the current system and the approaches taken to accommodate them.

Extra Considerations for Modelling Actual System Compared to 2D Laplace equation	**Manifestation**
Geometry	Different 2-D layers of cells have different sizes.
Internal Heat Generation	Some cells have extra value added to them after taking average as per LHS of Equation 3.
Heat Sink from Water Cooling	Bottom layer set at room temperature (water flow is high enough that it can be treated as at close to room temperature where it meets the interior of the water block).
Convective Air Cooling Across Sample	Currently unaccounted for – thought to cause perhaps a 20 or 30 degree decrease in temperature from the temperature predicted in the model.

$$\frac{\partial^2 T}{\partial x^2}+\frac{\partial^2 T}{\partial y^2}+\frac{\partial^2 T}{\partial z^2}-\frac{aq}{C_p\rho}=0$$

Equation 6
This is the form of a heat conduction problem involving heat generation. where a is the thermal diffusivity, q the power dissipated from the beam, C_p the specific heat capacity at constant volume, ρ the density of the material in which the power is dissipated (the α-SiC sample).

Two different approaches to temperature modelling were employed in this project; a finite difference scheme (section 4.1.3.2.) using Microsoft Excel to model a 2D cross-section of a typical SiC material sample during irradiation mounted to the sample holder and a finite element model (section 4.1.3.1.) in 3D of the sample and sample holder using the COMSOL finite elements/computer modelling package.

The finite difference scheme used a grid of cells in Excel whose value represents the temperature. Each cell is given an initial value of temperature. The algorithm in equation 7 then loops over each cell in the grid, averaging over the surrounding cells (X_2 to X_5) and adding contributions from the internal heat generated by the ion beam S, assigning a new value to the cell in question. This process is repeated until $X_{1(\mathrm{new})}$ does not change appreciatively from $X_{1(\mathrm{old})}$, at which point a stable solution is reached. Boundary conditions can be included by giving cells at the edges the following exceptions to the above rules; for boundaries at a fixed temperature, the cell is merely given its initial value and not changed as the program loops, whereas for free boundaries the cells take averages of neighbours as normal but excluding any missing cells (at a wall facing vacuum and without an internal heat source term the average in equation 7 would read $X_{1(old)} + X_2 + X_3 + X_4/4$, since the material stops at the wall and a neighbour is therefore missed out). Internal heat sources can be added on as a constant contribution S to each cell effected (in this study the relative value of S was assigned to each cell in the path of the beam according to the energy loss profile of the ion as calculated by the Bethe equation (see section 2.3.2)).

$$X_{1(new)} = \frac{\left(X_{1(old)} + X_2 + X_3 + X_4 + X_5 + S\right)}{5}$$

Equation 7
The program loops over each cell in the grid, averaging over the surrounding cells (X_2 to X_5) and adding contributions from the internal heat generated by the ion beam S, assigning a new value to the cell in question. This process is repeated until $X_{1(new)}$ does not change appreciatively from $X_{1(old)}$, at which point a stable solution is reached.

3.5.1.2. Finite Element Simulation using the COMSOL Computational Modelling Package

The Modelling software COMSOL[58] was used to design a heat conduction model analogous to the vacuum irradiation setup (with 0.3 μA current 10 MeVs incident on a thin sample clamped against a copper plate connected directly to the heating element as detailed in section 3.3.2.3.). COMSOL is a finite elements package with many modules available to address specific types of problems within physics and engineering; the heat transfer module was utilised in this study. Material properties were input manually for each connected component modelled (sample, copper mounting block and heating element), heating behaviour of the ion beam during irradiation was supplied and a 3D model of the setup was produced as inputs for the program. COMSOL gave the temperature distribution across the setup and experimental sample during irradiation as an output. The COMSOL program functions by loading solutions to versions of problems in question with very simple boundary conditions (for the heat conduction module, heat conduction in one dimension) and then the full object to be modelled is separated into a series of small domains for which these boundary conditions must be satisfied. The parameters of the function approximating the temperature across one such domain are matched with those of each neighbouring domain so that at the point where they intersect the temperature is the same. When this process is completed over the entire mesh of domains for a given material, the temperature at any given point in the mesh approximates the temperature of the physical component being modelled at that point. The accuracy of the approximation increases as the number of domains in the mesh is increased (requiring longer processing time on the computer modelling the system). Finite

element packages typically have the advantage of easily incorporating complex shapes, which was necessary particularly for the cylindrical target setup to which samples were mounted for irradiation.

3.5.2 Modelling Irradiation Dose and Penetration Using TRIM/SRIM Computational Modelling Software

The program TRIM[57] was used to model radiation damage in SiC materials for alpha particle and proton beams of various energies. This was output in the form of plots of particular particle paths through the material for each ion type and parameter, with all particle paths modelled starting from the same point. Most of the energy is lost in the low energy regime, as seen in the peaks on the right hand side of each dpa/depth graph (and as discussed in section 2.3.2.). Figure 28 shows a typical output from the TRIM program with dose as number (of vacancies), per angstrom of target material for one incident ion travelling through. In practical application to prediction of radiation damage, this graph is converted to total absorbed dose by normalising it for the conditions of the irradiated specimen. TRIM is a computational modelling software package that uses the Monte-Carlo method with a square grid of point particles representing the medium to be tested[57]. The relative number density of each element within the target material is input by the user and uniformly distributed within the grid. TRIM then simulates the passage of a single ion, whose type and energy is input by the user, and traces its path through the lattice. When the ion comes within range of an atom on the lattice the probability of an interaction is approximated using a statistical process (the initial grazing angle in which the atom is hit is assigned by a random number). This results in the ion being deflected and the process is repeated for the ions passage through the material along its altered path and at reduced energy (since some portion is imparted to the lattice atom during the original collision). In this way, the passage of a test ion through the simulated material is traced out, with the total number of displaced lattice atoms and penetration depth of the

ion recorded by the program. By repeating this process many thousands of times an average number of displacements per incident ion and an average penetration depth are generated; these are the main outputs from the program. The average number of displacements per ion was used to calculate the dose in dpa for irradiated samples and the average penetration depth was taken directly as the penetration depth of the ions and used in design of the irradiations.

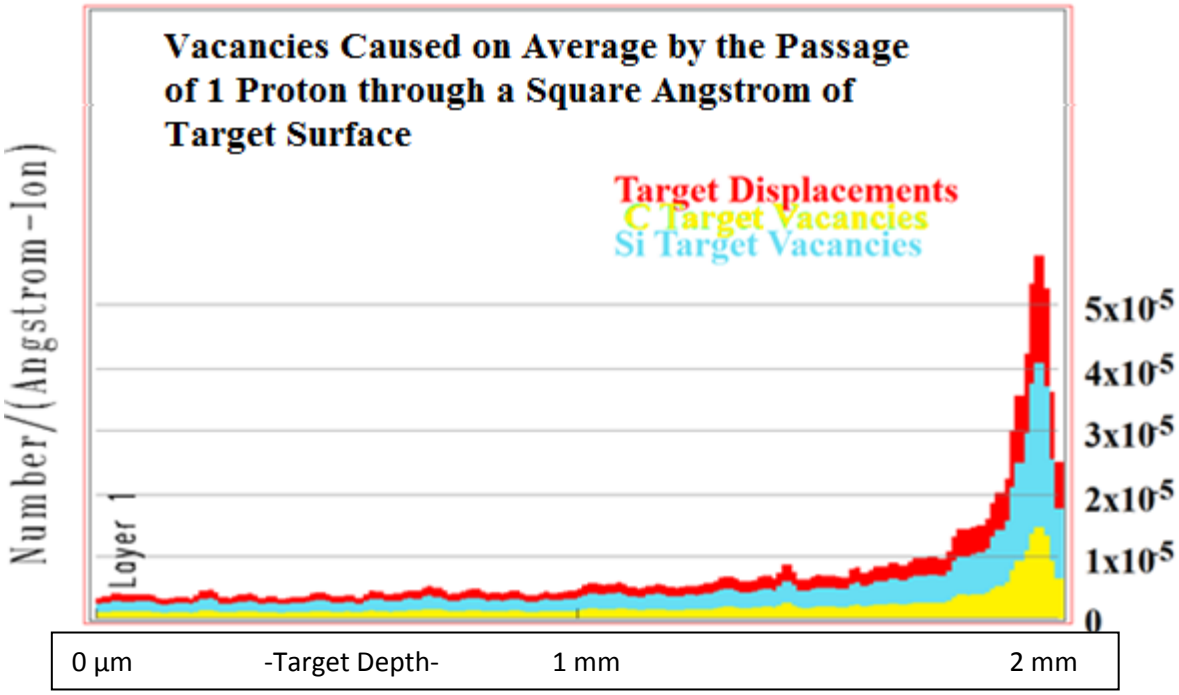

Figure 28
Typical output from TRIM, in this case for a 22 MeV proton through 2 mm SiC. The yellow area represents Si atoms displaced, the blue are Carbon atoms displaced and red the total number of displaced atoms.

Going from TRIM output to total dose requires that the incident current and the surface area it is spread over be converted into number of ions per square Angstrom per second. There are $6.24*10^{12}$ elementary charges reaching a surface per second that has one μA of ion beam incident upon it (providing each ion has a charge of +1 which is not the case for α particles but protons were used for all data collecting runs in this study). 1 cm^2 contains 10^{16} square angstroms. On average then, for the air irradiated samples in this study, during irradiation a proton would pass through a given square angstrom of target surface once every 1280 seconds. Figure 29 shows the TRIM output taking this into account so that dpa/hour for a given current (in this case 1 μA).

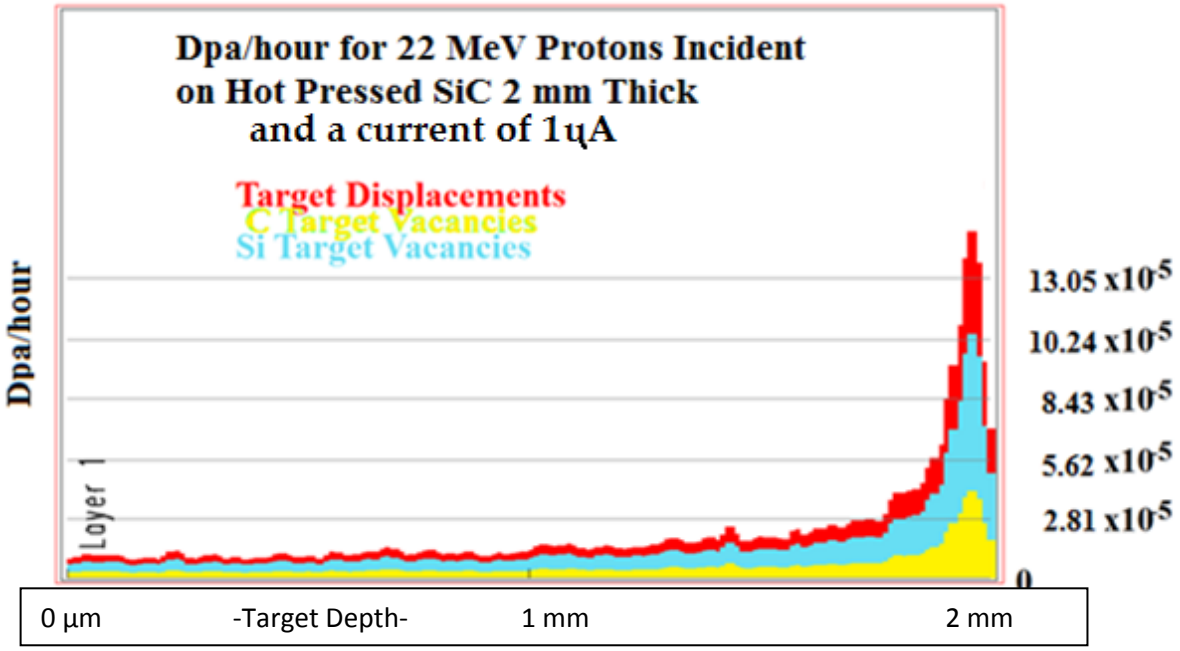

Figure 29
Total dose in sample for 22 MeV per hour at 1 uA current as a function of depth in the material. For the majority of the material, the dose rate is around 0.00001 dpa/hour, but is around 0.00015 dpa/hour just beneath the surface (more than the resolution here but only over about a micron, so the true peak was not deemed controllable).

4. RESULTS, THEIR INTERPRETATION AND ANALYSIS

4.1. Analytical Results and Computational Modelling

4.1.1. Absorbed Dose of Irradiated Specimens

The program SRIM/TRIM was used to find stopping distances, power dissipated and damage in the materials tested. Typically, the more massive ions cause more damage for the same beam power as lighter ions. The TRIM outputs for 10 MeV protons stopping in SiC (figures 30(a) and (b)) and 10 MeV α-particles (figures 31(a) and (b)) stopping in SiC are given here, the full set of simulation results can be found in Appendix A. These outputs are given in two components: (a) is the spread of beam particles through the sample (which grows significantly for lower ion energies) whilst the (b) figure components are graphs showing the calculated dose as a function of depth through the sample (as explained in section 3.4.2.) .

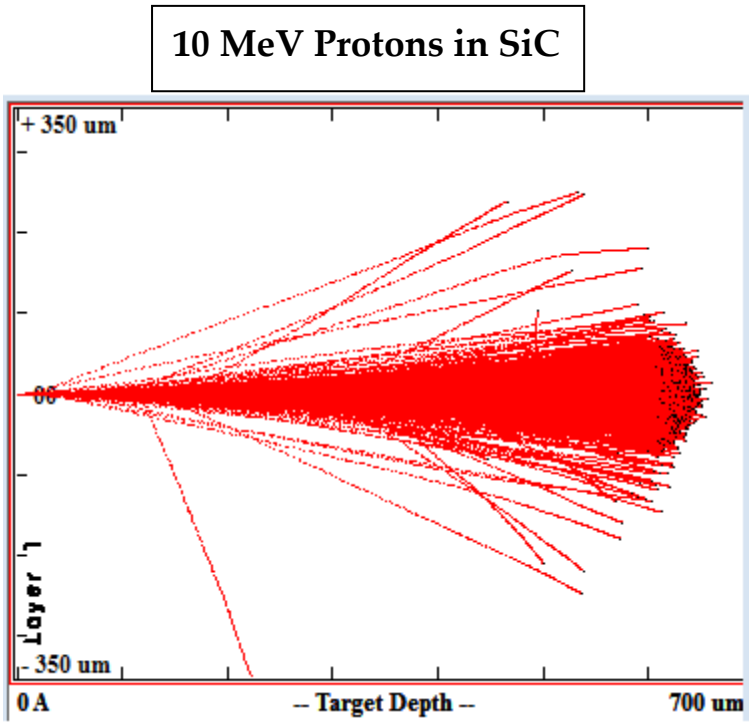

Figure 30 (a)
10 MeV proton paths through SiC starting with an infinitely thin beam using TRIM. Around 4000 simulated proton paths are show, the average penetration is 630 µm.

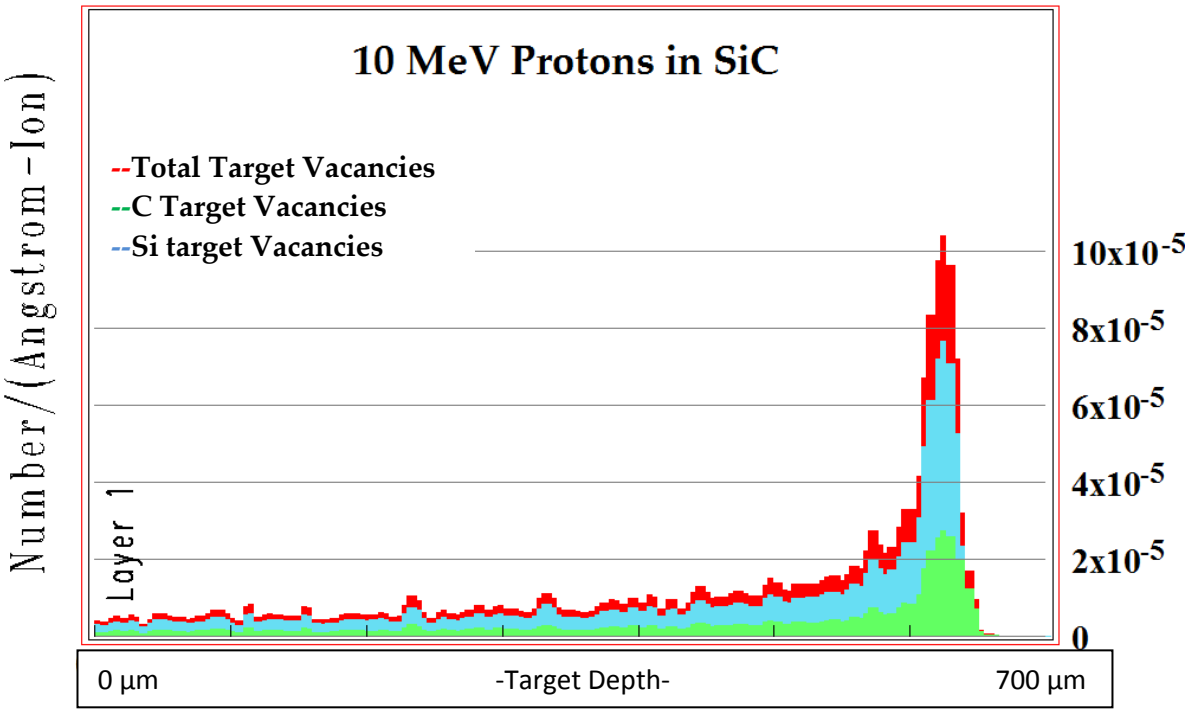

Figure 30 (b)
Damage as function of depth through SiC for 10 MeV protons.

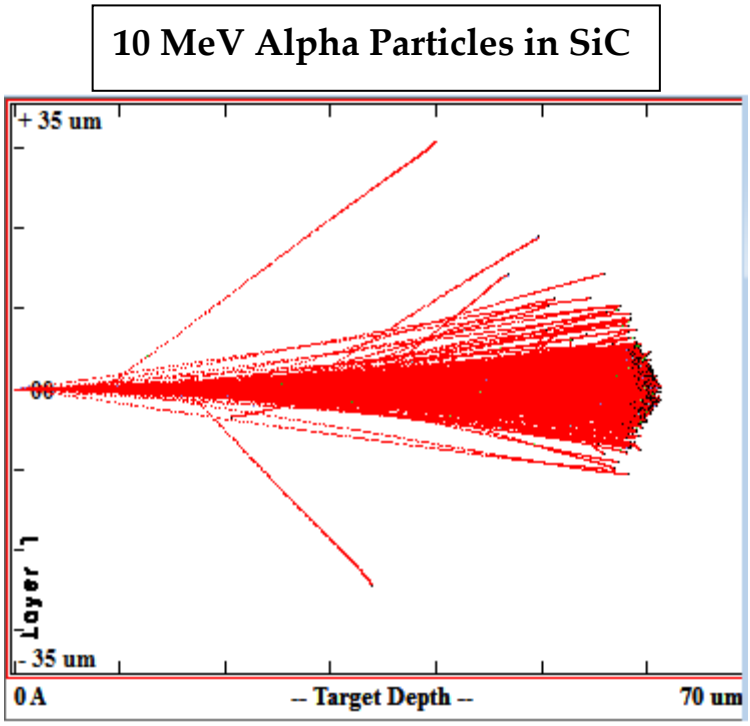

Figure 31 (a)
10 MeV alpha particle paths through SiC starting with an infinitely thin beam using TRIM. Around 4000 simulated proton paths are shown, the average penetration is 870 μm.

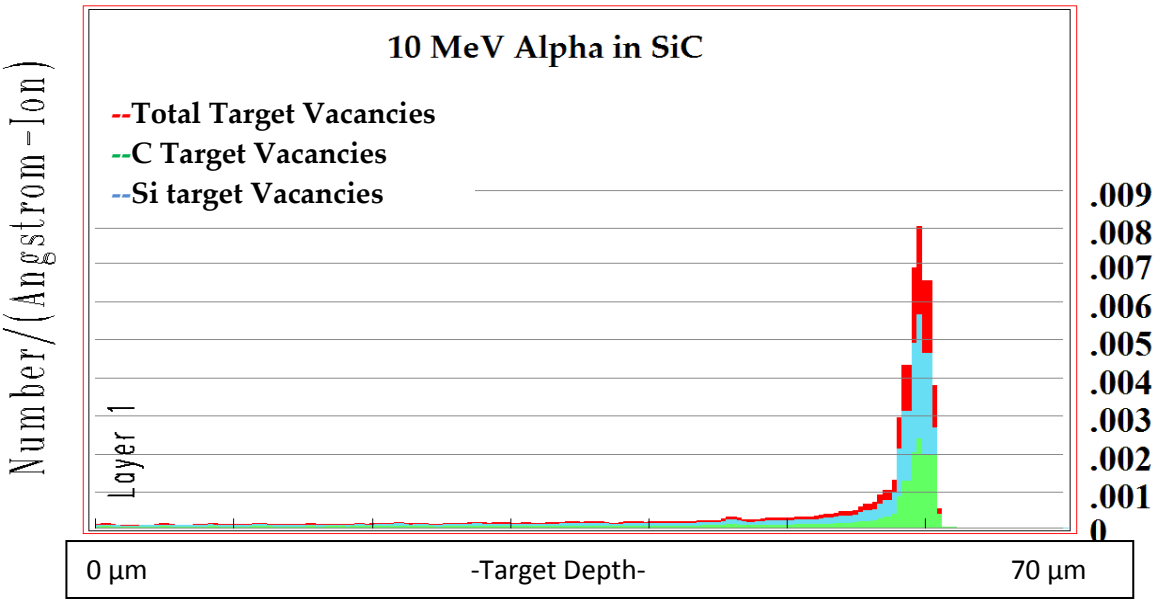

Figure 31 (b)
Damage as function of depth through SiC for 10 MeV alphas.

4.1.2. Modelling of Sample Temperature during Irradiation

4.1.2.1. COMSOL Model for Temperature Distribution in Apparatus during Vacuum Irradiation

A computational model was produced with the COMSOL Multiphysics software using the heat transfer module [58]. The model represented the end portion of the heating element and served as a means to confirm the validity of the finite difference scheme (temperature drops very quickly from the irradiated target). This was split into 3 portions: the sample, the thick copper block to which it is mounted and the steel heating element to which this is connected. Figure 32 shows the temperature distribution through the heating element during irradiation with 1 μA protons (after temperatures equilibrate, which was measured by thermocouple to take approximately 5 to 10 minutes depending on beam stability). Figure 33 shows a cutaway of the thermal model of the heating element with isothermal surfaces – heat flow occurs normal to an isothermal surface [56] so heat flows directly from one isotherm to the next. Understanding the variation of temperature inside the heater block with depth is important if the addition of a thermocouple directly behind the sample is made (in practice this could be done using a bore hole through the copper plate to which the specimen is mounted).

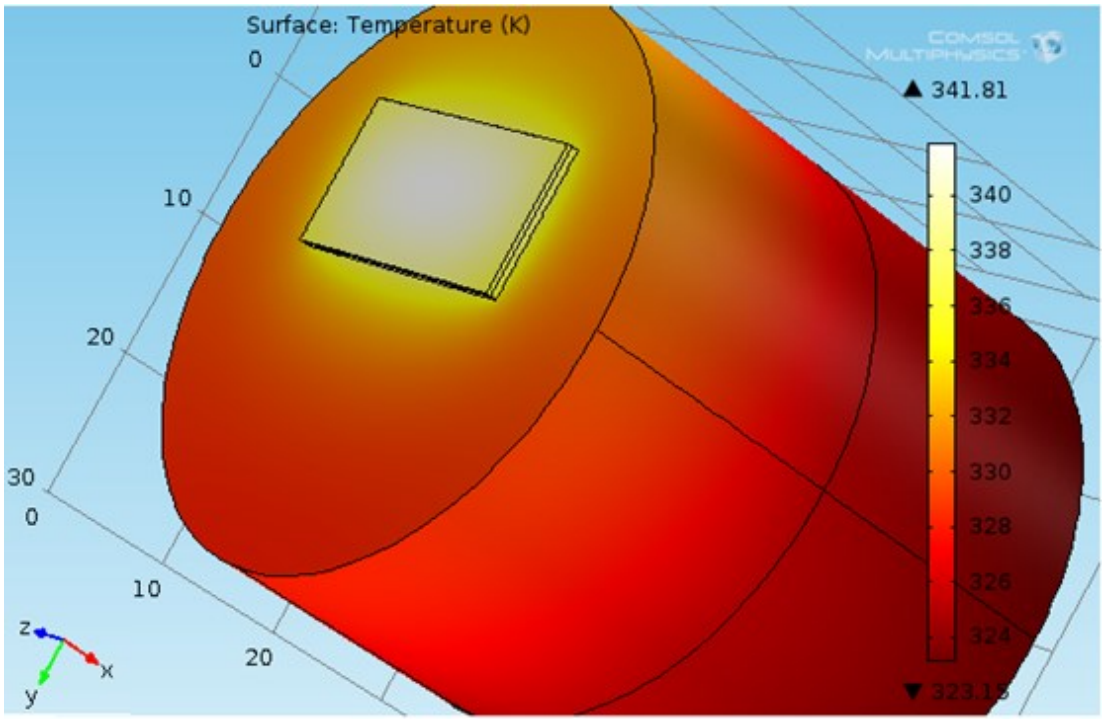

Figure 32
COMSOL simulation of temperature after continuous operation at 10 watts for a 2 cm by 1 cm thin sample mounted to the target setup. This was modelled as a copper block that connected directly to the end portion of the steel heating element (separated by a line through the cylinder in the picture).

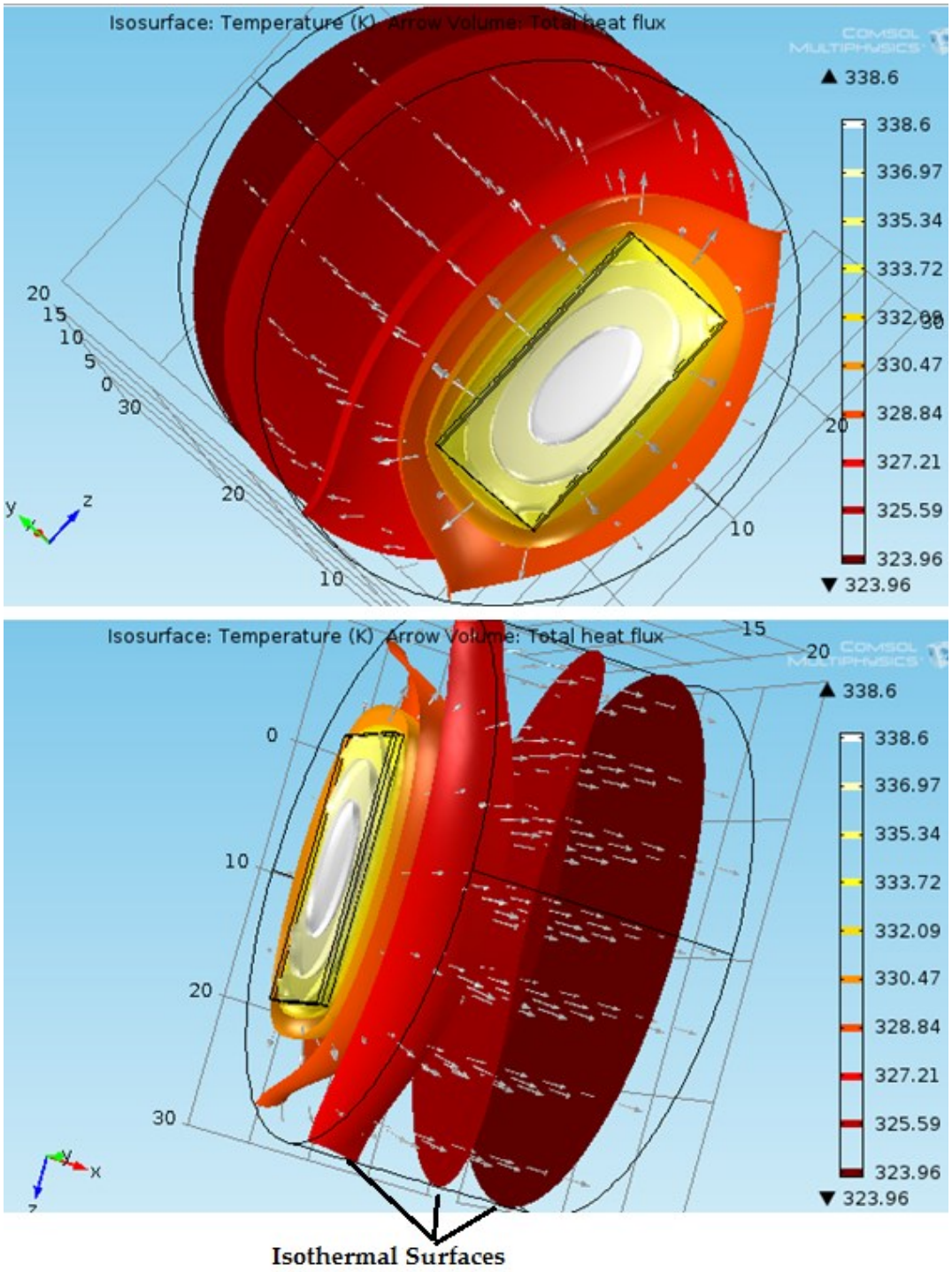

Figure 33
Isothermal surfaces on COMSOL temperature model.

4.1.2.2. Finite Difference Method for Temperature in Waterblock during Air Irradiation

A finite difference model was produced (see e.g. [56] for finite difference modelling) to find the temperature as a function of position within the sample and copper block attached to the heating element (using the model described in section 3.5.1.1.). 10 different layers of cells were used for this model, each connected to the ones adjacent (above and below) so that the model took the 3 dimensional effects of the real system into account. The central slice of this is shown in figure 34 – the base (white) is kept at room temperature whilst the sample gets to around 85 ^{o}C in the sample area (shaded).

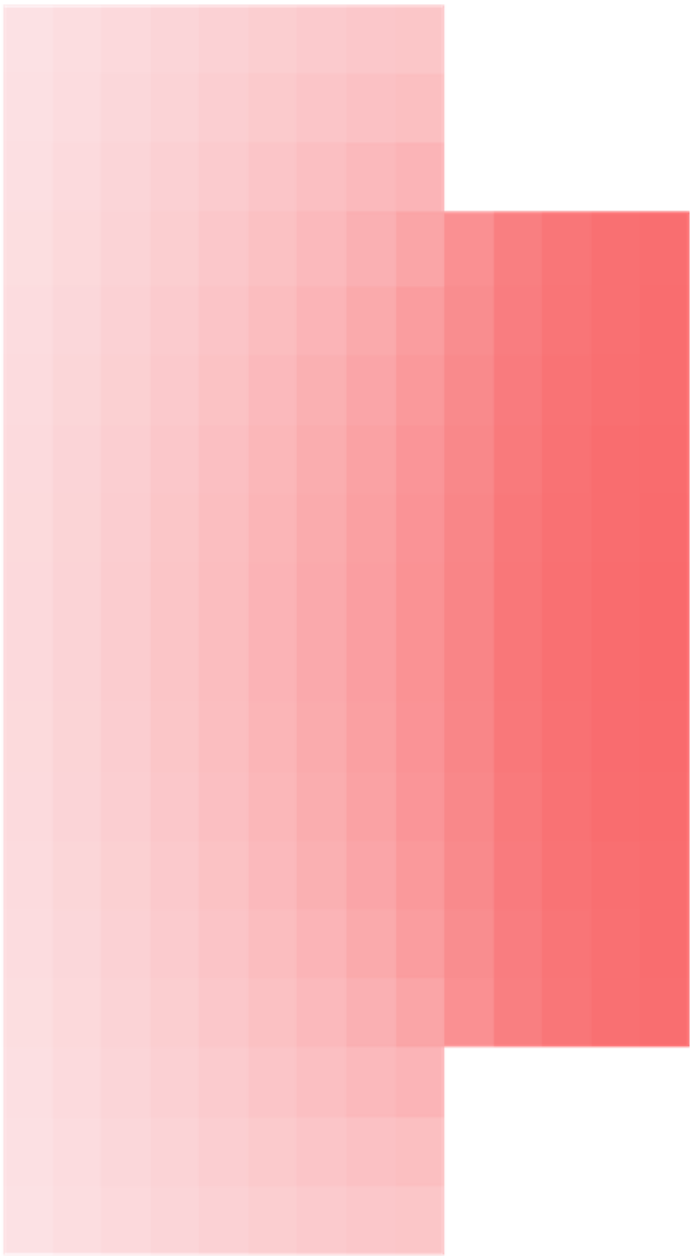

Figure 34
A 2D slice through the waterblock system was modelled using a finite difference scheme. As predicted, the temperature variation vertically here is much smaller than the horizontal. The smaller right-hand section of this represents the sample, heated by a beam of protons approximated as a series of sources through the sample. The temperature peaks at the right of the sample (red) and drops almost to room temperature at the water interface in the cooling block (pink).

4.2. Radioactivity and Activation Measurements

4.2.1. Radiation Measured in Direct Vicinity of Chamber during Vacuum Irradition

Typically, during operation, the radioactivity in the direct vicinity of the cyclotron can be high enough to be immediately hazardous to human health. A He3 neutron detector was used to measure the neutron flux from the decay of short lived radioisotopes produced when 10 nA of protons were incident on an aluminium plate (connected directly to the heating element). At a distance of about 1 meter, the radiation dose equivalent was about 0.01 Sieverts an hour, increasing to 0.08 Sieverts an hour at ~30 cm. Typical operating currents are in the region of 5 μA or more; measurement at this flux may damage a neutron detector but since conceptually there is no reason that neutron flux should not increase linearly with current, it is expected that a neutron flux during operation at a distance of about 1 meter from the experiment may cause the equivalent of 5 to 10 Sieverts of absorbed dose per hour should a human be present at this distance, not accounting for gamma rays and x-rays. It is for these reasons that large distances and radiation shields must be used during ion irradiation experiments, which greatly compounds the cost and complexity of producing ion beam facilities (which is part of the reason why there are so few currently operating in Universities around the world). The MC40 cyclotron uses around 1.5 meters of concrete and distances in excess of 5 or 10 meters between the control room and the nearest experiments in order to ensure safety.

4.2.2. Gamma Radioactivity of Irradiated Samples

Gamma ray spectra were taken using a germanium semiconductor detector (see e.g. Knoll [67]). SiC has the advantage of low activation compared to alternative proposed reactor materials which was reflected in measurements of the gamma spectra taken. Figures 35-38 show the spectra from several different irradiated samples. Peaks in the spectra are indicative of specific radioisotopes produced during irradiation. The peak at 845.41 KeVs with others suggests cobalt which would be produced from iron – minute iron impurities may therefore exist in the samples.

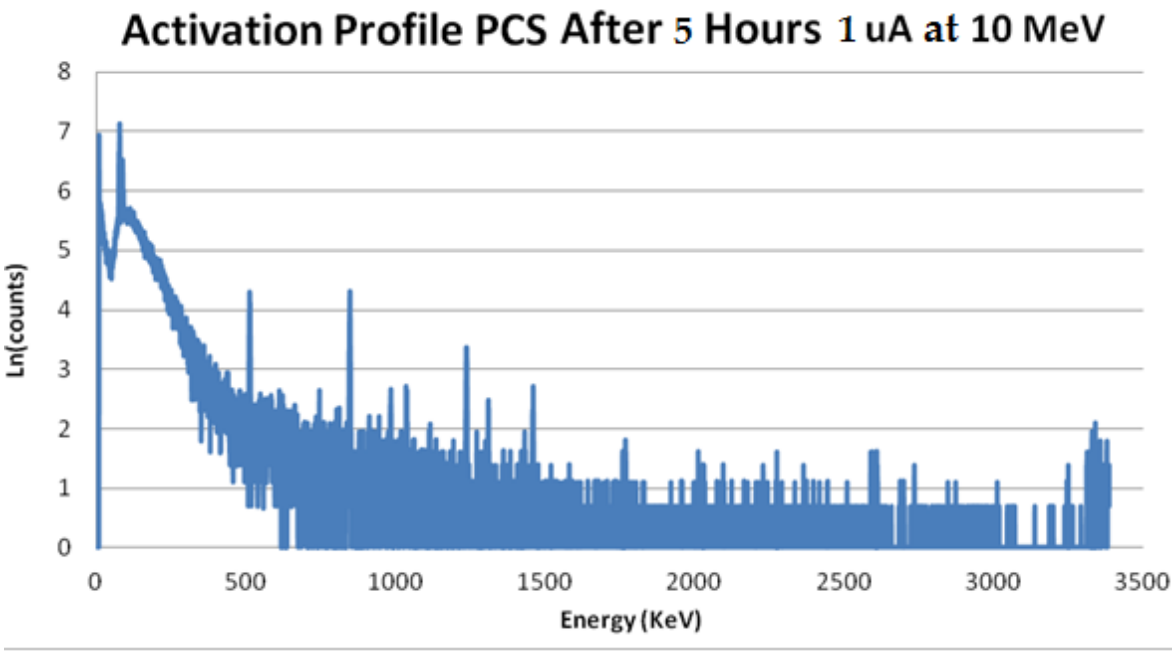

Figure 35
Gamma emissions from PCS sample after proton irradiation. The total average dose was 0.0007 dpa.

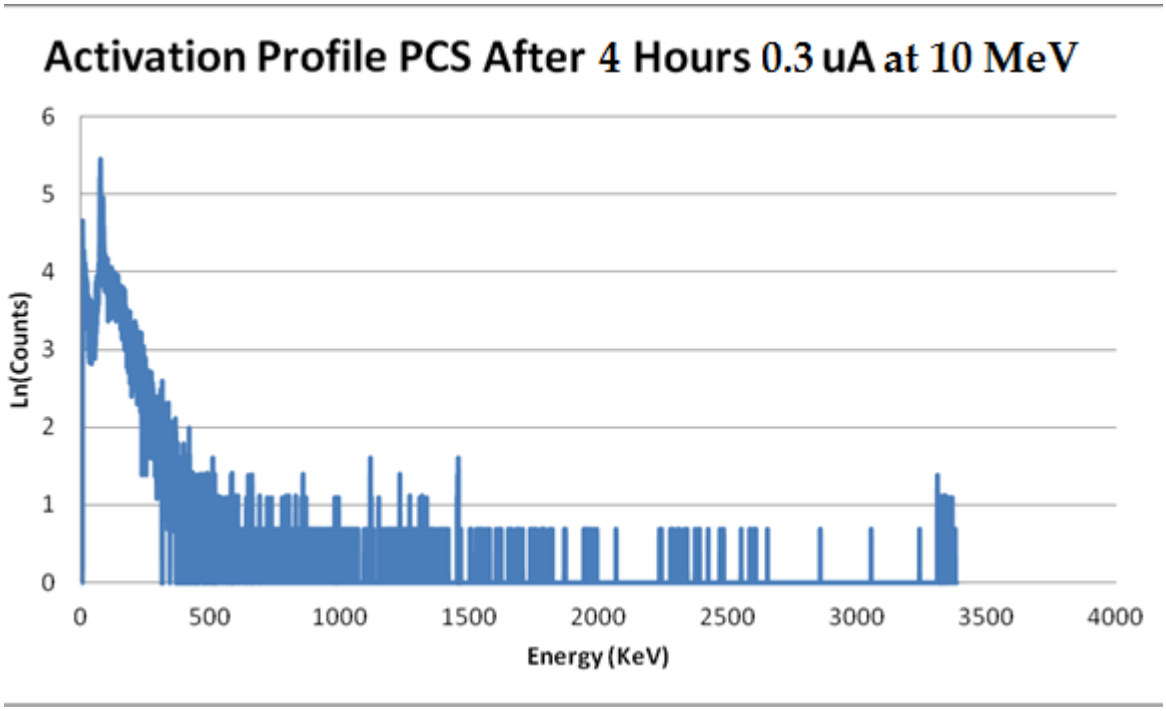

Figure 36
Gamma emissions from PCS sample after proton irradiation. The total average dose was 0.000021 dpa.

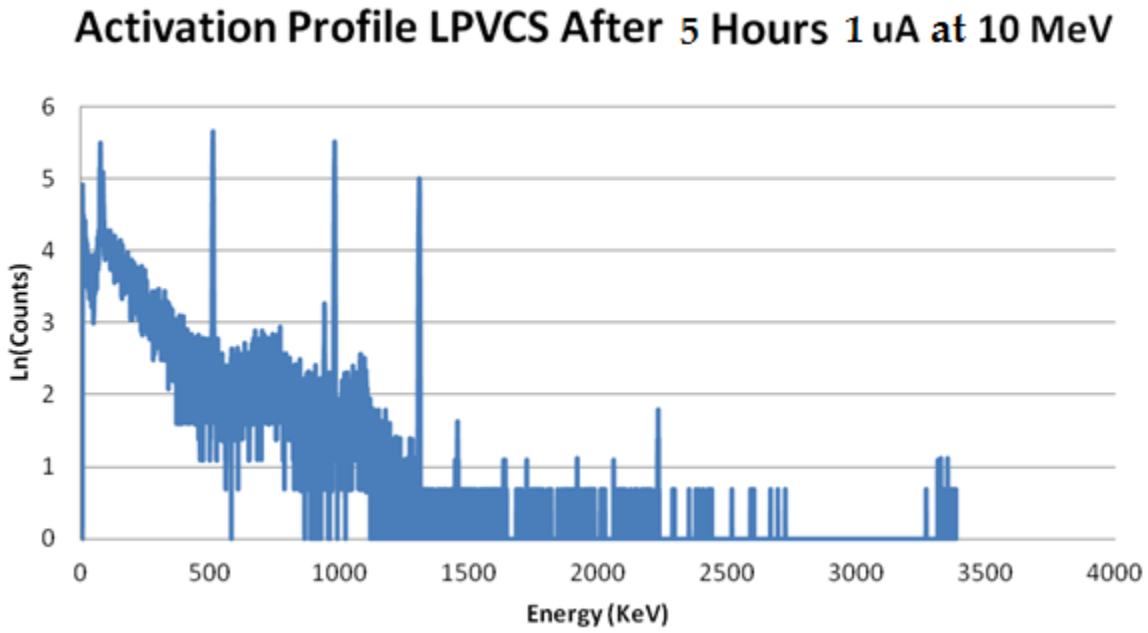

Figure 37
Gamma emissions from LPVCS sample after proton irradiation. The total average dose was 0.0007 dpa.

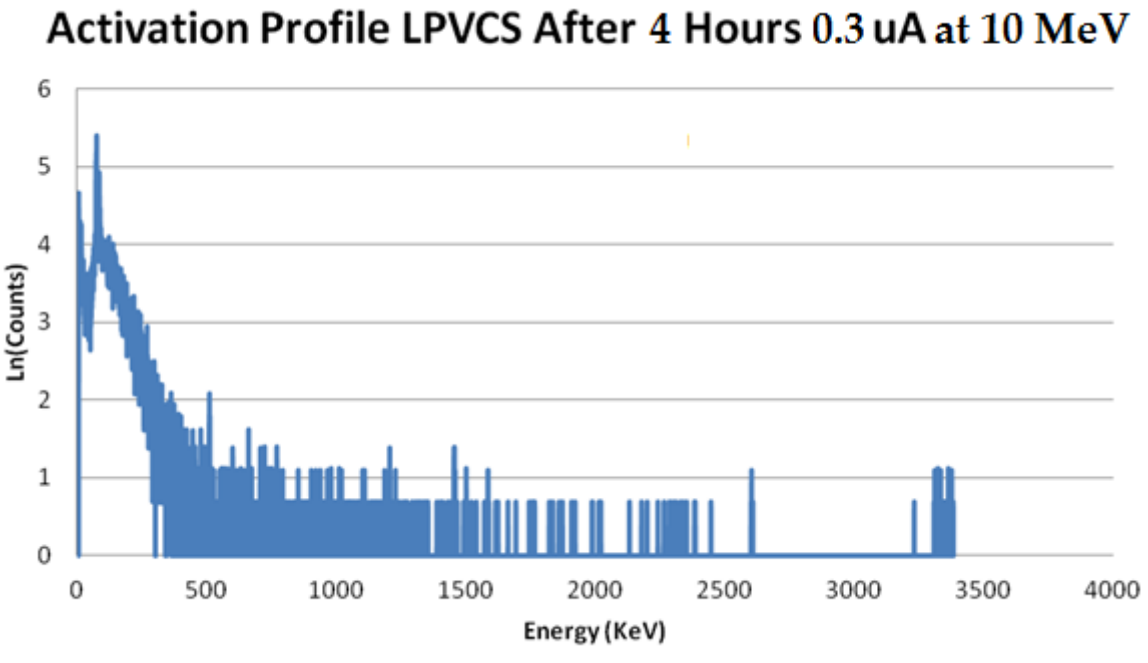

Figure 38
Gamma emissions from LPVCS sample after proton irradiation. The total average dose was 0.000021 dpa.

4.3. Mechanical Testing

4.3.1. Vickers Microhardness

Vickers indents were performed on the hot pressed α-SiC samples and pressureless sintered α-SiC, the indents were used for direct hardness measurements and crack measurement for fracture toughness. Extensive cracking on the sintered specimens was found to make this impractical with the equipment available and so results were only taken for the hot pressed α-SiC before and after irradiation as plotted in figure 39. The mean hardness measured for non-irradiated hot pressed α-SiC was 2970 HV0.1kgf whilst the mean hardness measured for air irradiated hot pressed α-SiC was 2900 HV0.1kgf. The sample standard deviations of these measurements were 360HV0.1kgf and 370HV0.1kgf, respectively. A Student T-Test (2-tailed) gave the likeliness of the null hypothesis being true (no change) at 30%. This is in part thought to be because of the imbalance of statistics used owing to the tendency for the air irradiated α-SiC to crack more readily (101 indents on non-irradiated, 43 on air irradiated). It is conjectured that this may be due to surface oxidation during air irradiation. Weibull fits were made using the method outlined in appendix D and the distributions plotted in figure 40. Here the similarity between their distributions suggests that no significant change can be detected.

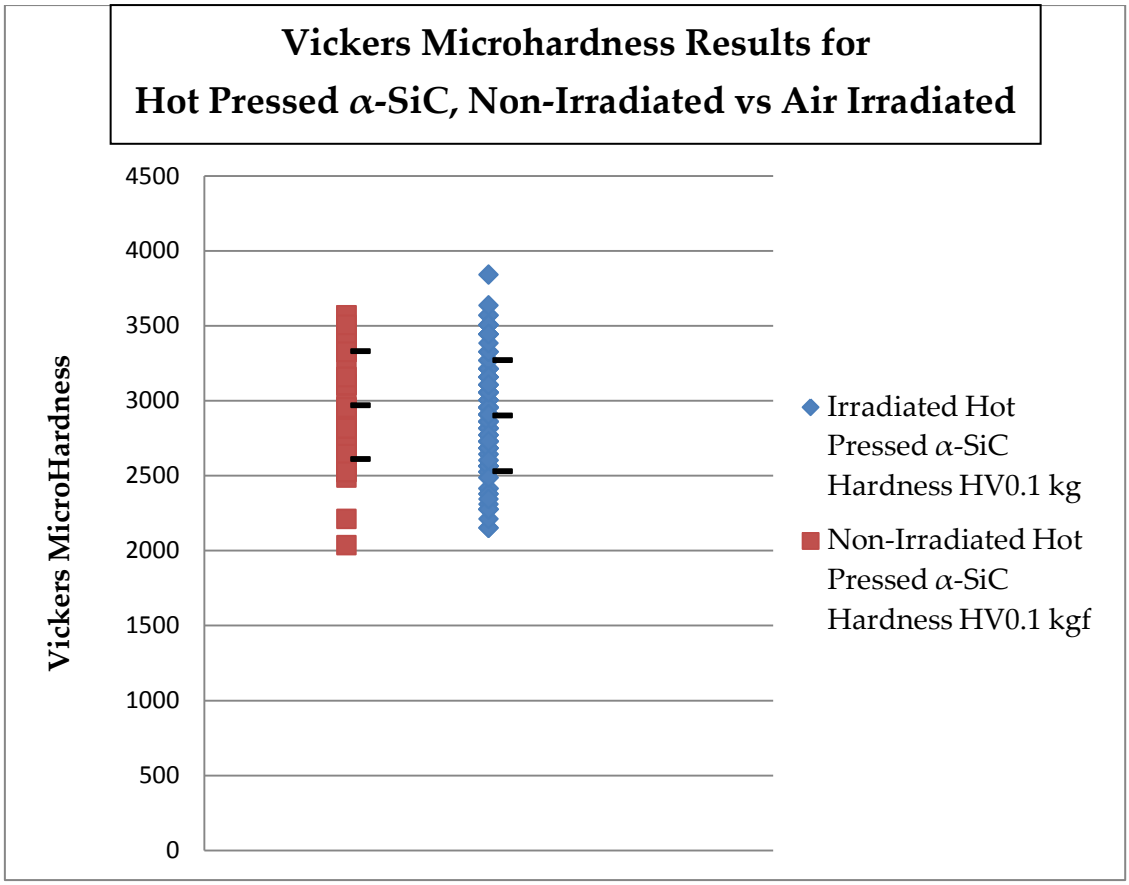

Figure 39
Vickers microhardness values taken from hot-pressed α-SiC before irradiation vs after irradiation. The standard deviation was prohibitively high so that any small change in Vickers hardness could not be separated from background noise.

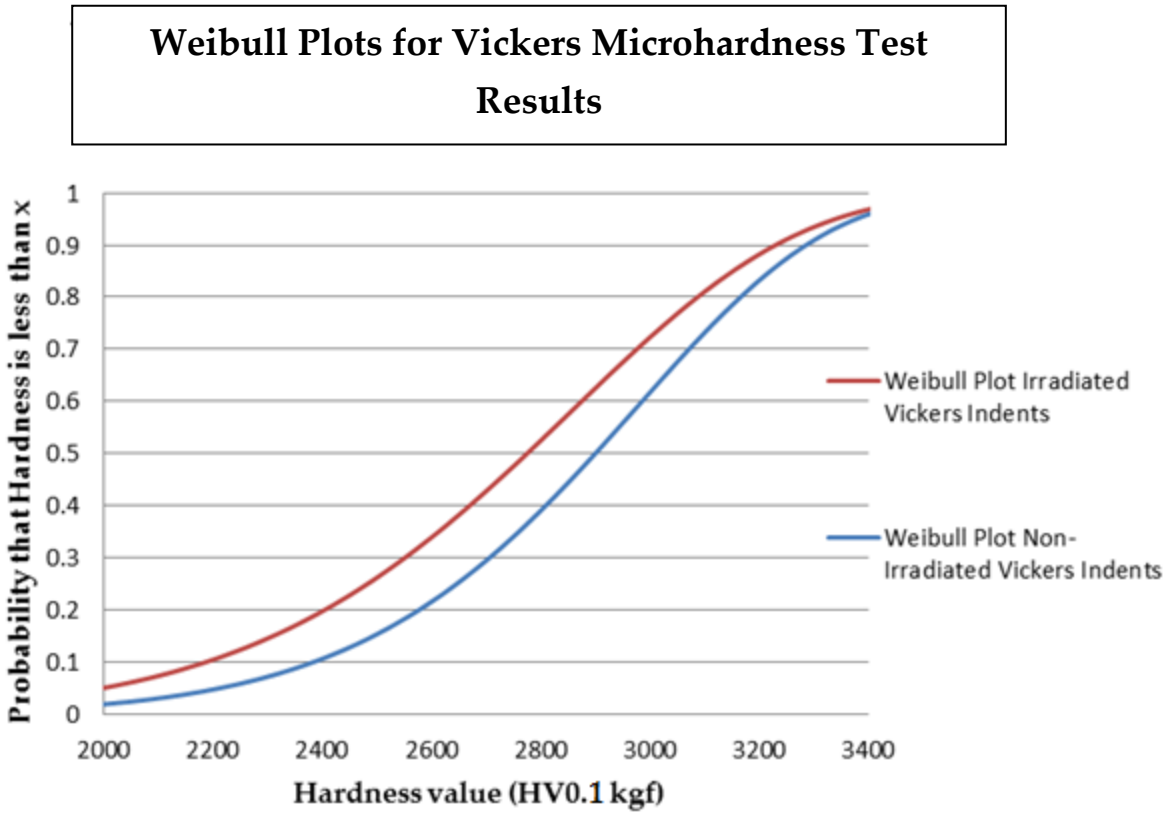

Figure 40
Plot of Weibull cumulative distribution functions using parameters found from non-irradiatedandair irradiated α-SiC data.

4.3.2. Nanohardness Tests

Nanoindentations were performed using the nanoindenter (as described in section 3.3.1.3.). Indentations were performed on the exposed fibre surfaces and matrix surface on the polished surfaces of the PCS and LPVCS composite materials used. As in appendix C, the nanohardness measurements did not differ more than 1 standard deviation between non-irradiated and irradiated samples suggesting a resistance to the irradiation conditions tested (0.00021 dpa, 0.3 μA for 4 hours at 85°C). Figure 41 is an example of the output generated by the nanohardness indenter, see appendix C for the tables summarising the data for each tested material.

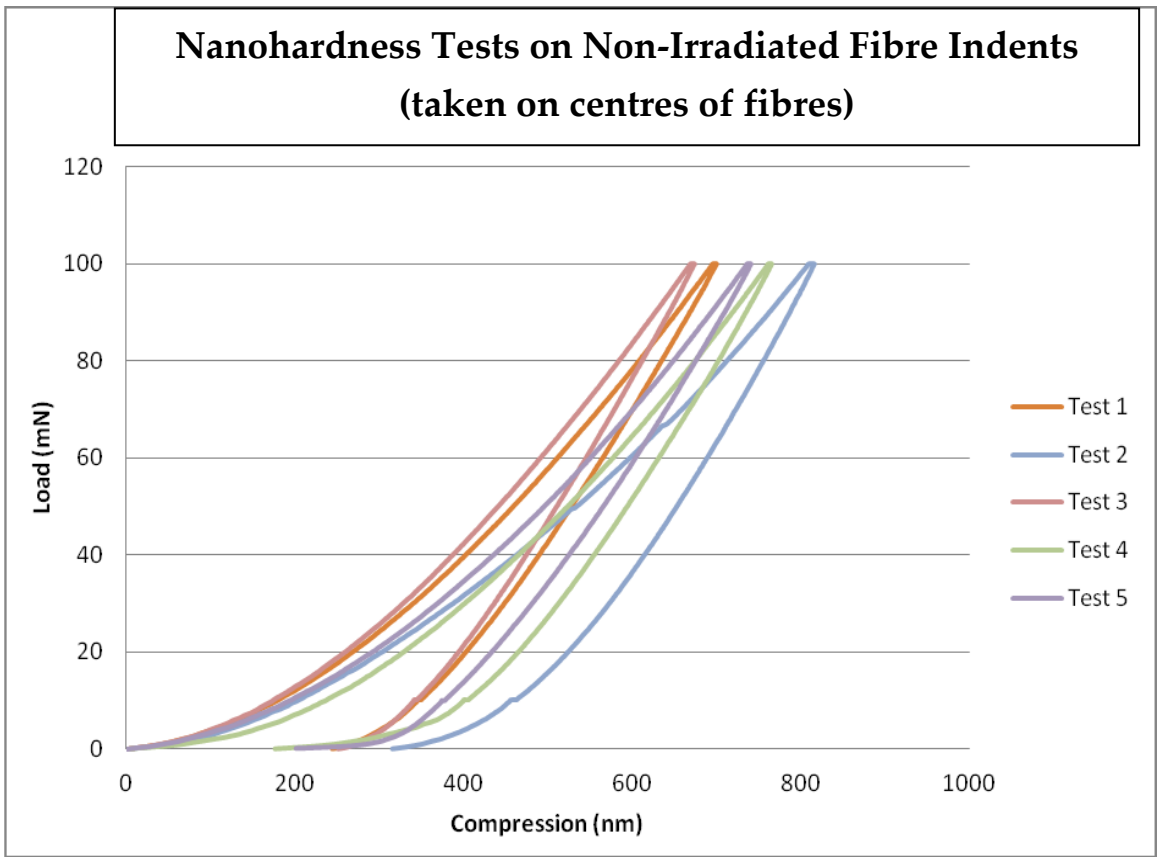

Figure 41
5 Nanohardness indentations were performed on the central regions of different fibres visible on the surface of a non-irradiated LPVCS sample polished to a 1 μm finish. The fibres chosen were around 50 μm apart.

4.3.3. Fracture Toughness from Vickers Indentation

By observing the crack length from Vickers indentations the fracture toughness was estimated in figure 42 (as described in section 3.3.1.1.). A high scatter was observed, but this method may be useful under different circumstances (especially because of the error in Vickers hardness measurements associated with cracking; this method may provide another means for comparison in that instance).

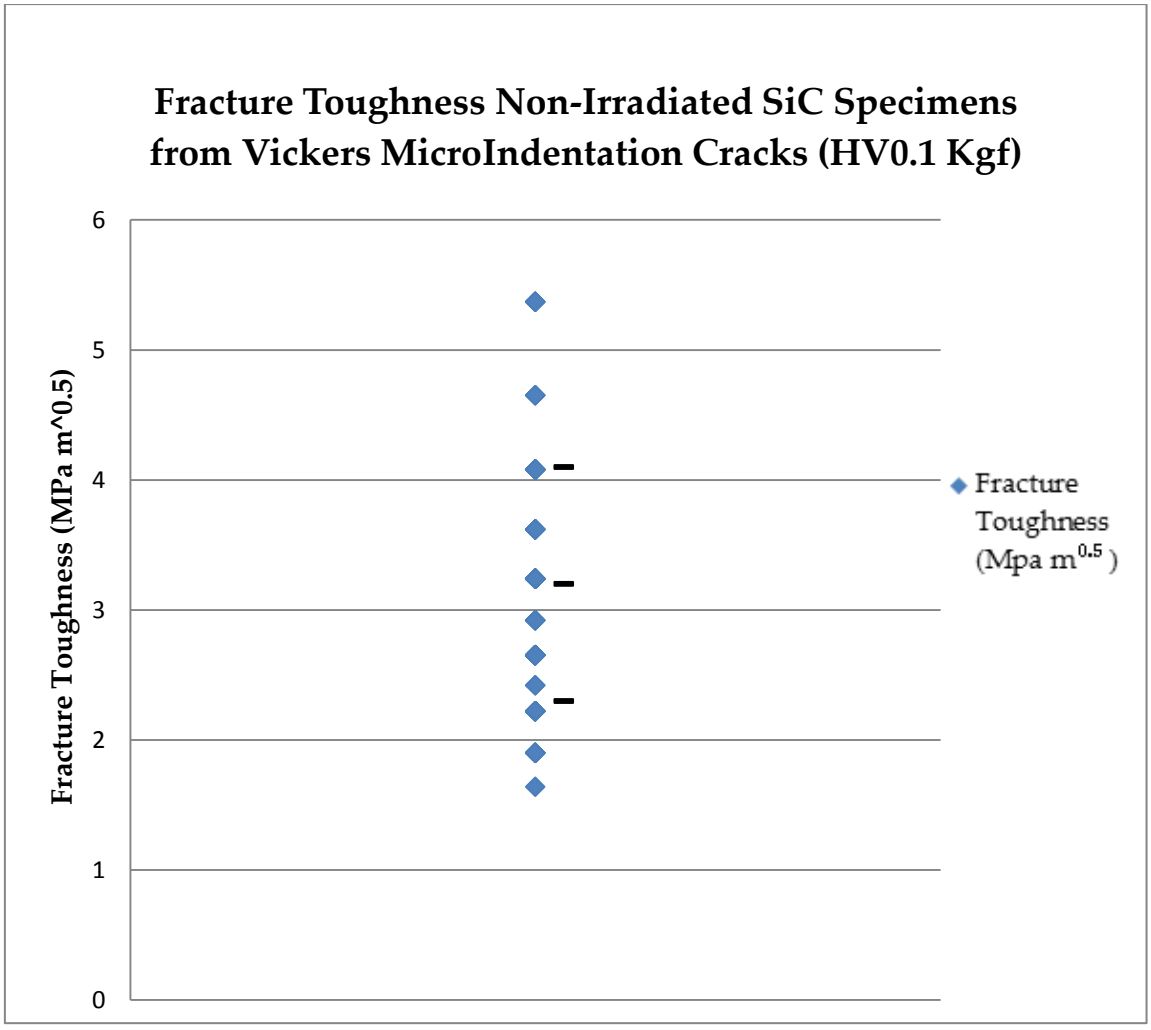

Figure 42
Fracture toughness results from crack length measurements around Vickers indents. The average fracture toughness was 3.3 MPa $m^{0.5}$ with a sample standard deviation of microhardness indents was 0.9 MPa $m^{0.5}$.

4.3.4. SCS-6 Fibre Tensile Testing

SCS-6 fibres were broken in tension as described in 3.4.1.5. After irradiation, the SCS-6 fibres tested were found to be very fragile and often broke during clamping for tensile testing. The tests performed are summarised in table 15. Unfortunately, due to the tendency of irradiated fibres to break during handling, it was difficult to obtain a large enough number of irradiated tests to produce a variation of statistical significance.

Table 15
Ultimate Tensile Strengths were obtained using an ESH machine.

Tensile Testing of SCS-6 Fibres			
	NonIrradiated (MPa)		**Irradiated (MPa)**
	3970		3500
	3170		3890
	4060		4310
	3620		4050
	3860		4140
	4020		3700
	3980		
	3610		
	3240		
	4080		
Average	3770		3930
Standard Dev.	310		306
Equivalent uncertainty	**+/- 8%**		**+/- 8%**

4.3.5. Thin Fibre (KD-1 and Nicalon) Tensile Testing

Thin fibre test results are plotted in figure 43. KD-1 fibres were tested after irradiation in vacuum (0.00021 dpa at estimated 85°C) and in air (0.0007 dpa at an estimated 400 °C), with an average beam current at 1 μA/cm² over 5 hours. These demonstrated an increase in mean strength of a factor of two. This was relatively unchanged by further irradiation for another 5 hours under the same conditions. Figure 44 shows a typical fracture surface from an air irradiated KD-1 fibre. A bundle of Nicalon fibre was also irradiated under the same conditions, however attempts at mechanically removing single Nicalon fibres from the bundle for tensile testing were unsuccessful.

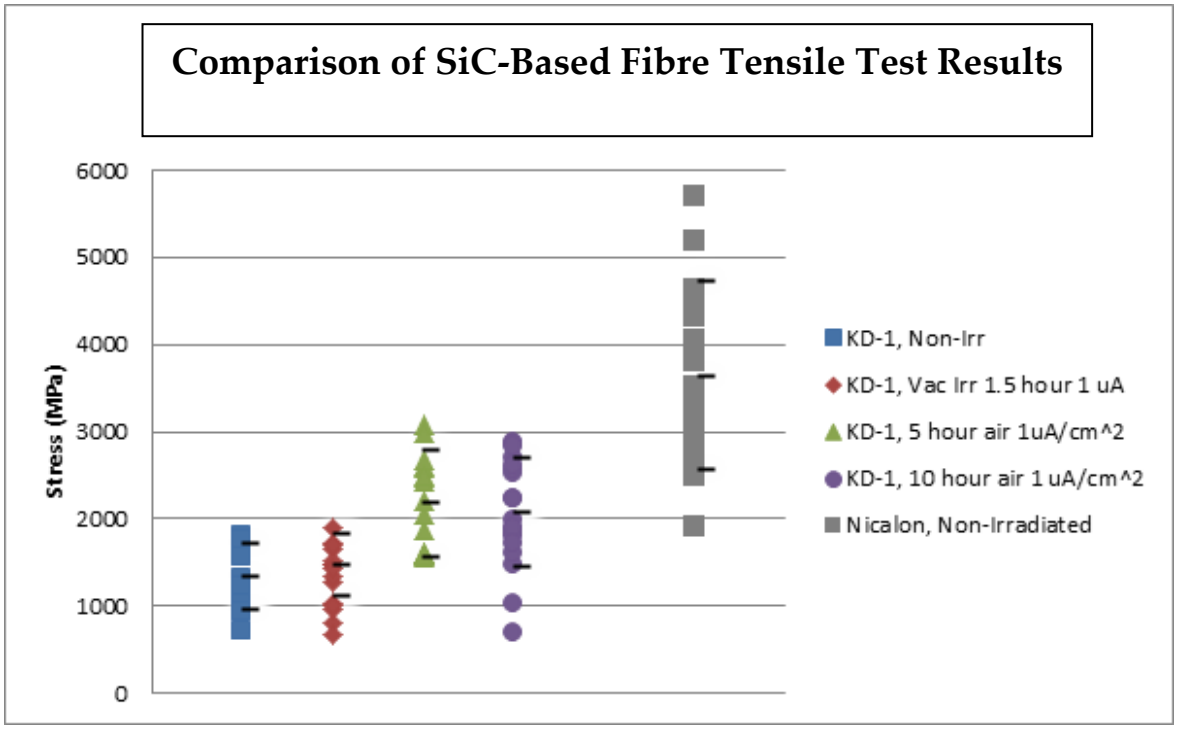

Figure 43
Thin fibre tensile test results – from left to right, KD-1 non-irradiated, KD-1 vacuum irradiated (0.00021 dpa over 4 hours at 0.3 μA), KD-1 air irradiated(0.0007 dpa over 5 hours 1μA), KD-1 air irradiated (0.0014 dpa over 10 hours at 1 μA), Nicalon non-irradiated (the irradiated Nicalon bundle merged so that individual fibres could not be removed).

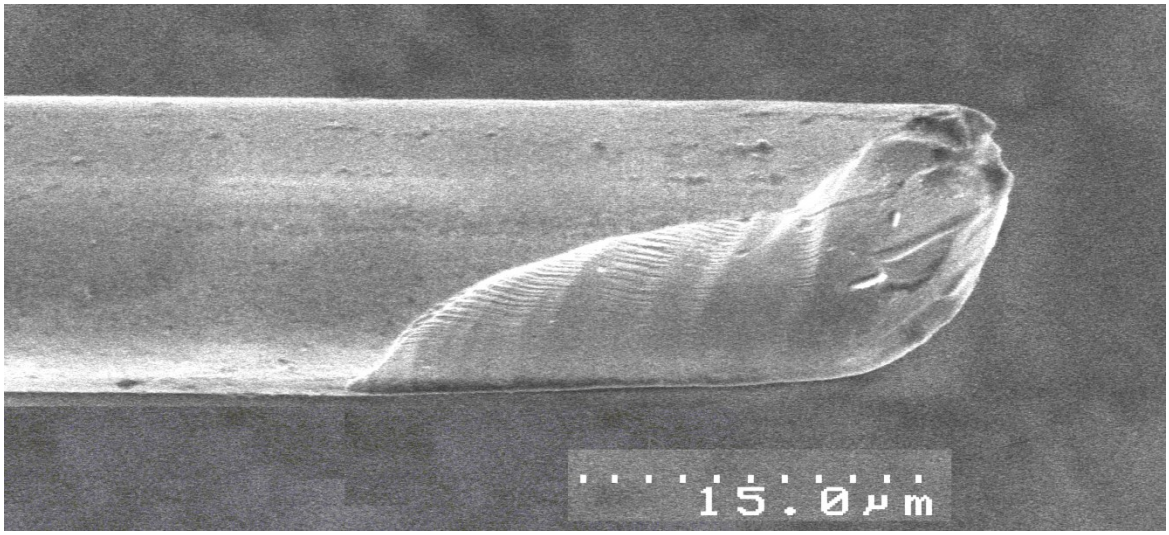

Figure 44
Air Irradiated KD-1 fractography image taken with SEM.

Work exists in the literature on the heat treatment of SiC/SiC composites manufactured by the CVI route with temperatures up to 1800 °C (i.e. Yang et al)(2007) [26] where no change in flexural properties was observed. These were heated in an inert atmosphere, so that oxidation may play a role at much lower temperatures. The conditions during air irradiation were estimated to be around 400 °C under irradiation.

Tensile testing of KD-1 fibres revealed changes due to irradiation. After vacuum irradiation, the mean tensile strength changes from 1340 MPa to 1480 MPa, which is 0.4 sample standard deviations. A Student T-Test comparing the non-irradiated and vacuum irradiated results using a 2-tailed distribution (a priori it was not known whether strength should increase or decrease) gave a probability of 46% that the null hypothesis (no significant change) is valid.

Weibull fits were made (using the method outlined in appendix E) for each thin fibre tensile data set and are plotted in figure 45. The non-irradiated and vacuum irradiated samples have a very similar distribution but the air irradiated distributions deviate significantly from the non-irradiated distribution. After air irradiation the tensile strength increased by roughly 2.3 standard deviations (of the non-irradiated distribution) from 1340 MPa to 2180 MPa.

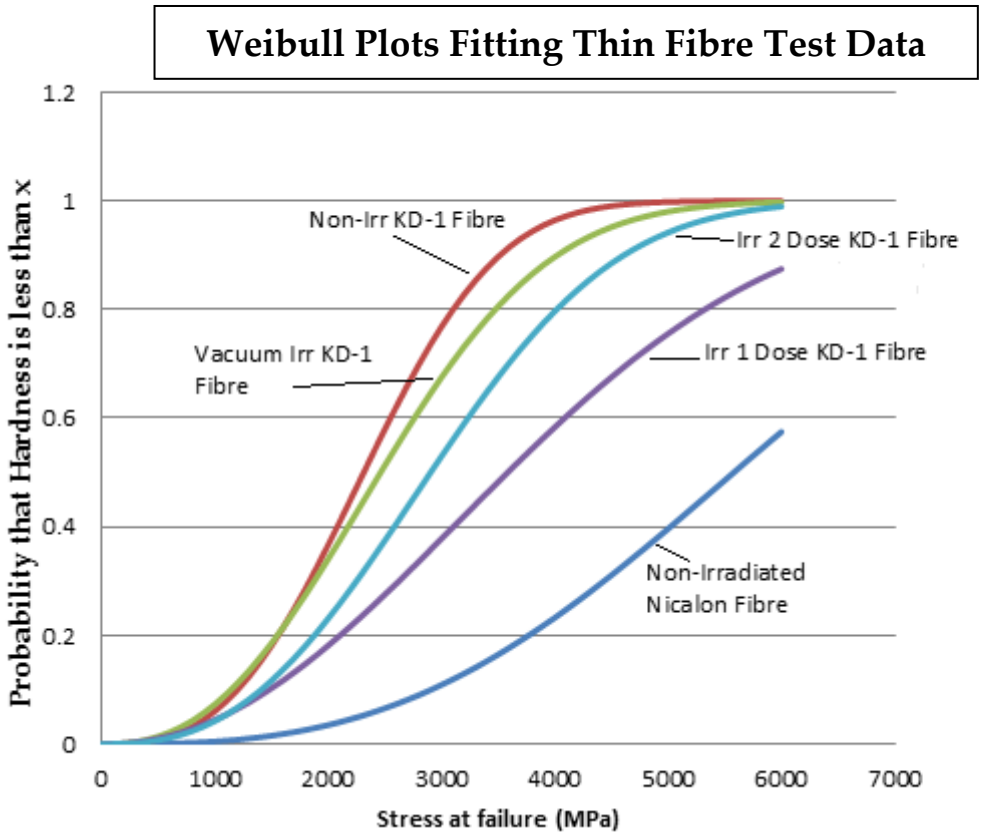

Figure 45
Plot of Weibull cumulative distribution functions using parameters found from thin fibre test data.

4.3.6. 4-Point Flexure

4.3.6.1. Flexure of Pressureless Sintered α-SiC

Flexure of pressureless sintered α-SiC samples in two groups (non-irradiated and irradiated in air with protons at 0.007 dpa) was performed using the setup described in section 3.1.4. Figure 46 compares stress/displacement results for air irradiated (a) and non-irradiated (b) specimens. The data obtained from these plots is displayed in tables 16 and 17. Spread in the surface energy at failure was observed to increase after irradiation (comparing table 16 (non-irradiated) with table 17 (irradiated)), with the standard deviations of stress at failure and stress energy stored as a fraction of measured values of these increasing by a factor of 3 and 5, respectively. However, the mean total stress energy and mean total stress at failure for both data groups have changed only within 1 standard deviation. The average extension before failure increased by 2 standard deviations from the non-irradiated samples after irradiation.

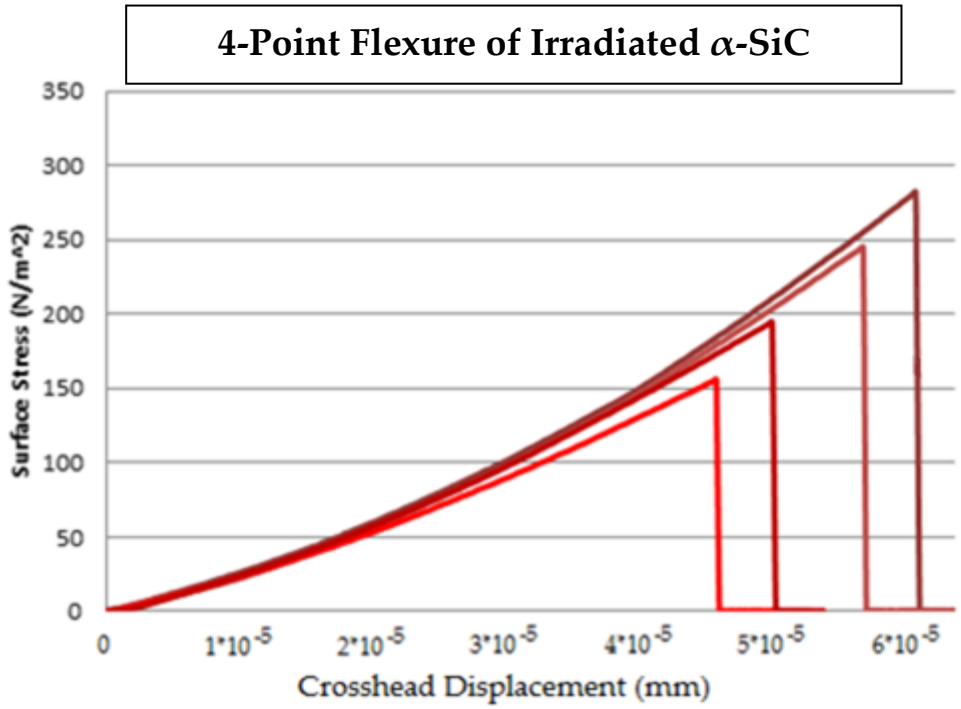

Figure 46(a)
Irradiated samples broken in 4-point bending show a greater variety of critical stresses, the average extension being slightly greater than for non-irradiated samples.

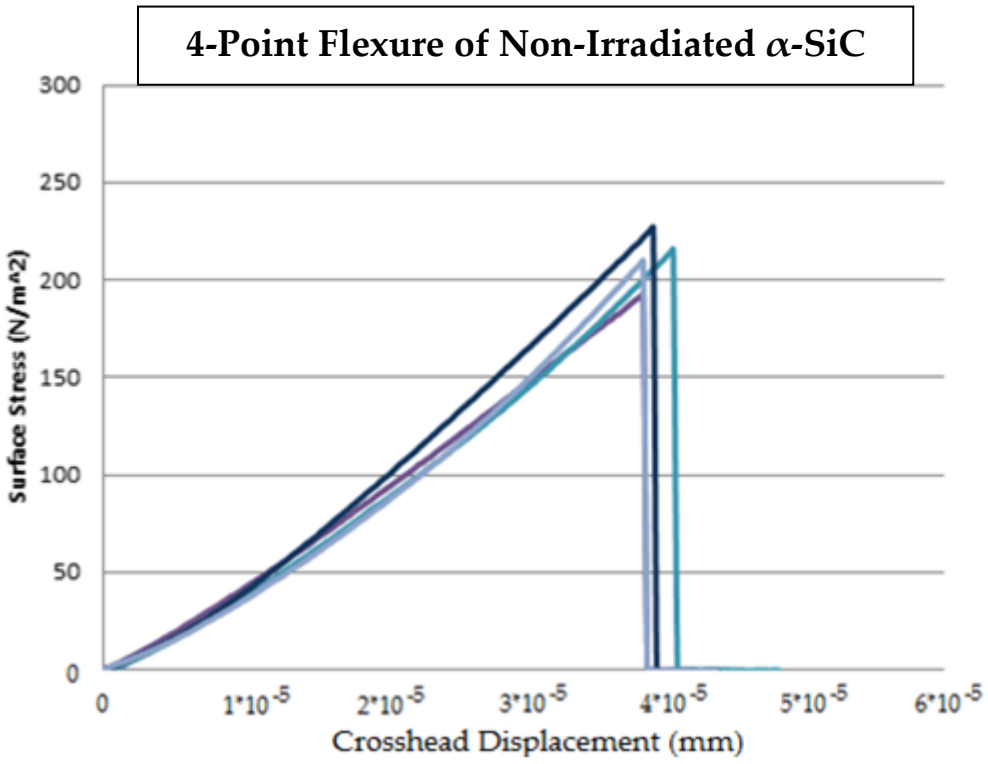

Figure 46(b)
Non-Irradiated α-SiC samples were tested to failure in 4-point flexure. The grouping of this data is much closer than for the irradiated α-SiC samples.

Table 16
Total surface energy at breaking (a), surface stress at failure (b) and extension before failure (c) were tabulated for each non-irradiated sample.

Failure Behaviour in 4-point Flexure of Non-irradiated Bulk Pressureless Sintered Carborundum α-SiC			
	Total Fracture Surface Energy in Non-Irradiated α-SiC (Jm-2)	**Total Stress at failure Non-Irradiated α-SiC** (MPa)	**Extension to Failure (m)**
Specimen 1	3.54	192	$3.85*10^{-5}$
Specimen 2	3.85	216	$4.07*10^{-5}$
Specimen 3	3.98	227	$3.92*10^{-5}$
Specimen 4	3.46	210	$3.85*10^{-5}$
Mean Work Done at Failure	**3.7**	**210**	**$3.9*10^{-5}$**
Sample Standard Deviation	**0.3**	**15**	**$1*10^{-6}$**
(Stan.Dev. / Mean) x100%	**+/- 6.8%**	**+/-7%**	**+/- 2.5%**

Table 17
Total surface energy at breaking (a), surface stress at failure (b) and extension before failure (c) were tabulated for each irradiated sample.

Failure Behaviour in 4-point Flexure of Irradiated Bulk Pressureless Sintered Carborundum a-SiC			
	Total Fracture Surface Energy in Irradiated α-SiC (Jm-2)	**Total Stress at failure in Irradiated α-SiC (MPa)**	**Extension to Failure in Irradiated α-SiC (m)**
Specimen 1	7.3	282	6.2*10-5
Specimen 2	5.9	245	5.8*10-5
Specimen 3	3.2	156	4.7*10-5
Specimen 4	4.3	195	5.1*10-5
Mean Work Done at Failure	5.2	220	5.5*10-5
Sample Standard Deviation	1.5	48	5.9*10-6
(Stan.Dev. /Mean)x100%	+/- 29%	+/- 22%	+/- 11%

4.3.6.2. Flexure of SiC Based Fibre Composites

4.3.6.2.1. Flexural Test Results

Flexure tests were performed on the PCS and LPVCS composite samples using the method outlined in section 3.3.1.4. Failure in these samples was characterised by an extended "plastic" region in which the fibres debonded from the sample matrix to form the crack surfaces observed (as can be seen in figures 52 (a) and (b)). The presence of relatively clean fibre shaped grooves in the crack surface (figure 52(a)) suggests the observed plastic behaviour is primarily due to fibre debonding and subsequent extension in the material. It is this slow failure that drastically increases the toughness of fibre reinforced ceramic composites compared to the sintered α-SiC tested (as in section 4.8.1.). Figures 49 (a) and (b) show the flexural stress vs crosshead displacement for LPVCS for non-irradiated and irradiated specimens and analogously for figures 50 (a) and (b) for PCS. The standard deviation of these flexure profiles is thought to be large enough as to make it very difficult to extract information about mechanical changes – within the accuracy of the experiment no change in flexural properties was detected after irradiation. All samples were vacuum irradiated to a dose of 0.00021 dpa at 85^{o}C. Typical observed behaviour at failure is depicted in figures 47 and 48. Figure 47 depicts a PCS sample with two breaks visible but neither crack occurred under the rollers. After the formation of one crack the specimen deflected preferentially towards one side to create the odd angle at which the second crack formed. This was found to occur more frequently in PCS samples than LPVCS. Samples which failed in this manner will have different behaviour in the "plastic" stress-displacement regime after initial fracture to samples with more central cracks (e.g. the LPVCS one in figure 48) which adds to the discrepancy between "plastic"

behaviour in the graphs of PCS stress vs crosshead displacement. Since the region between the rollers is in pure bending the stress at failure is still directly comparable to a specimen that fails directly at its centre such as figure 48.

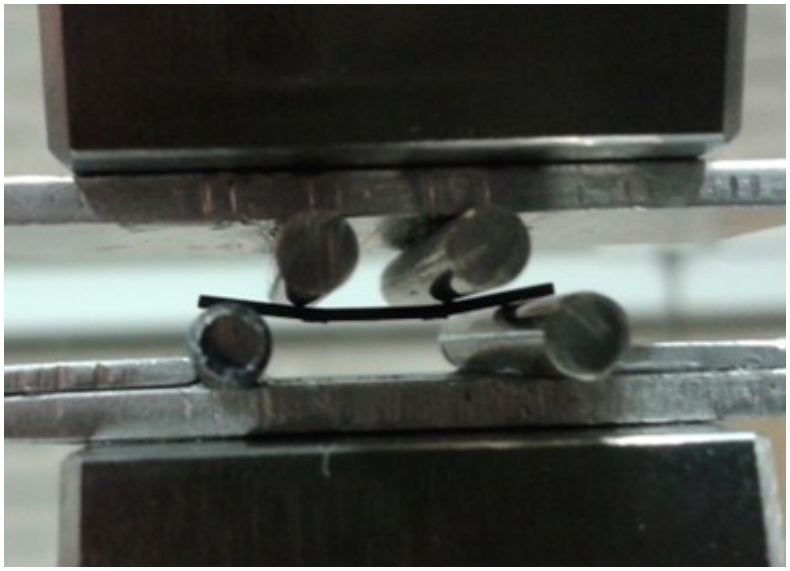

Figure 47
Typical flexure of thin PCS specimen. Neither crack occurred under the rollers, but after the formation of one crack the specimen deflected preferentially towards one side to create the odd angle at which the second crack formed.

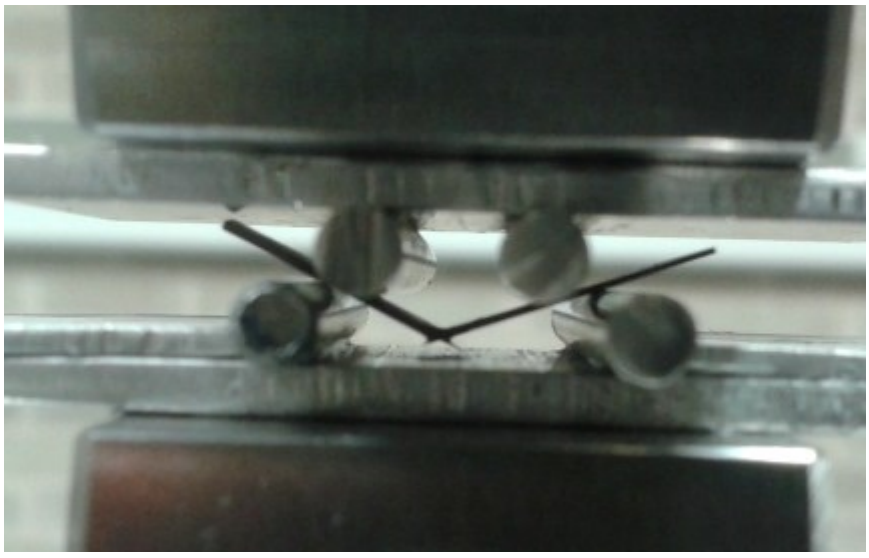

Figure 48
Typical flexure of thin LPVCS specimen. Extension was continued well into the plastic region; at the stage depicted here a reaction force was still detected which decreased in small jumps rather than abruptly as for monolithic SiC, suggesting an increase in toughness as is desired of fibre reinforced ceramic composites.

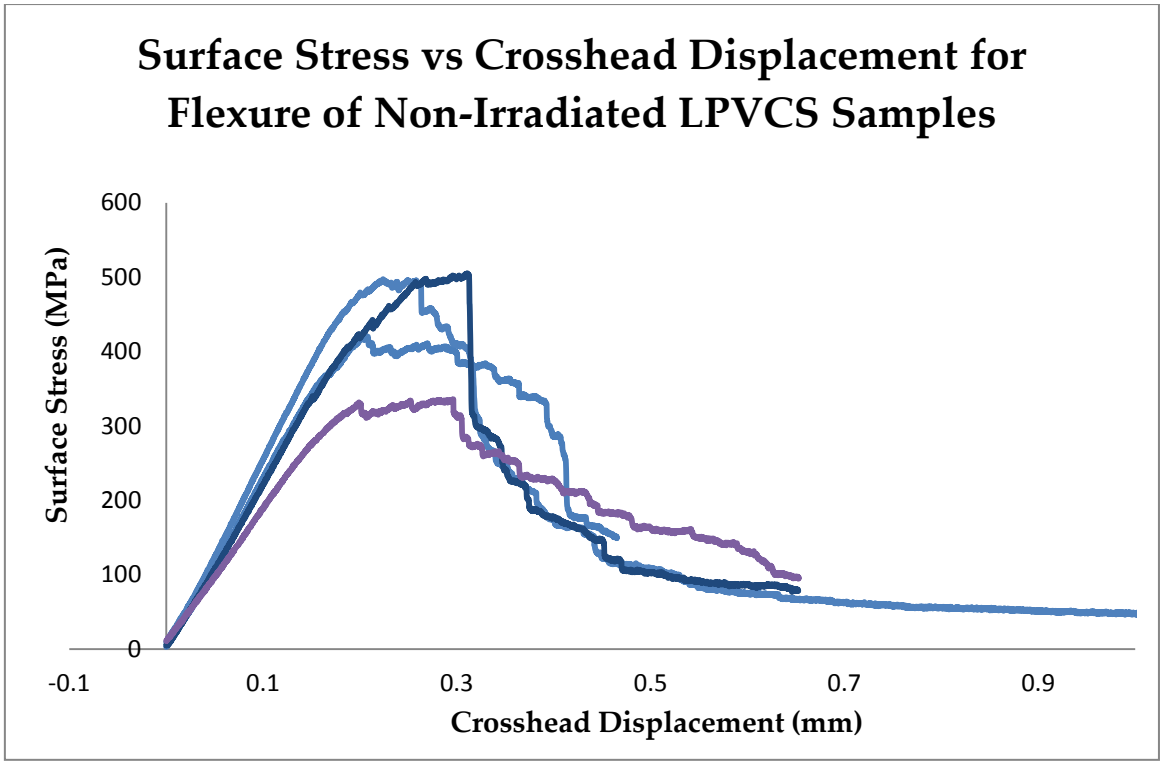

Figure 49 (a)
Flexure test results for non-irradiated LPVCS composite.

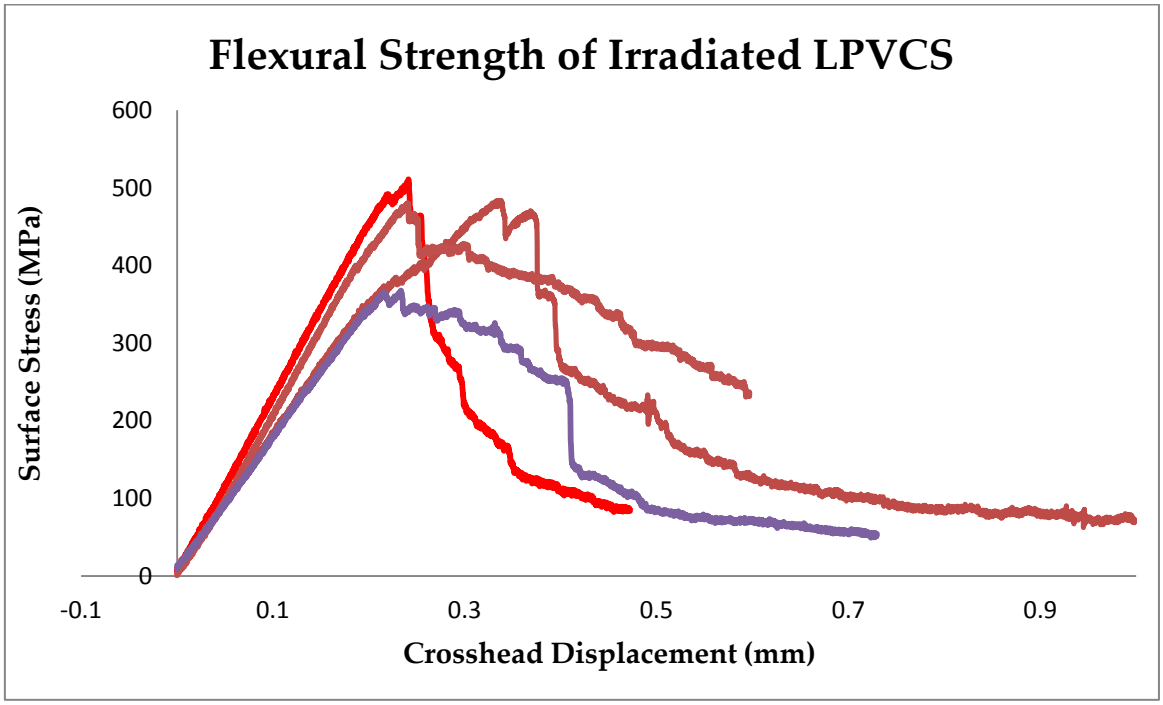

Figure 49 (b)
LPVCS samples irradiated in vacuum (2600 μC over 5 hours) for 0.00021 dpa damage at 85°C, The statistical spread is larger here but there appears to be a trend towards a more rapid loss of structural integrity after the critical flexure stress is reached.

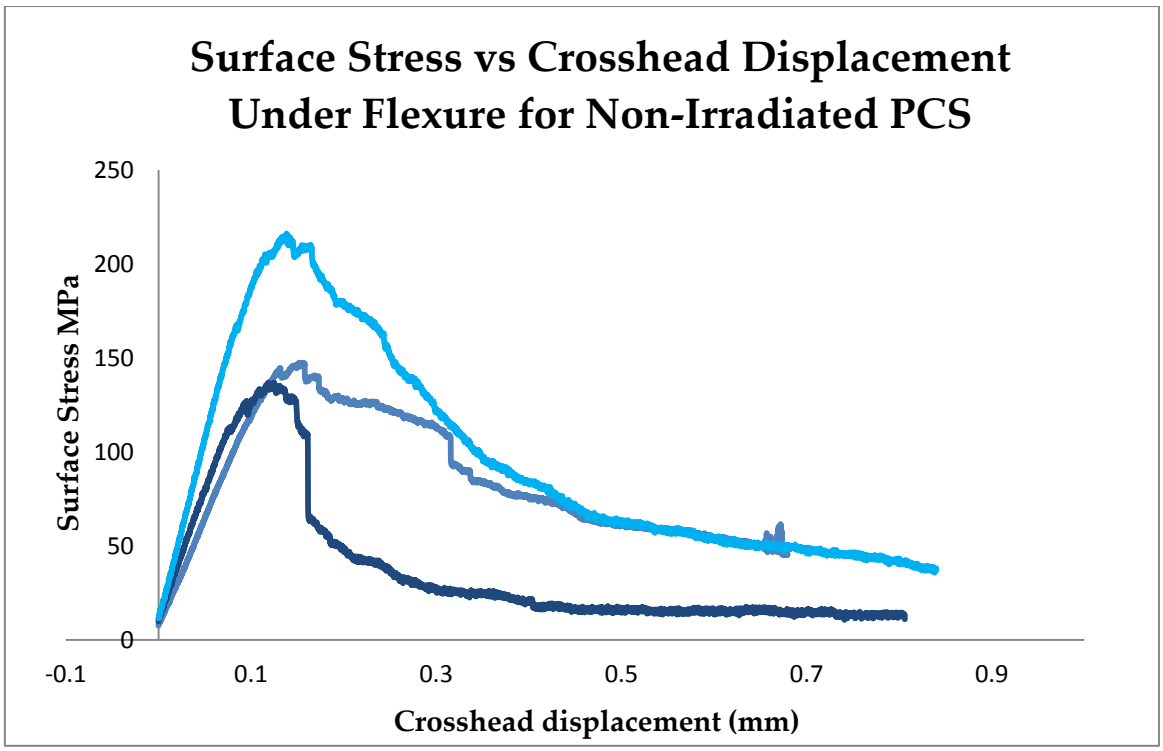

Figure 50(a)
Stress-displacement curve for non-irradiated PCS composite.

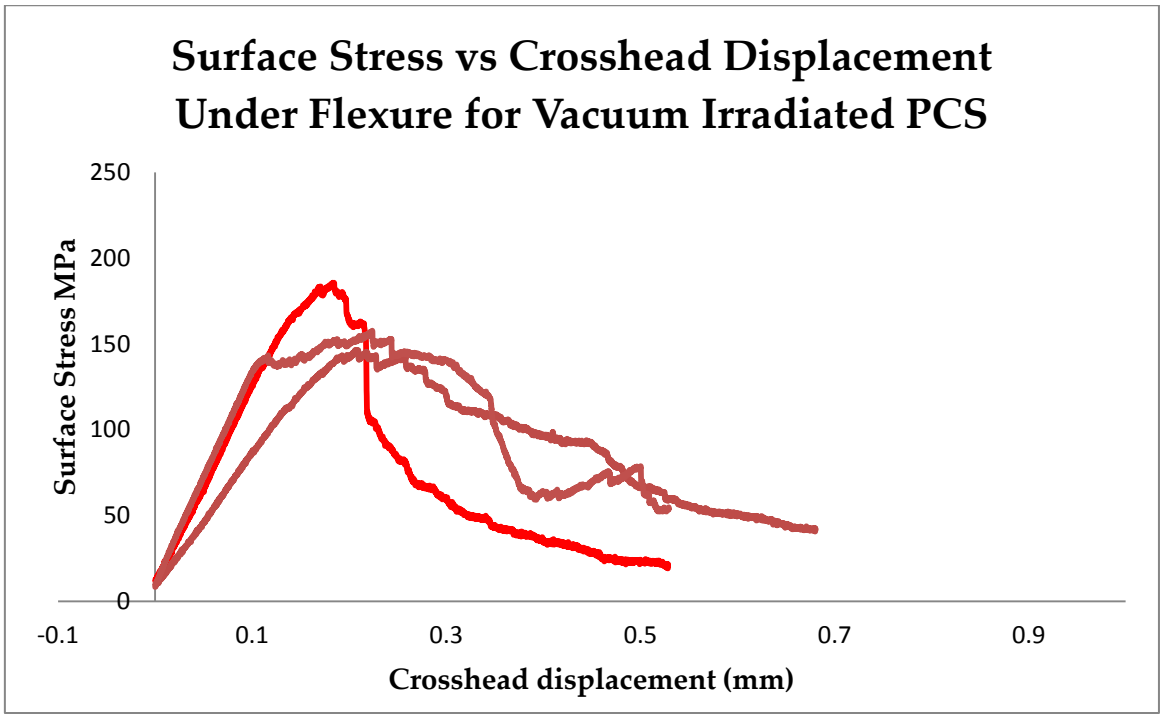

Figure 50 (b)
Stress-displacement curve for PCS composite irradiated in vacuum (2600 μC over 5 hours) for 0.00021 dpa damage at 85°C.

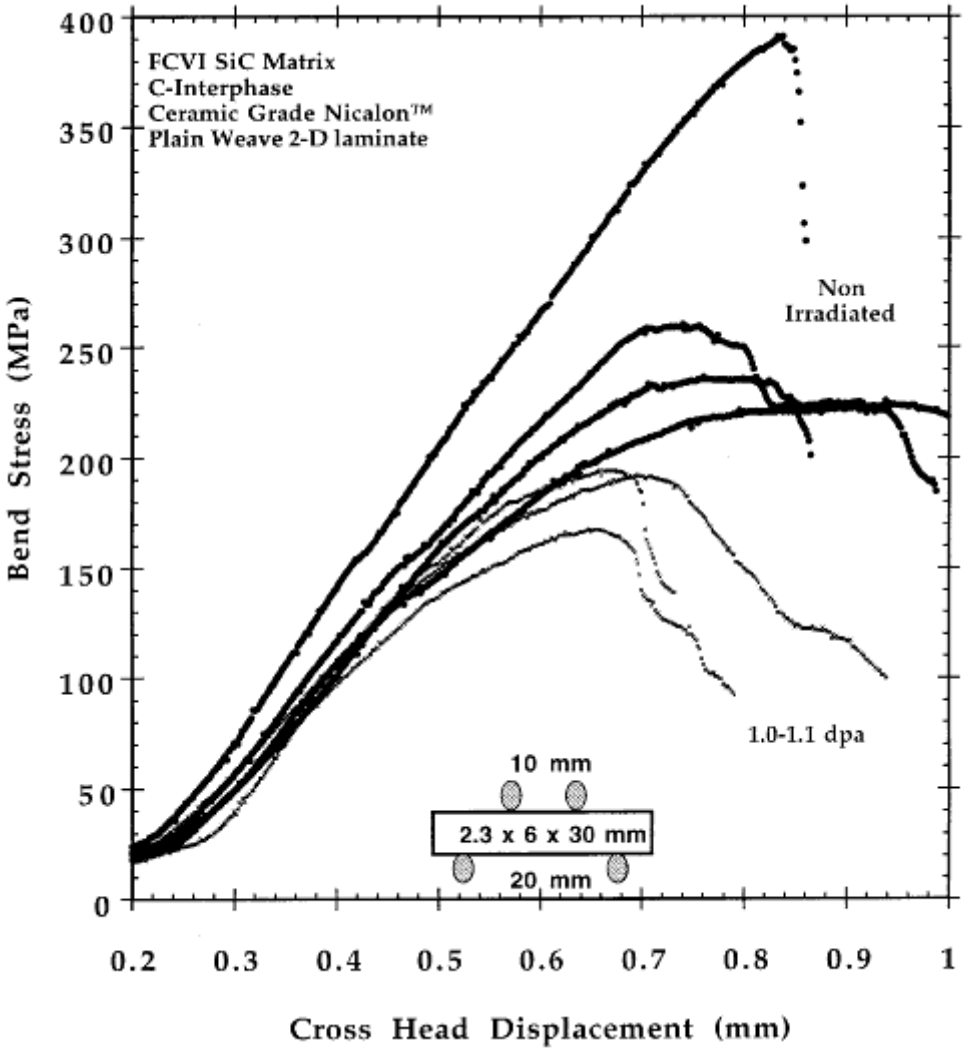

Figure 51
Graph taken directly from Snead et al[71], 1 dpa neutron irradiated near-stoichiometric nuclear grade SiC composite vs non-irradiated composite.

The standard deviation observed in the flexure tests is high but typical of SiC composites (compare figure 50(a) and (b) with figure 51, most notably after the ultimate stress is reached).

4.3.6.2.2. Fractography

Fractography was performed using SEM images of the surfaces after cracking in flexure, as in figures 52 (a) and (b). These images suggest that the primary failure process was fibre debonding as well as matrix cracking parallel to the fibres. It may be interpreted from the revealed crack surface in these images that matrix cracking becomes more important after irradiation (fewer fibres are visible in the crack surface of figure 52 (a) compared to (b)). Considerable discrepancy exists between fracture surfaces of different specimens tested under the same conditions so care must be taken in the interpretation of these SEM images.

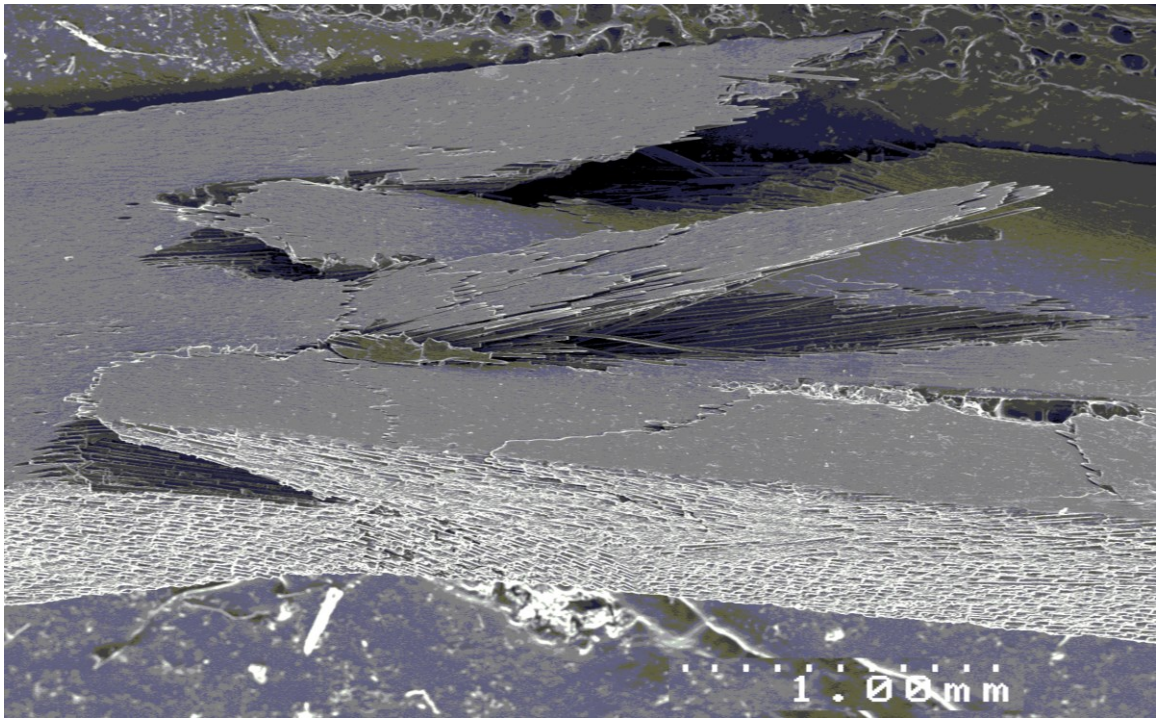

Figure 52(a)
Non-irradiated LPVCS fracture surface after 4-point bending, with limited damage visible on the matrix, indicating a low bonding between the KD-1 fibre and the matrix SiC.

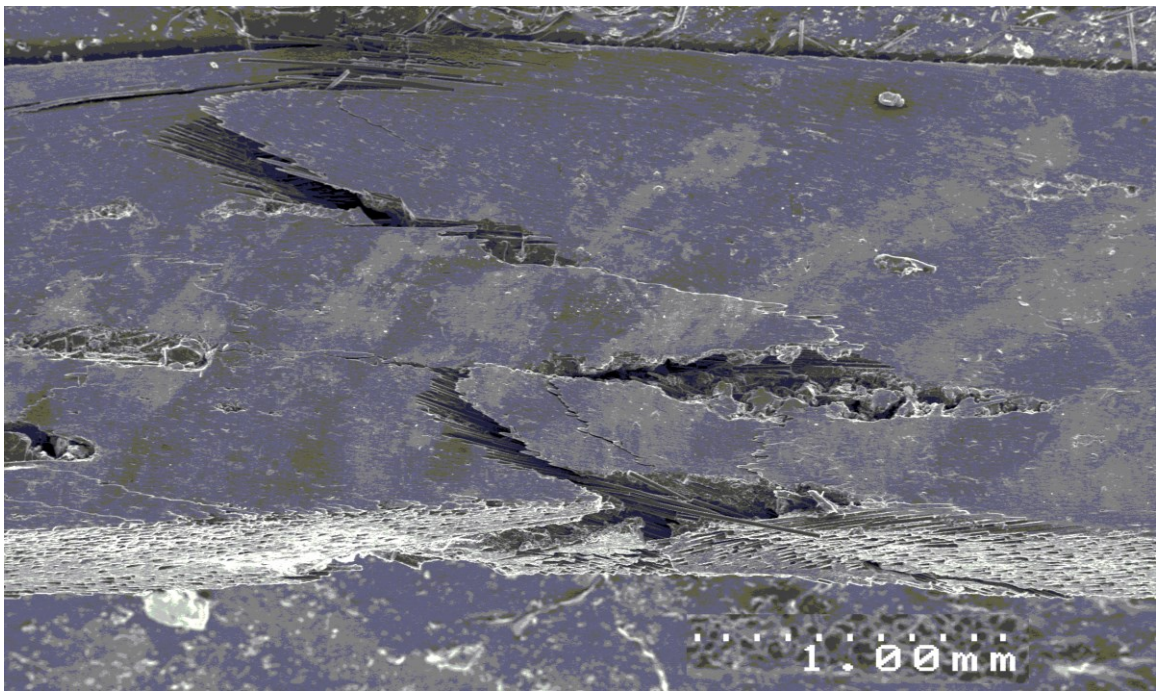

Figure 52(b)
Vacuum irradiated LPVCS (0.00006 dpa, 80°C) fracture surface after 4-point bending.

4.3.7. X-Ray Tomography of SiC Fibre Composites

X-Ray tomography was performed on PCS and LPVCS composite samples broken in flexure using a lab-based SkyScan 1172 X-ray MicroCT scanner with a tube-source Hamamatsu X-ray generator. The shape and relative distribution of their pores was extracted from the completed scans. Comparing figures 53 and 54, the internal structure of the PCS composites is very different – pores were only large enough to usefully identify in the PCS samples.

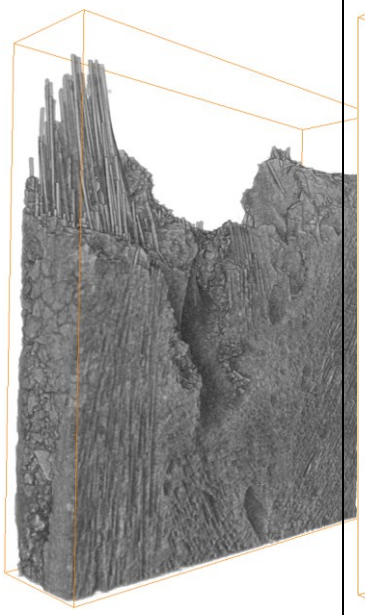	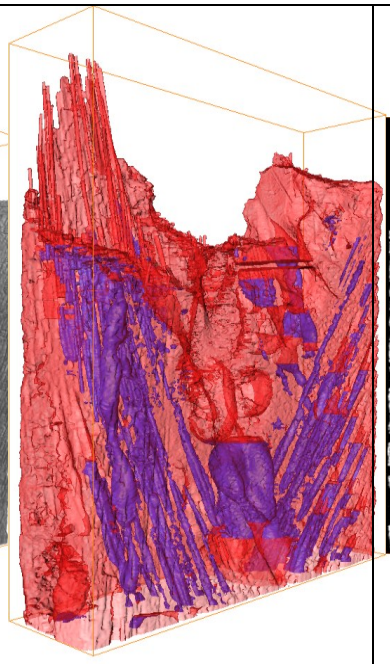	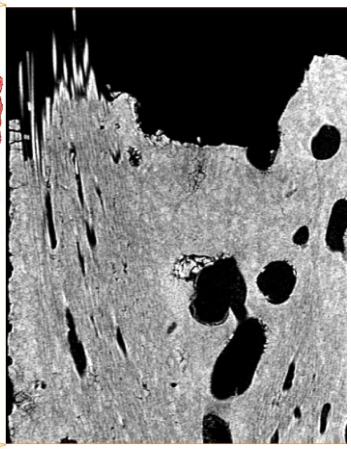
PCS Irradiated (Air) – Pre-segmentation visualisation	PCS Irradiated (Segmented) – Blue features are clusters of high pore concentration	Slice 215/270
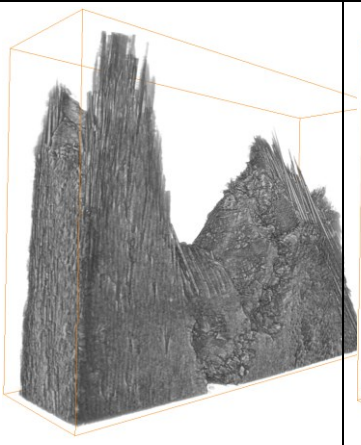	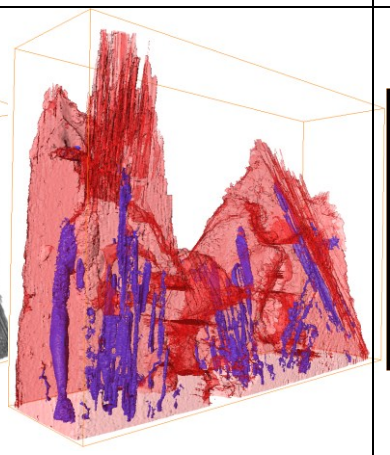	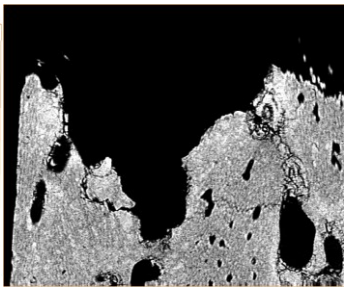
PCS Non-irradiated – Pre-segmentation visualisation	PCS Non-irradiated (Segmented) Blue features indicate internal pores not breaching the surface	Slice 367/499

Figure 53
Tomographic analysis of PCS composite non-irradiated vs irradiated.

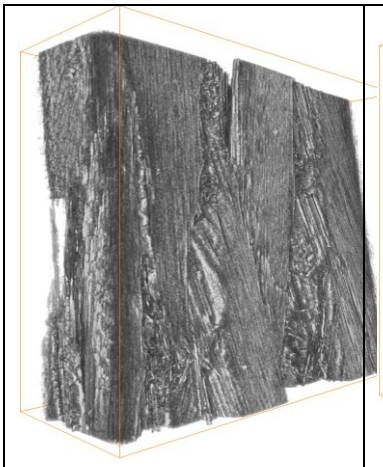		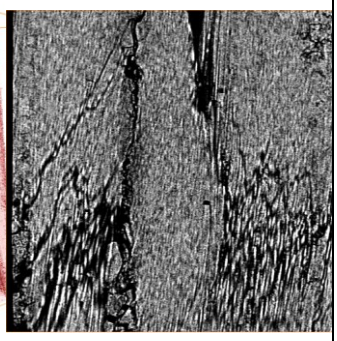
LPVCS Non-irradiated – Pre-segmentation visualisation	LPVCS Non-irradiated	Slice 272 of 544
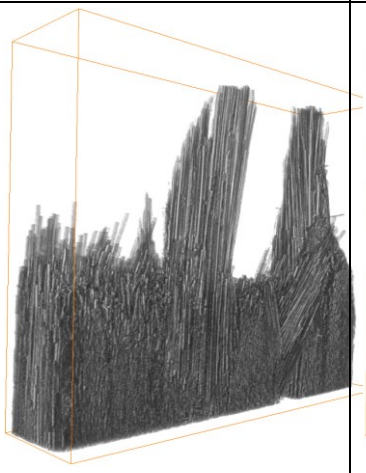	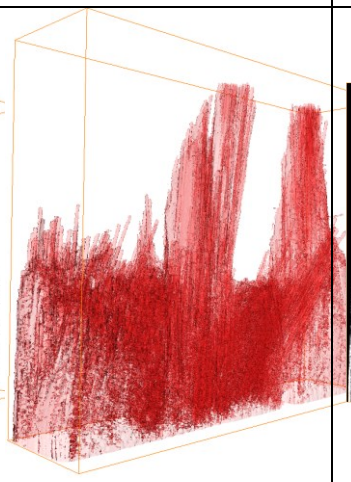	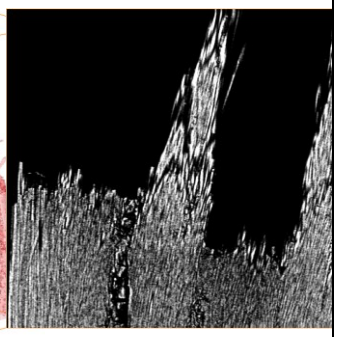
LPVCS Air Irradiated Pre-segmentation visualisation	LPVCS Air Irradiated	Slice 263/390

Figure 54
Tomographic analysis of LPVCS composite non-irradiated vs irradiated.

The irregular nature of the composites made it difficult to study the effects of these pores, since each composite piece is unique. Comparing relative pore sizes and distributions before and after irradiation, there is some evidence to suggest that a significant change may have taken place; in figure 55, the distribution of pore sizes for irradiated and non-irradiated samples shows that irradiated pores tended to be larger across a spectrum of sizes. In practice this may have been due to one being a fully broken specimen and the other partially broken in flexure.

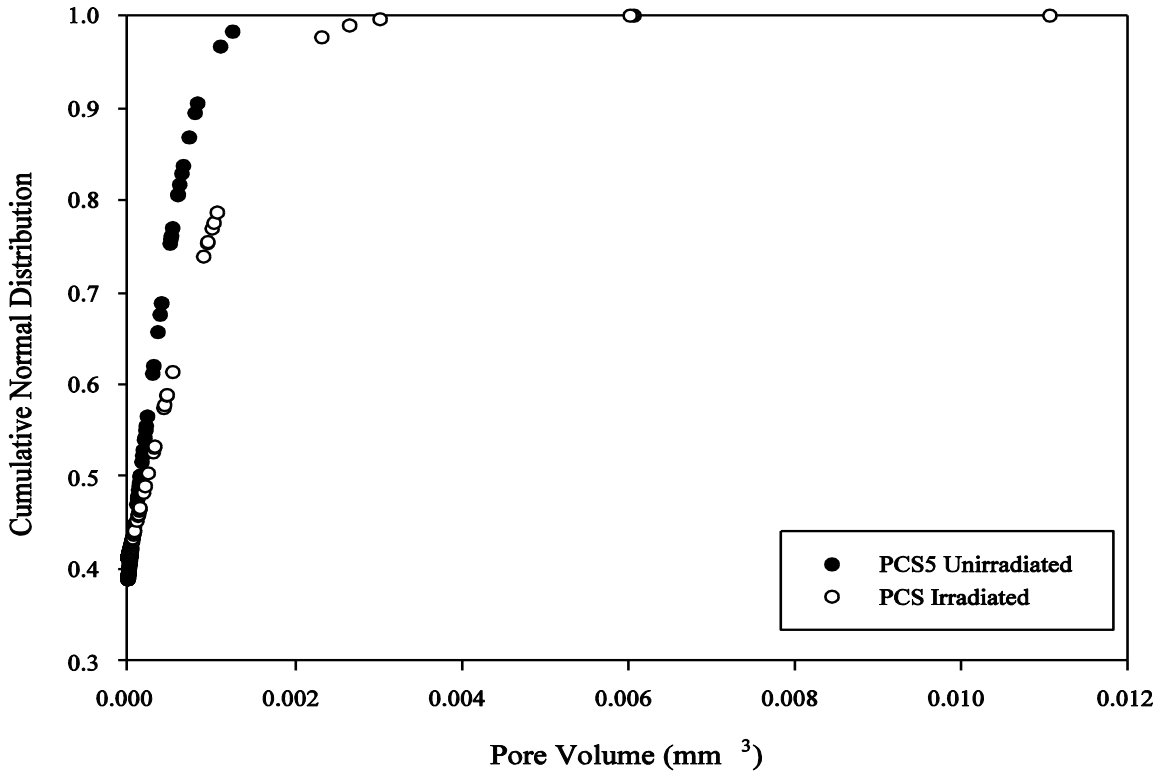

Figure 55
Comparison of porosity distribution, non-irradiated vs irradiated.

5. SUMMARY OF DISCUSSION

5.1. Establishment of Experimental Setup

A wide range of tests were conducted in this investigation. The experimental setup was demonstrated to be practical for holding samples during irradiation. Aluminium, the material which the water block was constructed from, tends to become Sodium 24 under proton irradiation at MeV-range energies (the rate of activation goes up as beam energy is increased up to maybe 20 MeVs). Whilst this is a mild β emitter, with a half-life of around 15 hours exposure can be easily controlled by leaving the water block for several days after irradiation. The primary drawbacks of the water block are an inability to measure temperature directly and that all irradiations must be done in atmosphere. Oxidation on the surface of irradiated materials may be the true cause of observed effects (further diagnostics could be performed, such as WDX on a surface before and after irradiation to spot differences in oxygen concentration).

A heat transfer model was constructed using a relaxation method which successfully incorporated a heat sink, varying internal heat source and geometry specific to the system.

Flexural tests were performed on α-SiC samples non-irradiated and irradiated. Significant differences in ultimate flexural strength were difficult to observe because of the size of the standard deviations of the data. Significant changes were found in the total extension before failure and in the standard deviation amongst the results, moving from around +/- 8% uncertainty in flexural strength to +/- 30%. Tensile tests showed little significant difference but this could be due to disparity in sample size.

5.2. Interpretation of Experimental Results

The composite materials used have a significant porosity. In the case of LPVCS, this manifests predominantly in the fibre bundles along the direction of the weave (parallel to fibre lengths). For PCS, by contrast, larger volumes of uninterrupted matrix material are present between fibre bundles. In these portions of matrix, pores are present that are much larger in volume than those found in LPVCS.

- Hot pressed α-SiC showed successful resistance to radiation; no significant hardnesss changes were observed after irradiation. The standard deviation in the results was high (as much as 50% of the mean hardness value), however, so that nanoindentation for this material may be more appropriate than microindentation in future.
- KD-1 fibres exhibited a significant (2 standard deviations) increase in tensile strength after air irradiation at 0.007 dpa and 400 ^{o}C. After treatment in a furnace at 400 ^{o}C, this increase was not observed and so may be attributable to radiation induced changes.
- Sintered α-SiC samples displayed an increase in standard deviation of stress at fracture and surface energy at fracture, though the mean values for these properties were not significantly different between non-irradiated and irradiated specimens, suggesting surface changes more likely due to oxidation than radiation damage.
- SCS-6 showed no significant change in tensile properties to the accuracy of the apparatus after irradiation but exhibited less resistance to stresses applied during handling (bending).

- PCS composites showed no significant degradation of nanohardness after air irradiation. They also
- LPVCS composites showed no significant degradation of nanohardness after air irradiation.

6. CONCLUSIONS

The original intention, to use light ions at high energy to cause radiation damage through a thickness on the order of 1mm of SiC fibre composite, was found to be prohibitively difficult with the setup developed for this project. The setup itself demonstrated the capability of sample irradiation using hydrogen ions or alpha particles in atmosphere or medium vacuum (a pressure of less than 10^{-9} Pa). The facility could irradiate a range of rectangular profiles by changing the aperture spacing (so long as their dimensions are not greater than 2 cm by 1 cm). Dose profiles were calculated for several key beam energies that can be produced by the MC-40 cyclotron using the TRIM program. Temperature during operation was modelled using a finite difference scheme and then the computational modelling program COMSOL for a flat specimen clamped to the beam target behaviour under irradiation can be strongly temperature dependant [24, 25, 30-35]. Temperature adjacent to but not directly in contact with the irradiated sample was measured using an n-type thermocouple (unfortunately, direct contact with the sample could allow ion beam onto the thermocouple, contaminating the reading) at intervals of 1 minute over several full irradiation runs.

Mechanical testing together with characterisation using a variety of methods was successfully performed on SiC based materials, including bulk α-SiC, SiC composite and SiC fibres. Radiation damage and particle stopping distances were generated using the TRIM and SRIM software so that damage profiles could be designed for specific experiments. A computational model was developed using a numerical model based on a relaxation scheme to predict the temperature of a tested sample during irradiation.

A facility for the irradiation of material samples in vacuum was developed with temperature control mechanisms (a heating element for the samples during testing) and beam collimator to control the area profile of the target that is exposed to the ion beam.

Whilst causing radiation damage to SiC at doses relevant for nuclear applications was found to be prohibitively difficult with the ion source available, the potential for irradiating materials composed of heavier elements such as steels (which should be damaged more easily and also require more penetrating radiations than light elements) exists (after e.g. Nagawaka et al [68].

7. FURTHER WORK

There is scope for investigation of higher dose effects on the materials tested using helium ions instead of hydrogen, though higher heat loading made this impractical with the current setup, running for extended periods at low doses may provide higher surface damage.

Higher dose effects on the materials tested could also be attained using an alternative radiation source. With the lower energy but higher ion flux of an electrostatic accelerator, higher doses over a shallower depth could be attained which would provide a greater range of doses for nanohardness tests. Using such a setup, a higher dose for the thin fibres (KD-1 and Nicalon) could also be attained and further tensile testing performed.

8. REFERENCES

1. L.L. Snead, R.H. Jones, A. Kohyama, P. Fenici, "**Status of silicon carbide composites for fusion**", Journal of Nuclear Materials (I 996), Volumes 233-237, pp 26-36

2. P. Fenici, A.J. Frias Rebelo, R.H. Jones, A. Kohyama, L.L. Snead, "**Current status of SiC/SiC composites R&D**", Journal of Nuclear Materials (1998), Volumes 258-263, pp 215-225

3. R.H. Jones, L.L. Snead, A. Kohyama, P. Fenici, "**Recent advances in the development of SiC:SiC as a fusion structural material**", Fusion Engineering and Design (September 1998), Volume 41, Issues 1–4, pp 15–24

4. Hasegawa, A. Kohyama, R.H. Jones, L.L. Snead, B. Riccardi, P. Fenici, "**Critical issues and current status of SiC/SiC composites for fusion**", Journal of Nuclear Materials (2000), Volumes 283-287, pp 128-137

5. A.R. Raffray, R. Jones, G. Aiello, M. Billone, L. Giancarli,H. Golfier, A. Hasegawa, Y. Katoh, A. Kohyama, S. Nishio,B. Riccardi, M.S. Tillack, "**Design and material issues for high performance SiCf/SiC-based fusion power cores**", Fusion Engineering and Design (2001), Volume 55, pp 55–95

6. R.H. Jones, L. Giancarli, A. Hasegawa, Y. Katoh, A. Kohyama, B. Riccardi, L.L. Snead, W.J. Weber, "**Promise and challenges of SiCf/SiC composites for fusion energy applications**", Journal of Nuclear Materials (2002), Volume 307–311, pp 1057–1072

7. B. Riccardi, L. Giancarli, A. Hasegawa, Y. Katoh, A. Kohyama, R.H Jones, L.L Snead, "**Issues and advances in SiC$_f$/SiC composites development for fusion reactors"** Journal of Nuclear Materials (August 2004), Volumes 329–333, Part A, pp 56–65

8. Y. Katoh**,** L.L. Snead, T. Nozawa, N.B. Morley, W.E. Windes, "**Advanced Radiation-Resistant Ceramic Composites",** Advances in Science and Technology (2006), Volume 45, pp 1915-1924

9. Y. Katoh, L.L. Snead, C.H. Henager Jr., A. Hasegawa, A. Kohyama, B. Riccardi, H. Hegeman, "**Current status and critical issues for development of SiC composites for fusion applications**", Journal of Nuclear Materials (2007), Volumes 367–370, pp 659–671

10. L. L. Snead, T. Nozawa, Y. Katoh, B. Thak-Sang, S. Kondo, D.A. Petti, "**Handbook of SiC properties for fuel performance modelling**", Journal of Nuclear Materials (2007) , Volume 371, pp 329–377

11. "**Workshop on Science Applications of a Triple Beam Capability for Advanced Nuclear Energy Materials**", Co-Chairs M. Fluss and W.E. King, (April 6-7 2009), held at Lawrence Livermore National Laboratory

12. G. Aiello, A. Gasse, L. Giancarli, H. Golfier, J.F. Salavy, J. Szczepanski, "**The TAURO SiC/SiC breeding Blanket**", presentation made as part of EURATOM (European Atomic Energy Community), available at ARIES program website http://aries.ucsd.edu/LIB/MEETINGS/0001-SiCSiC/Golfier.pdf (accessed 20/11/2013)

13. K. Abe, A. Kohyama, S. Tanaka, C. Namba, T. Terai, T. Kunugi, T. Muroga, A. Hasegawa, A. Sagara, S. Berk, S.J. Zinkle, D.K. Sze, D.A. Petti, M.A. Abdou, N.B. Morley, R.J. Kurtz, L.L. Snead, N.M. Ghoniem, "**Development of advanced blanket performance under irradiation and system integration through JUPITER-II project**", Fusion Engineering and Design (October 2008), Issue 83, pp 842–849

14. S. Bragg-Sitton, K. Barrett, I. van Rooyen, D. Hurley, M. Khafizov, "**Studying silicon carbide for nuclear fuel cladding**", Nuclear Engineering International (May 2013), Volume 58, Issue 706, pp 37-40

15. C.P. Deck, H.E. Khalifa, B. Sammuli, T. Hilsabeck, C.A. Back, "**Fabrication of SiC-SiC Composites for Fuel Cladding in Advanced Reactor Designs**", Progress in Nuclear Energy (2012), Volume 57, pp 38-45

16. Y. Katoh, L. L. Snead, I. Szlufarska, W. Weber, "**Radiation Effects in SiC for Nuclear Structural Applications**", Current Opinion in Solid State and Materials Science (2012), Volume 16, pp 143-152

17. V. Barabash, G. Federici, M. Rödig, L.L. Snead, C.H. Wu, "**Neutron irradiation effects on plasma facing materials**", Journal of Nuclear Materials (2000) , Volumes 283-287, pp 138-146

18. A.R. Bunsell, A. Piant, "**A review of the development of three generations of small diameter silicon carbide fibres**", Journal of Materials Science (2006), Volume 41, pp 823–839

19. T. Hinoki, L.L. Snead, Y. Katoh, T. Nozawa, A. Kohyama, A. Hasegawa **"The effect of high dose/high temperature irradiation on high purity fibres and their Silicon Carbide Composites"**, Journal of Nuclear Materials (2002), Volumes 307-311, pp 1157-1162

20. L.R. Dharani, "**Analysis of a Ceramic Matrix Composite Flexure Specimen**", Thermal and Mechanical Behaviour of Metal Matrix and Ceramic matrix Composites, ASTM STP 1080, J.M. Kennedy, H.H. Moeller, W.S. Johnson, Eds., American Society for Testing and Materials (1990), Philadelphia, pp 87-97

21. Data from Accuratus SiC wafer product can be found at **http://accuratus.com/silicar.html (last accessed 30/10/2013)**

22. SCS-6 Brand fibre details can be found from the Speciality Materials Inc. commercial website; **http://www.specmaterials.com/siliconcarbidefiber.htm (accessed 05/06/2013)**

23. Sigma Brand fibre details can be found from the TISICS Ltd. Website; **http://www.tisics.co.uk/fibre.htm (last accessed 30/10/2013)**

24. L.L. Snead, M.C. Osborne, R.A. Lowden, J. Strizak, R.J. Shinavski, K.L. More, W.S. Eatherly, J. Bailey, A.M. Williams, **"Low dose irradiation performance of SiC interphase SiC/SiC composites"**, Journal of Nuclear Materials (1998), Volume 253, pp 20-30

25. Y. Katoh, Hashimoto, Kondo, L.L. Snead, A. Kohyama, **"Microstructural development in cubic silicon carbide during irradiation at elevated temperatures"**, Journal of Nuclear Materials (2006), Volume 351, pp 228-240

26. W. Yang, H. Araki, A. Kohyama, Q. Yang, T. Noda, "**Effects of Heat Treatment on the Microstructure and Flexural Properties of CVI-Tyranno-SA/SiC Composite**", Ceramics International (2007), Volume 33, pp 141-146

27. S. Kondo, T. Koyanagi, T. Hinoki, "**Development and Testing of Ion-Irradiation under the Applied Stress for Nuclear Ceramics**", Materials Science and Engineering (2011), Volume 18, Symposium 10

28. H.T. Keng S.W. Li, S.W. Wu, K. Ji-Jung, C. Fu-Rong, Y. Katoh, A. Kohyama , "**Cavity formation in Tyranno-SA SiCf/SiC composite irradiated with multiple-ion beam at elevated temperatures**", Journal of Nuclear Materials (2007), Volumes 367–370, pp 753–757

29. T. Nozawa, T. Hinoki, L.L. Snead, Y. Katoh, A. Kohyama, "**Neutron irradiation effects on high-crystallinity and near-stoichiometry SiC fibers and their composites**", Journal of Nuclear Materials (2004) , Volumes 329–333, pp 544–548

30. G. Newsome, Lance L. Snead, T. Hinoki, Y. Katoh, D. Peters, "**Evaluation of neutron irradiated silicon carbide and silicon carbide composites**", Journal of Nuclear Materials (2007) , Volume 371, pp 76–89

31. S. Miwa, A. Hasegawa, T. Taguchi, N. Igawa, K. Abe, "**Cavity Formation in a SiC/SiC Composite under Simultaneous Irradiation of Hydrogen, Helium and Silicon Ions**", Materials Transactions (2005), Volume 46, Issue 3, pp 536-542

32. L.L. Snead, S.J. Zinkle, D. Steiner, "**Radiation induced microstructure and mechanical property evolution of SiC/C/SiC composite material**s" Journal of Nuclear Materials (1992), Volumes 191-194, pp 560-565

33. G. Simon and A. R. Bunsell, "**Mechanical and structural characterisation of Nicalon SiC fibres up to 1300°C**", Composites Science and Technology (1986), Volume 27, pp 157-171

34. Y. Katoh, L.L. Snead, T. Nozawa, S. Kondo, J. T. Busby, **"Thermophysical and mechanical properties of near-stoichiometric fiber CVI SiC/SiC composites after neutron irradiation at elevated temperatures"**, Journal of Nuclear Materials (2010), Volume 403, pp 48-61

35. R. Scholz, "**Deuteron irradiation creep of chemically vapor deposited silicon carbide fibers**", Journal of Nuclear Materials (1998), Volume 254, pp 74–77

36. S. Miro, J.M. Costantini, J. Haussy, L. Beck, S. Vaubaillon, S. Pellegrino, C. Meis, J.J. Grob, Y. Zhang, W.J. Weber, **"Nuclear Reaction Analysis of Helium Migration in Silicon Carbide"**, Journal of Nuclear Materials (2011), Volume 415, pp 5-12

37. D. Peter, F. Otto, T. Depka, P. Nörtershauser, G. Eggeler, "**High Temperature Test Rig for Inert Atmosphere Miniature Specimen Creep Testing**", Mat.-wiss. u.Werkstofftech.(2011), Volume 42, Issue 6, pp 493–499

38. M.F. Beaufort, E. Oliviero, M.L. David, A. Declémy, C. Blanchard, E. Ntsoenzok, J.F. Barbot, "**Defects induced by high energy helium implantation in 4H-SiC**", Journal Nuclear Instrumentation and Methods B (2002), Volume 186, pp 218-222

39. L. Charpentier, M.Balat-Pichelin, F.Audubert, "**High temperature oxidation of SiC under helium with low-pressure oxygen—Part1:Sintered α-SiC**", Journal of the European Ceramic Society (2010), Volume 30, pp 2653–2660

40. L. Charpentier, M. Balat-Pichelin, H. Glénat, E. Bêche, E. Laborde, F. Audubert, **"High temperature oxidation of SiC under helium with low-pressure oxygen—Part2: β-SiC",** Journal of the European Ceramic Society (2010), Volume 30, pp 2661–2670

41. H. Liu, H. Cheng, J. Wang, G. Tang, R. Che, Q. Me, **"Effects of the fiber surface characteristics on the interfacial microstructure and mechanical properties of the KD SiC fiber reinforced SiC matrix composites",** Materials Science and Engineering: A (Nov. 2009), Volume 525, Issues 1–2, pp 121–127

42. L.L. Snead, M.C. Osborne, R.A. Lowden, J. Strizak, R.J. Shinavski, K.L. More, W.S. Eatherly, J. Bailey, A.M. Williams**, "Low dose irradiation performance of SiC interphase SiC/SiC composites**", Journal of Nuclear Materials (1998), Volume 253, pp 20–30

43. S. Bertrand, R. Pailler, and J. Lamon, "**Influence of Strong Fiber/Coating Interfaces on the Mechanical Behavior and Lifetime of Hi-Nicalon/(PyC/SiC)n/SiC Minicomposites**", Journal of the American Ceramic Society (April 2001), Volume 84, Issue 4, pp 787–794

44. K., T. Hinoki, H. Kishimoto, A. Kohyama, **"Enchanced high-temperature performances of SiC/SiC composites by high densification and crystalline structure**", Composites Science and Technology (2011), Volume 71, pp 326–332

45. S. Kondo, T. Hinoki, A. Kohyama, **"Effects of Dual-Ion Irradiation on the Swelling of SiC/SiC Composites"**, Materials Transactions (2005), Volume 46, pp 1923-1927

46. R.S. Nelson, D.J. Mazey and J.A. Hudson, **"The Use of Ion Accelerators to Simulate Fast-Neutron Induced Voidage in Metals"**, Journal of Nuclear Materials (1970), Volume 37, pp 1-12
47. H. Kishimoto, K. Ozawa, O. Hashitomi, A. Kohyama, "**Microstructural evolution analysis of NITE SiC/SiC composite using TEM examination and dual-ion irradiation**", Journal of Nuclear Materials (2007), Volumes 367-370, Part A, pp 748-752

48. R. Gerhardt, "**Properties and Applications of Silicon Carbide**", published by Intech, (April 2011), ISBN 978-953-307-201-2

49. H. Pierson, "**Handbook of Refractory Carbides and Nitrides**", William Andrew Publishing (Dec. 1996), ISBN-13: 978-0815513926

50. R. Riedel, I. Chen, "**Ceramics Science and Technology, Volume 2, Materials and Properties**", published by Wiley-VCH (2010), ISBN: 978-3-527-31156-9

51. G.S. Was, "**Fundamentals of Radiation Materials Science: Metals and Alloys**", published by Springer (July 2007), ISBN-10: 3540494715

52. M. Alonso, E. Finn, "**Physics**", published by Prentice Hall (May 1992), ISBN-13: 978-0201565188

53. Formula for surface stress in flexure tests and source for standard geometry taken from; "**Standard Test Method for Flexural Strength of Advanced Ceramics at Ambient Temperature**", ASTM C1161 − 02c

54. J. J. Kruzic and R. O. Ritchie, "**Determining the Toughness of Ceramics from Vickers Indentations Using the Crack-Opening Displacements: An Experimental Study**", Journal American Ceramic Society (2003), Volume 86, Issue 8, pp 1433-36

55. W. Oliver, G. Pharr, "**An improved technique for determining hardness and elastic modulus using load and displacement sensing indentation experiments**", Journal of Nuclear Materials (1992), Volume 7, Issue 6, pp 1564-1583

56. R. Leveque, "**Finite Difference Methods for Ordinary and Partial Differential Equations: Steady-State and Time-dependent Problems**", Society for Industrial and Applied Mathematics (Sep 2007), ISBN-13: 978-0898716290

57. The TRIM/SRIM programs, created by J.F. Ziegler, together with extensive associated background information are available at **www.srim.org** (Accessed 22/07/2013)

58. The COMSOL Multiphysics program can be obtained through the COMSOl Ltd. website at **http://www.uk.comsol.com/** (Accessed 01/08/2013)

59. H. Wang, X. Zhou, J. Yu, Y. Cao, R. Liu, "**Fabrication of SiCf/SiC Composites by Chemical Vapor Infiltration**", Materials Letters (2010), Volume 64, pp 1691-1693

60. A. Okada, "**Ceramic-Matrix Composites**", Handbook of Advanced Ceramics (Ed. By S. Somiya et al) (2003), Volume 2, Chapter 15.1, pp 417-443

61. W. Honglei, Z. Xingui, Y. Jinshan, C. Yingbin, L. Rongjun, "**Microstructure, mechanical properties and reaction mechanism of KD-1 SiC$_f$/SiC composites fabricated by chemical vapor infiltration and vapor silicon infiltration**", Materials Science and Engineering: A (March 2011), Volume 568, Issue 6, pp 2441-2445

62. B. Dodson, **"Weibull Analysis"**, published by ASQA/Quality Press (1995), ISBN-13: 978-0873892957

63. T. Taguchi, T. Nozawa, N. Igawa, Y. Katoh, S.Jitsukawa, A. Kohyama, T. Hinoki, L.L. Snead, "**Fabrication of advanced SiC fiber/F-CVI SiC matrix composites with SiC/C multi-layer interphase**", Journal of Nuclear Materials (2004), Volumes 329–333, pp 572–576

64. Y. Katoh, A. Kohyama, T. Nozawa, M. Sato "**SiC/SiC composites through transient eutectic-phase route for fusion applications**" Journal of Nuclear Materials (Dec 2003), Volumes 329–333, Part A, pp 587–591

65. National University of Defence Technology **http://english.nudt.edu.cn/**

66. "**Standard Test Method for Tensile Strength and Young's Modulus of Fibers**" ASTM C 1557 – 03 (2013)

67. G. F. Knoll, "**Radiation Detection and Measurement**", published by John Wiley and Sons, ISBN-13: 978-0470131480

68. J. Nagakawa, S. Uchioa, Y. Murasea, N. Yamamotoa, K. Shibac, "**Creep Behaviour of the F82H Steel Under Irradiation with 17 MeV Protons at 300°C**", Journal of Nuclear Materials (2009), Volumes 386-388, pp 264-267

69. Image obtained from **http://www.carroll-ramsey.com/turku.pdf** (Accessed 23 July 2013)

70. H. Tenailleau, X. Bourrat, R. Naslain, "**TEM/EELS Characterization of a Sintered Polycrystalline Silicon Carbide Fiber**", Journal of American Ceramics Society (1998), Volume 81, Issue 8, pp 2037–2044

71. The homepage of the Carborundum Company can be found at **http://www.carborundumabrasives.com/** (accessed 10/11/2013)

72. L.L. Snead, Y. Katoh, A. Kohyama, J.L. Bailey, N.L. Vaughn, R.A. Lowden "**Evaluation of neutron irradiated near-stoichiometric silicon carbide fiber composites**", Journal of Nuclear Materials (2000), Volumes 283-287, pp 551-555

73. D. Hull, "**Introduction to Dislocations 2nd Edition**", published by Pergamon Press Ltd., ISBN-13: 978-0080181288

74. The homepage of the Micro Materials company can be found at **http://www.micromaterials.co.uk/** (accessed 10/11/2014)

9. APPENDICES

9.1. Appendix A: TRIM Calculations for Radiation Damage Induced by Alpha Particles and Protons at Energies from 100 KeV to 12 MeV

The full TRIM modelling outputs produced are compiled in this appendix.

100 KeV Protons in SiC

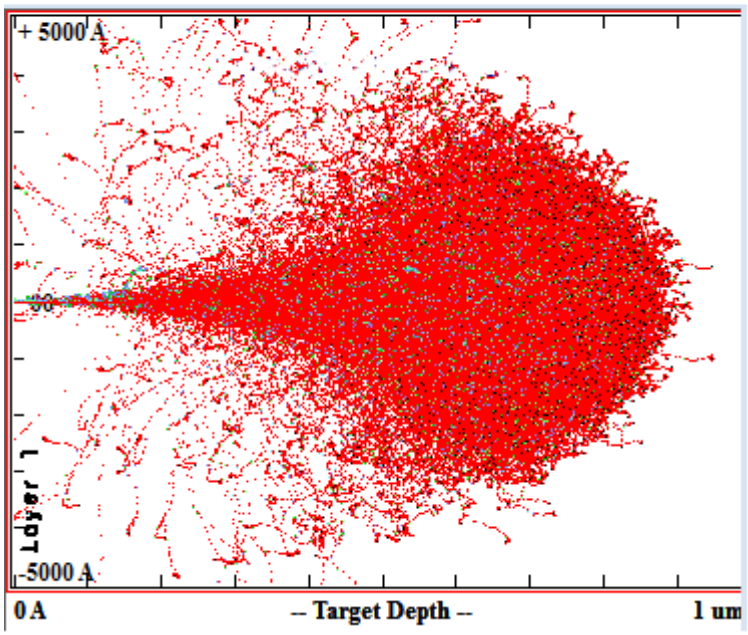

Figure i
Proton paths through SiC starting with an infinitely thin beam using TRIM. Around 4000 simulated proton paths are shown, the average penetration is 0.85 μm.

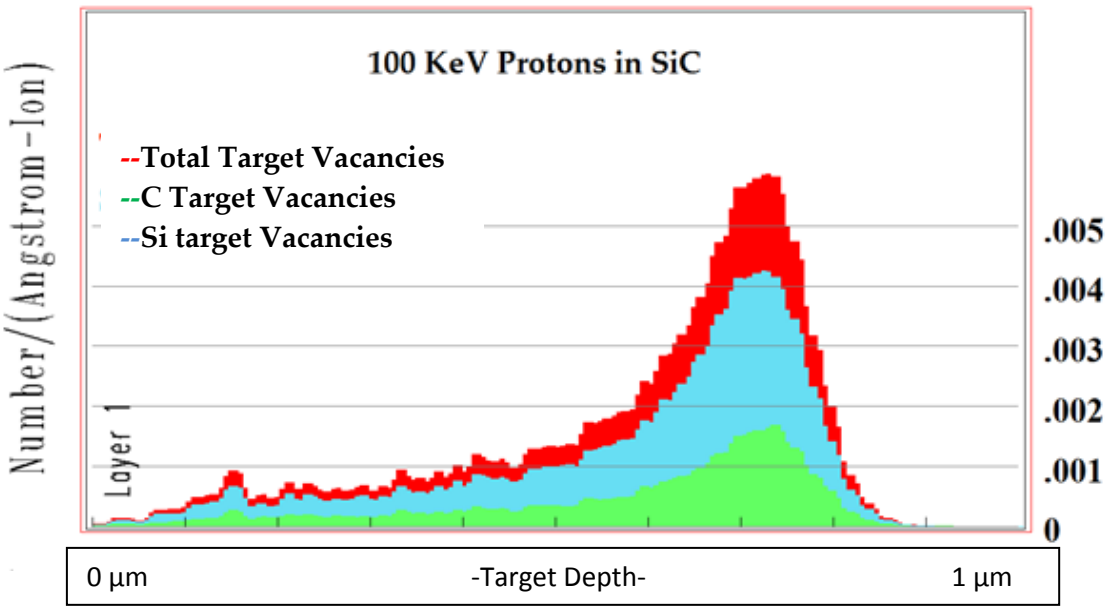

Figure ii
Damage as function of depth through SiC for 100 KeV protons.

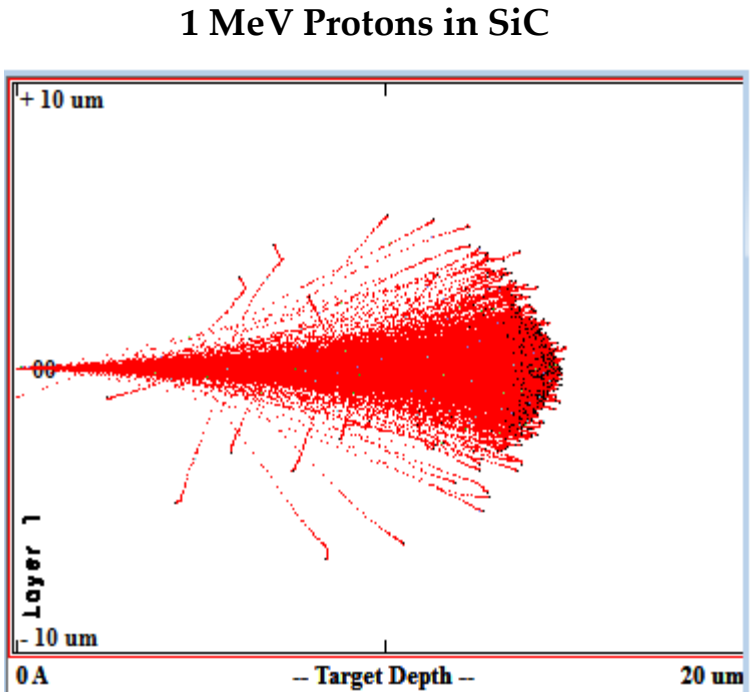

Figure iii
1 MeV proton paths through SiC starting with an infinitely thin beam using TRIM. Around 4000 simulated proton paths are show, the average penetration is 14 µm.

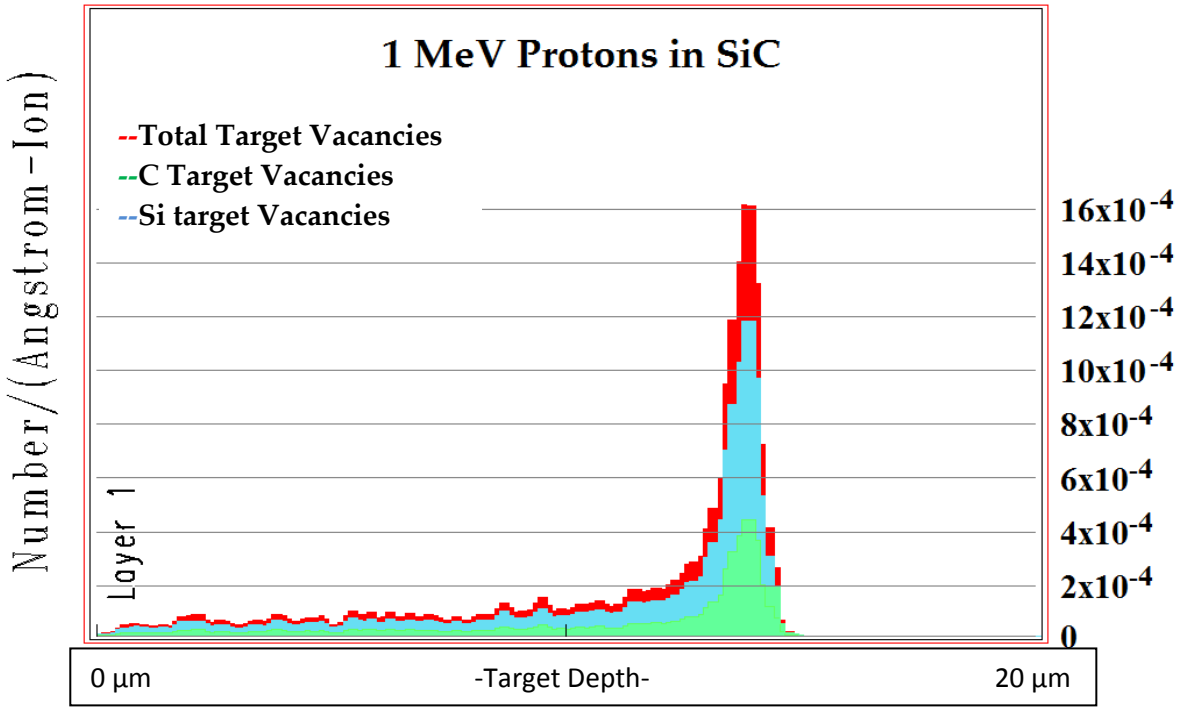

Figure iv
Damage as function of depth through SiC for 1 MeV protons.

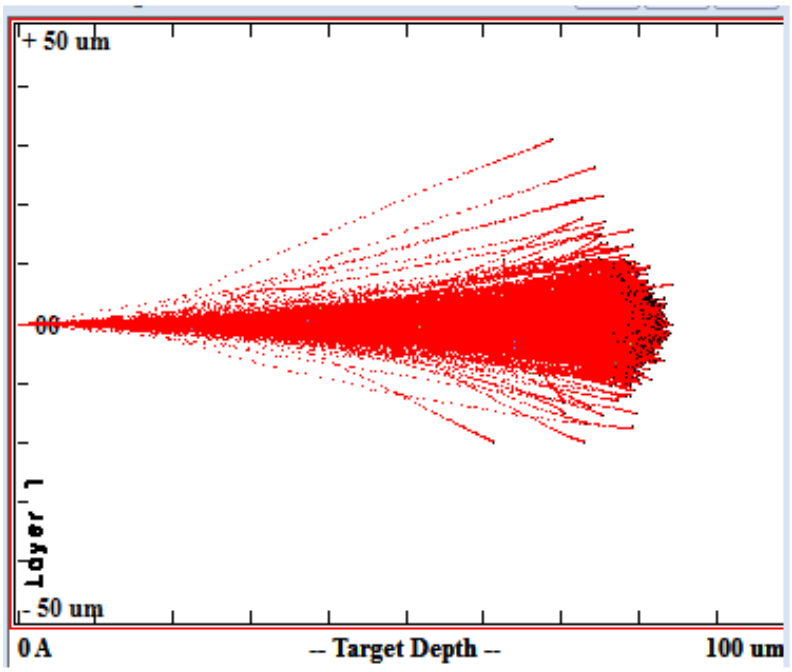

Figure v
3 MeV proton paths through SiC starting with an infinitely thin beam using TRIM. Around 4000 simulated proton paths are shown, the average penetration is 81 µm.

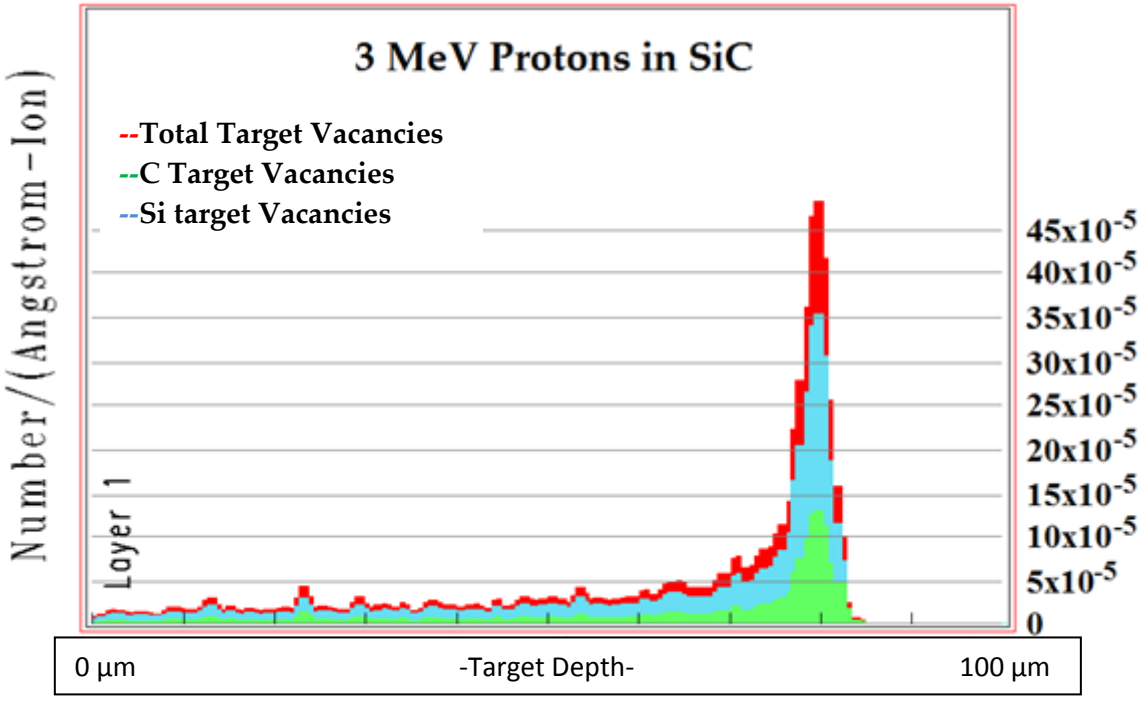

Figure vi
Damage as function of depth through SiC for 3 MeV protons.

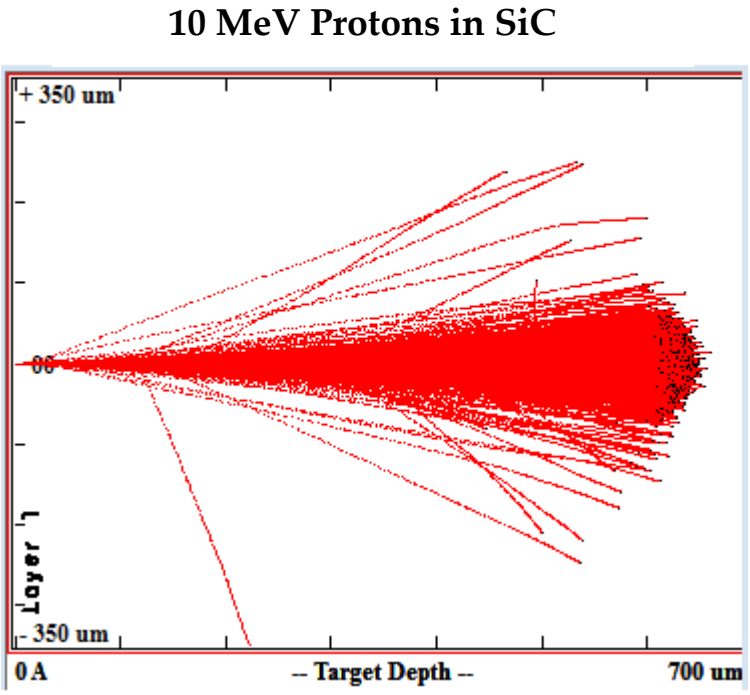

Figure vii
10 MeV proton paths through SiC starting with an infinitely thin beam using TRIM. Around 4000 simulated proton paths are shown, the average penetration is 630 µm.

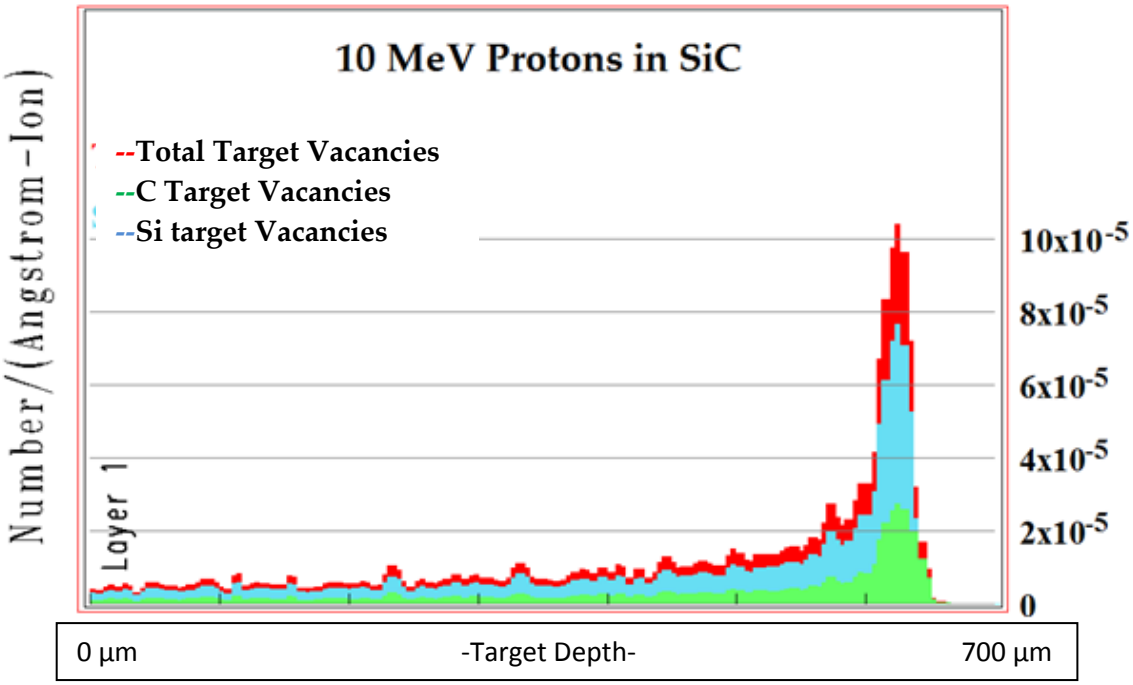

Figure viii
Damage as function of depth through SiC for 10 MeV protons.

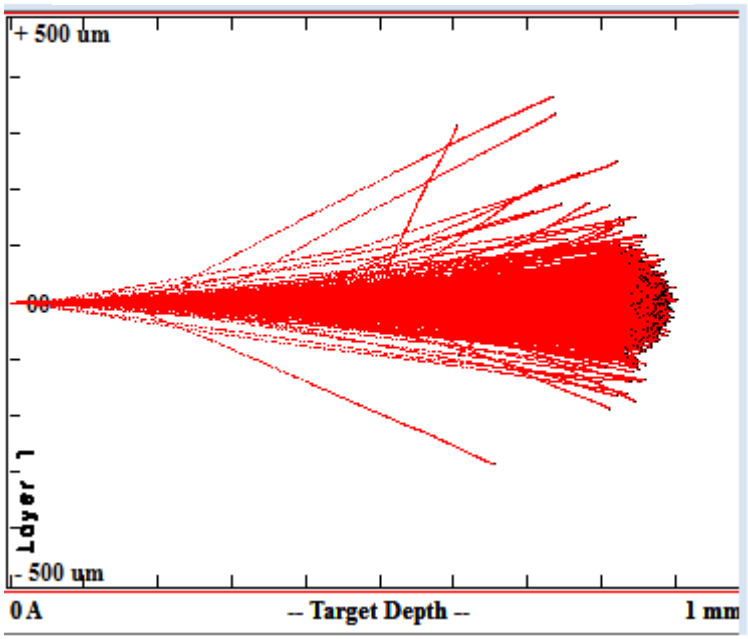

Figure ix
12 MeV proton paths through SiC starting with an infinitely thin beam using TRIM. Around 4000 simulated proton paths are shown, the average penetration is 870 μm.

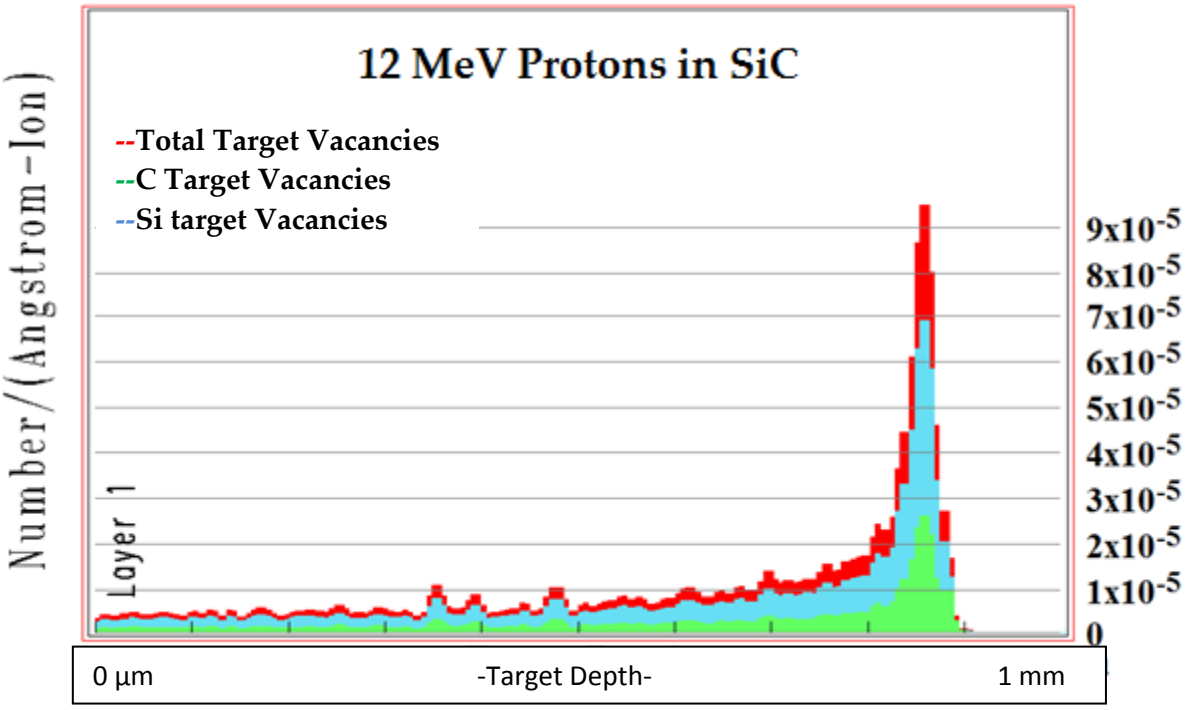

Figure x
Damage as function of depth through SiC for 12 MeV protons.

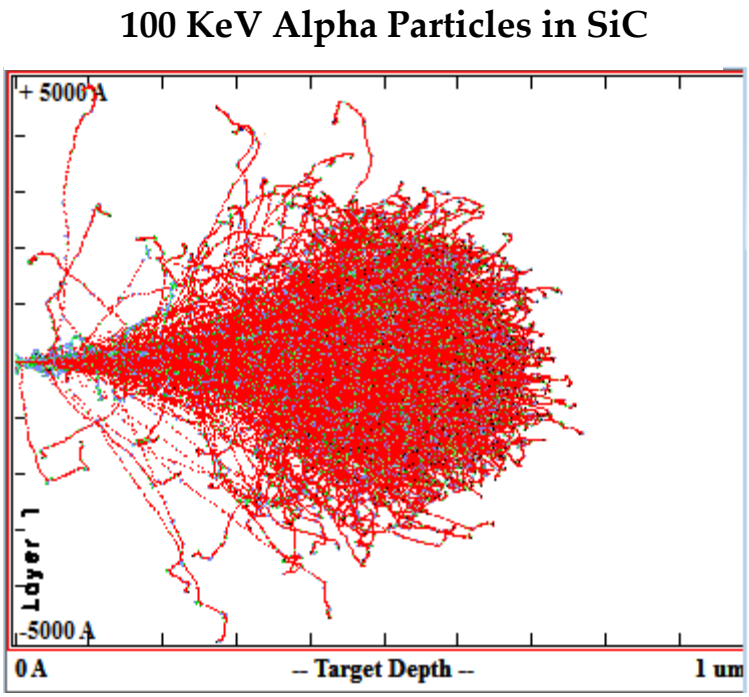

Figure xi
100 KeV alpha particle paths through SiC starting with an infinitely thin beam using TRIM. Around 4000 simulated proton paths are show, the average penetration is 0.7 µm.

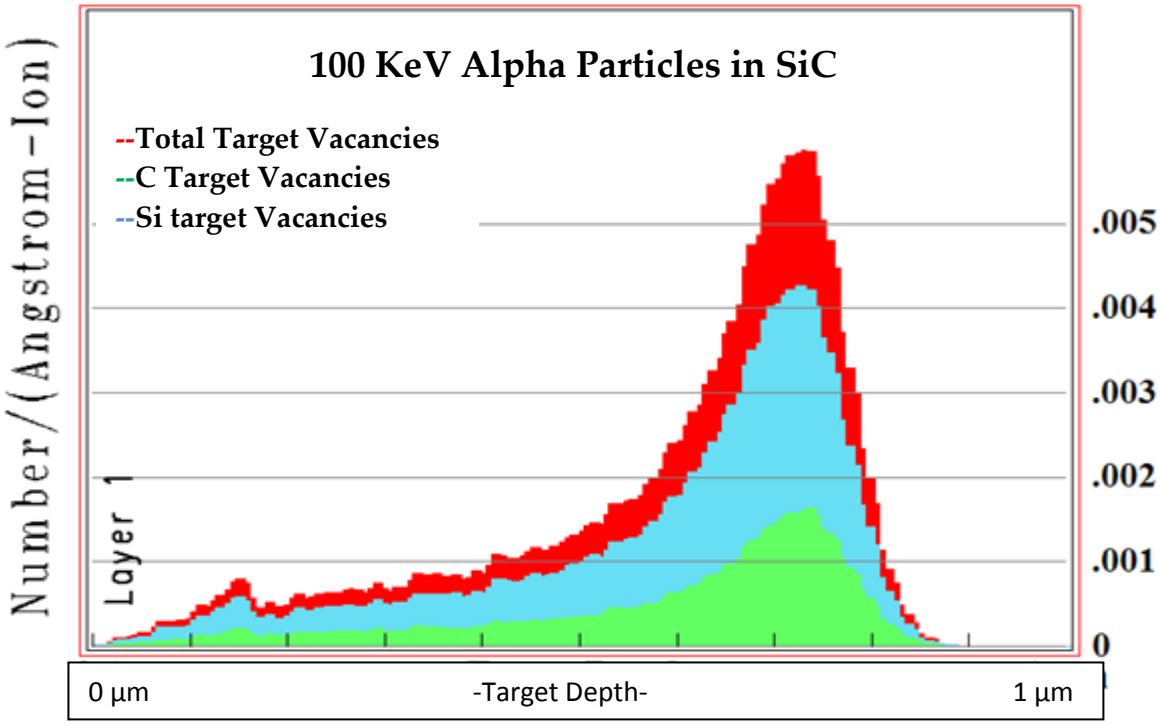

Figure xii
Damage as function of depth through SiC for 100 KeV alphas.

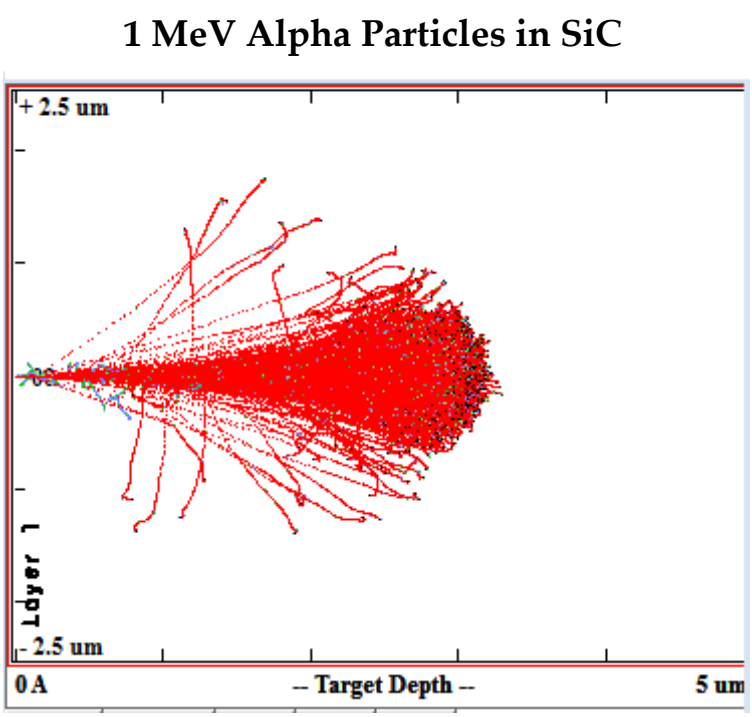

Figure xiii
1 MeV alpha particle paths through SiC starting with an infinitely thin beam using TRIM. Around 4000 simulated proton paths are shown, the average penetration is 3 µm.

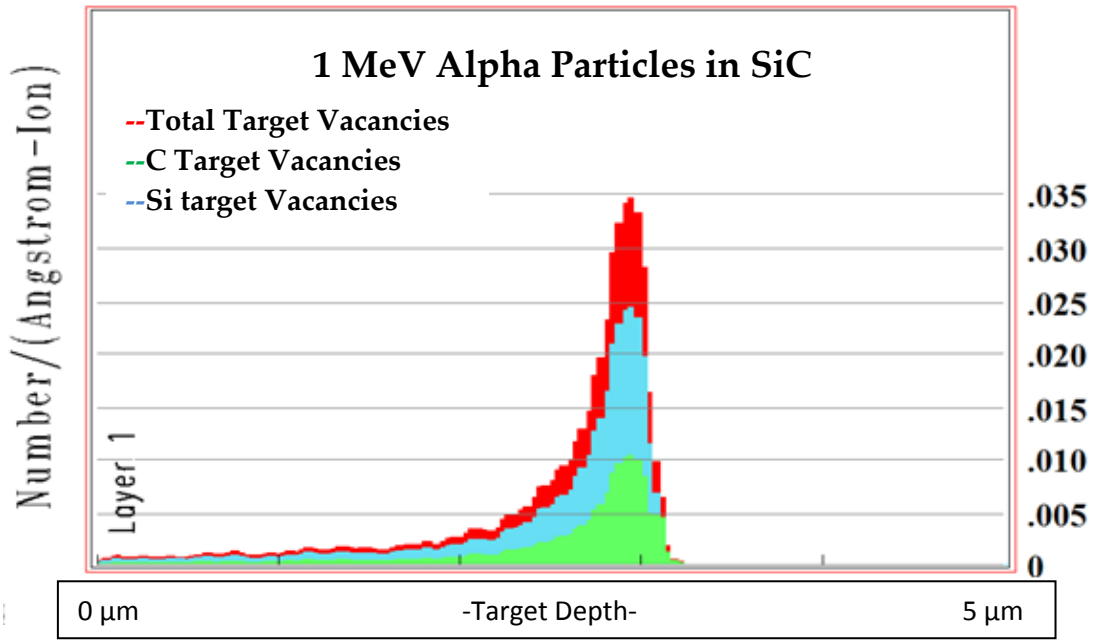

Figure xiv
Damage as function of depth through SiC for 1 MeV alphas.

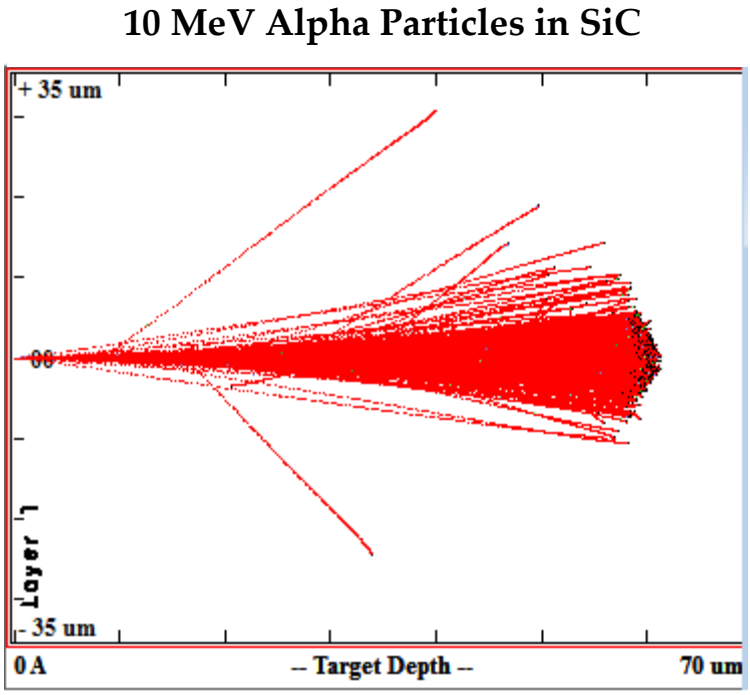

Figure xv
10 MeV alpha particle paths through SiC starting with an infinitely thin beam using TRIM. Around 4000 simulated proton paths are shown, the average penetration is 60 µm.

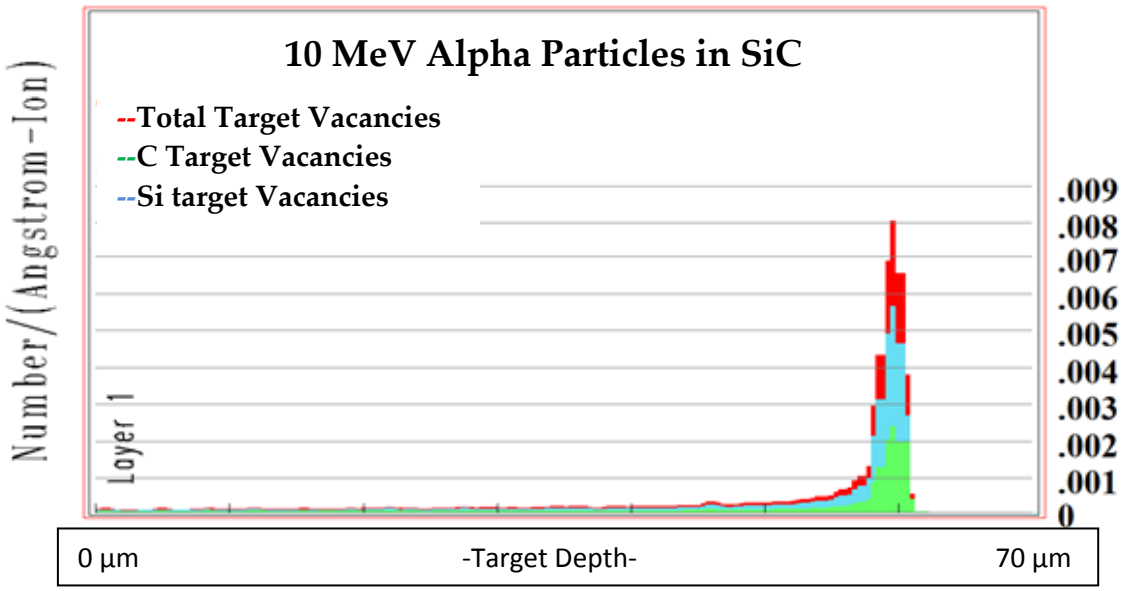

Figure xvi
Damage as function of depth through SiC for 10 MeV alphas.

9.2. Appendix B: Fracture Toughness by Vickers Indentation

101 indents were taken on irradiated hot pressed α-SiC (with approximately 0.0007 dpa at the surface) and 43 indents on non-irradiated hot pressed α-SiC, which are enumerated in table i.

Table i

Here irradiated vs non-irradiated data are compared for hot pressed α-SiC. For the irradiated specimen, fracture toughness was estimated using the crack length when visible (this is why come entries are left blank).

Irradiated Hot Pressed α-SiC					Non-Irradiated Hot Pressed α-SiC		
Test Point	1st Diagonal (μm)	2nd Diagonal (μm)	Hardness HV0.1 kgf	*Fracture Toughness (Mpa m$^{0.5}$)*	1st Diagonal (μm)	2nd Diagonal (μm)	Hardness HV0.1 kgf
1	8.8	8.8	2380	3.2	7.9	8.4	2770
2	9.0	9.1	2280	2.7	7.3	7.1	3570
3	8.3	8.7	2560	3.2	8.3	8.3	2680
4	9.2	9.4	2150	2.7	8.2	8.4	2680
5	9.5	9.1	2150	1.9	8.4	8.8	2490
6	8.3	7.8	2860	2.7	9.4	9.7	2040
7	8.4	8.6	2560	3.2	7.4	7.3	3440
8	9.0	9.4	2210	3.2	7.7	7.8	3110
9	8.7	8.8	2410	2.2	7.8	8.4	2820
10	7.3	7.8	3270	3.2	7.3	7.4	3440
11	7.5	7.4	3330	2.4	7.8	7.9	3000
12	8.1	7.9	2910	3.2	7.3	7.7	3330
13	8.3	8.2	2730	4.1	8.3	8.3	2680
14	7.3	7.1	3570	1.9	7.5	7.4	3330
15	7.7	7.7	3160	2.9	7.4	7.0	3570
16	8.1	7.7	3000	2.7	7.9	8.2	2860
17	8.1	8.1	2860		8.4	8.7	2520
18	7.7	7.7	3160	4.1	7.7	8.2	2960
19	7.8	8.2	2910		7.1	7.7	3380
20	7.1	7.3	3570	2.7	7.8	7.7	3110
21	7.7	7.9	3050	2.7	7.7	7.8	3110
22	6.9	7.0	3840	2.2	7.4	7.5	3330
23	6.9	7.7	3510	2.7	7.7	7.5	3210
24	8.3	8.1	2770	3.2	7.9	8.6	2730
25	8.6	8.4	2560		8.1	7.8	2960
26	7.7	7.8	3110	2.7	7.7	7.8	3110
27	7.7	8.3	2910	2.7	8.1	8.1	2860
28	7.9	7.7	3050	1.9	7.4	7.9	3160
29	8.3	8.2	2730	3.2	7.8	8.2	2910

Irradiated Hot Pressed α-SiC					Non-Irradiated Hot Pressed α-SiC		
Test Point	1st Diagonal (μm)	2nd Diagonal (μm)	Hardness HV0.1 kgf	*Fracture Toughness (Mpa m 0.5)*	1st Diagonal (μm)	2nd Diagonal (μm)	Hardness HV0.1 kgf
30	8.4	8.7	2520	5.4	8.4	8.6	2560
31	7.4	7.3	3440	4.7	8.2	8.3	2730
32	7.5	7.7	3210	1.9	8.1	8.2	2820
33	7.8	8.1	2960	2.7	8.3	8.4	2640
34	7.9	8.1	2910	2.4	7.3	7.4	3440
35	8.6	9.0	2410	2.7	7.7	8.2	2960
36	8.2	8.4	2680	3.2	8.4	8.7	2520
37	8.2	8.1	2820		6.9	7.7	3510
38	7.7	7.5	3210		7.5	7.4	3330
39	7.9	8.3	2820	2.2	7.7	7.8	3110
40	7.5	7.7	3210	2.2	7.5	7.8	3160
41	7.8	7.9	3000	2.7	9.0	9.4	2210
42	8.2	7.9	2860	4.1	8.1	8.2	2820
43	7.8	7.7	3110	2.7	8.1	8.2	2820
44	7.8	8.1	2960	2.2	Mean Hardness HV0.1 kgf		2970
45	8.1	7.8	2960	2.7	Sample Standard Deviation		360
46	7.9	7.7	3050	2.7			
47	7.9	7.8	3000	2.2			
48	8.2	8.4	2680	4.7			
49	8.6	8.6	2520	4.1			
50	8.1	8.3	2770	3.2			
51	7.1	7.4	3510	2.7			
52	8.4	8.3	2640	4.1			
53	7.7	7.9	3050	1.9			
54	7.9	7.9	2960	2.2			
55	8.4	8.2	2680	4.1			
56	8.8	8.4	2490	2.2			
57	7.5	7.5	3270	1.6			
58	8.6	8.4	2560				
59	7.9	8.6	2730				

Irradiated Hot Pressed α-SiC				
Test Point	Diagonal 1 (μm)	Diagonal 2 (μm)	Hardness HV0.1 kgf	Fracture Toughness (Mpa $m^{0.5}$)
60	8.2	7.9	2860	2.9
61	7.7	7.5	3210	2.7
62	8.3	8.2	2730	1.9
63	8.3	7.9	2820	4.1
64	8.4	8.3	2640	
65	8.6	8.6	2520	3.2
66	8.4	8.4	2600	2.9
67	7.3	7.4	3440	3.2
68	7.9	7.9	2960	
69	9.2	8.8	2280	3.2
70	8.2	8.1	2820	
71	7.7	7.5	3210	2.9
72	7.9	8.2	2860	5.4
73	8.1	8.3	2770	4.1
74	7.9	7.7	3050	4.1
75	7.8	8.1	2960	2.2
76	7.7	7.4	3270	3.2
77	7.4	7.5	3330	3.6
78	7.8	7.8	3050	4.1
79	8.4	8.2	2680	
80	9.0	9.0	2310	
81	8.7	9.0	2380	3.6
82	9.0	9.1	2280	3.6
83	7.4	7.5	3330	4.7
84	8.3	8.7	2560	3.6
85	7.4	7.1	3510	3.6
86	7.5	7.8	3160	3.6
87	8.1	7.9	2910	5.4
88	8.7	9.1	2340	4.1
89	7.9	7.4	3160	3.2
90	7.0	7.3	3640	4.1
91	7.4	8.1	3110	
92	7.3	7.4	3440	

Irradiated Hot Pressed α-SiC				
Test Point	Diagonal 1 (μm)	Diagonal 2 (μm)	Hardness HV0.1 kgf	Fracture Toughness (Mpa $m^{0.5}$)
93	8.3	8.2	2730	3.2
94	7.8	7.5	3160	2.7
95	7.5	7.3	3380	3.2
96	8.7	8.3	2560	4.1
97	8.4	8.8	2490	3.2
98	7.4	8.1	3110	3.6
99	7.3	7.4	3440	
100	8.3	8.6	2600	5.4
101	8.2	7.8	2910	2.7
Mean Hardness (HV0.1 kgf)			2900	
Sample Standard Deviation (HV0.1 kgf)			370	
Fracture Toughness (Mpa $m^{0.5}$)				3.2
Standard Deviation (Mpa $m^{0.5}$)				0.9

9.3. Appendix C: Tensile Test Results

Extensive results from tensile testing of thin fibres are included here for reference.

Table ii
Tensile test results of non-irradiated KD-1 fibres.

Tensile Test results for Non-Irradiated KD-1 Fibres		
Sample Number	**Force at failure (N)**	**Stress (Mpa)**
1	0.17	1110
2	0.14	940
3	0.26	1680
4	0.21	1330
5	0.27	1750
6	0.28	1820
7	0.24	1570
8	0.19	1240
9	0.14	940
10	0.19	1240
11	0.27	1760
12	0.11	710
Mean	**0.21**	**1340**
Sample Standard Deviation	**0.06**	**370**

Table iii
Tensile test results of irradiated KD-1 fibres (1 ½ hours, 1 μA, vacuum, RT).

Tensile Test results for Vacuum-Irradiated KD-1 Fibres (0.0021 dpa, 65°C)		
Sample Number	**Force at failure (N)**	**Stress (Mpa)**
1	0.23	1480.00
2	0.12	800.00
3	0.15	970.00
4	0.26	1660.00
6	0.23	1480.00
7	0.36	2340.00
8	0.24	1530.00
9	0.16	1030.00
10	0.42	2750.00
11	0.20	1280.00
13	0.29	1900.00
14	0.21	1350.00
15	0.16	1010.00
16	0.22	1430.00
18	0.26	1720.00
19	0.26	1700.00
20	0.10	670.00
Mean	**0.23**	**1480.00**
ST.Dev.s	**0.08**	**530.00**

Table iv

Force at failure and stress at failure for irradiated 1 Dose KD-1 fibre lengths tested in tension.

Irradiated 1 Dose KD-1 Fibre		
Sample Number	**Force at failure (N)**	**Stress (Mpa)**
1	0.31	1600
2	0.51	2590
3	0.49	2480
4	0.32	1620
5	0.37	1880
6	0.4	2060
7	0.51	2610
8	0.48	2430
9	0.31	1590
10	0.31	1600
11	0.31	1560
12	0.61	3090
13	0.53	2680
14	0.44	2220
15	0.31	1580
16	0.49	2500
17	0.59	3000
Average	**0.43**	**2180**
Sample Standard Deviation	**0.1**	**530**

Table v

Force at failure and stress at failure for irradiated 2 Doses KD-1 fibre lengths tested in tension.

Irradiated 2 Dose KD-1 Fibre		
Sample Number	**Force at failure (N)**	**Stress (Mpa)**
1	0.37	1880
2	0.29	1470
3	0.57	2890
4	0.36	1830
5	0.5	2530
6	0.2	1020
7	0.36	1820
8	0.44	2230
9	0.5	2560
10	0.56	2850
11	0.39	1980
12	0.53	2690
13	0.37	1900
14	0.32	1610
15	0.34	1720
16	0.14	700
17	0.51	2620
18	0.44	2240
19	0.56	2840
Average	**0.41**	**2070**
Sample Standard Deviation	**0.12**	**620**

Table vi
Tensile test results of non-irradiated Nicalon fibres.

Non-Irradiated Nicalon Fibre		
Sample Number	**Force at failure (N)**	**Stress (Mpa)**
1	0.39	2510
2	0.63	4070
3	0.4	2600
4	0.71	4640
5	0.69	4480
6	0.54	3530
7	0.45	2930
8	0.7	4530
9	0.59	3810
10	0.67	4330
11	0.3	1930
12	0.3	1930
13	0.48	3120
14	0.51	3340
15	0.43	2820
16	0.61	3980
17	0.8	5190
18	0.88	5710
Mean	**0.56**	**3640**
Sample Standard Deviation	**0.17**	**1080**

9.4. Appendix D: Nanohardness Indentation Results

The following tables summarise the data extracted from curves for load vs compression output by the nanoindenter from testing LPVCS and PCS composite samples.

Table vii
Results from nanoindentations on fibre faces of non-irradiated LPVCS fibre indents.

Indent	Max. Depth (nm)	Plastic Depth (nm)	Max. Load (mN)	Hardness (Gpa)	Contact Compliance (nm/mN)	Plastic Work (nJ)	Elastic Work (nJ)
1	668.4	451.4	100.05	15.7	2.9	8.1	16.8
2	784	586.7	100.05	9.6	2.6	13.1	16.4
3	642	435.2	100.05	16.8	2.8	8.2	15.7
4	733.2	520	100.05	12.1	2.8	8.1	17.2
5	708.9	490.8	100.05	13.5	2.9	8.5	17.3
Mean Value	707.3	496.8	100.05	13.5	2.8	9.2	16.7
Error	55.5	60.2	4E-06	2.9	0.1	2.2	0.6

Table viii
The nanohardness tester recorded the following results for air irradiated (0.0007 dpa, 5 hours at 1μA, 400°C) LPVCS fibre indents.

Indent	Max. Depth (nm)	Plastic Depth (nm)	Max. Load (mN)	Hardness (Gpa)	Contact Compliance (nm/mN)	Plastic Work (nJ)	Elastic Work (nJ)
1	649.1	434.8	100.05	16.9	2.9	7.8	16.4
2	777.3	553.6	100.05	10.7	3	12.7	19.3
3	804.9	583	100.05	9.7	3	8.9	20.7
4	776.5	595	100.05	9.4	2.4	11	14.8
5	731.2	520.5	100.05	12	2.8	9.6	17.4
Mean Value	747.8	537.4	100.05	11.7	2.8	10	17.7
Error	61.2	64.2	7E-06	3	0.2	1.9	2.3

Table ix
The nanohardness tester recorded the following results for non-irradiated LPVCS matrix indents.

Indent	Max. Depth (nm)	Plastic Depth (nm)	Max. Load (mN)	Hardness (Gpa)	Contact Compliance (nm/mN)	Plastic Work (nJ)	Elastic Work (nJ)
1	648.2	438.5	100.05	1	2.8	7.9	16.1
2	781.1	570.3	100.05	10.1	2.8	11	17
3	695.1	491.4	100.05	13.4	2.7	9.5	15.8
4	616.9	435.1	100.05	16.9	2.4	8.4	14.1
5	613.4	429.5	100.05	17.3	2.5	8.2	14.3
Mean Value	670.9	473	100.05	14.9	2.6	9	15.5
Errors	69.7	59.8	3E-06	3	0.2	1.3	1.2

Table x
The nanohardness tester recorded the following results for air irradiated (0.0007 dpa, 5 hours at 1μA, 400°C) LPVCS matrix indents.

Indent	Max. Depth (nm)	Plastic Depth (nm)	Max. Load (mN)	Hardness (Gpa)	Contact Compliance (nm/mN)	Plastic Work (nJ)	Elastic Work (nJ)
1	644.5	435.3	100.05	16.8	2.8	8	16.2
2	643.3	435.5	100.05	16.8	2.8	8	16
3	688.1	445.6	100.05	16.1	3.2	8	18.4
4	807.1	615.9	100.05	8.8	2.6	11.5	16.4
5	783.5	576.3	100.05	9.9	2.8	11.1	16.9
Mean Value	713.3	501.7	100.05	13.7	2.8	9.3	16.7
Error	77.45	87.4	7E-06	4	0.25	1.81	0.96

Table xi
The nanohardness tester recorded the following results for non-irradiated PCS fibre indents.

Indent	Max. Depth (nm)	Plastic Depth (nm)	Max. Load (mN)	Hardness (Gpa)	Contact Compliance (nm/mN)	Plastic Work (nJ)	Elastic Work (nJ)
1	793.1	572	100.05	10.1	3	11.7	19.2
2	747	484.8	100.05	13.8	3.5	8.3	20.1
3	795.3	586.2	100.05	9.6	2.8	11.6	17.3
4	720.5	531.9	100.05	11.6	2.5	8.9	16.5
5	899.1	663.7	100.05	7.6	3.1	7.8	20.2
Mean Value	791	567.7	100.05	10.5	3	9.7	18.7
Error	68.2	66.6	6E-06	2.3	0.4	1.9	1.7

Table xii
The nanohardness tester recorded the following results for air irradiated PCS fibre indents.

Indent	Max. Depth (nm)	Plastic Depth (nm)	Max. Load (mN)	Hardness (Gpa)	Contact Compliance (nm/mN)	Plastic Work (nJ)	Elastic Work (nJ)
1	622.1	427.3	100.05	17.4	2.6	7.8	15.1
2	1038.4	761.9	100.05	5.8	3.7	14.4	24.7
3	621.6	427.4	100.05	17.4	2.6	7.8	15.1
4	650.7	445.4	100.05	16.1	2.7	7.9	15.8
5	632.2	438.2	100.05	16.6	2.6	8.1	15
Mean Value	713	500	100.05	14.7	2.8	9.2	17.1
Errors	182.3	146.6	3E-06	5	0.5	2.9	4.3

Table xiii

The nanohardness tester recorded the following results for non-irradiated PCS matrix indents.

Indent	Max. Depth (nm)	Plastic Depth (nm)	Max. Load (mN)	Hardness (Gpa)	Contact Compliance (nm/mN)	Plastic Work (nJ)	Elastic Work (nJ)
1	755.4	553.3	100.05	10.7	2.7	12.3	16.6
2	706.5	472	100.05	14.5	3.1	10.5	18.8
3	704.8	477.2	100.05	14.2	3	9.4	18.4
4	580.1	377.8	100.05	21.9	2.7	6.8	15.9
5	770.1	586.8	100.05	9.6	2.4	12	16.1
Mean Value	703.4	493.4	100.05	14.2	2.8	10.2	17.2
Error	74.8	81.3	4E-06	4.8	0.3	2.2	1.4

Table xiv

The nanohardness tester recorded the following results for air irradiated PCS matrix indents

Indent	Max. Depth (nm)	Plastic Depth (nm)	Max. Load (mN)	Hardness (Gpa)	Contact Compliance (nm/mN)	Plastic Work (nJ)	Elastic Work (nJ)
1	574.7	404.1	100.05	19.3	2.3	7.1	13.7
2	725.8	504.6	100.05	12.8	2.9	8.8	18.7
3	704.2	532.1	100.05	11.6	2.3	9.2	13.5
4	574.4	375.6	100.05	22.1	2.6	7.2	15.8
5	666.7	482	100.05	13.9	2.5	9.2	15.8
Mean Value	649.2	459.7	100.05	15.9	2.5	8.3	15.5
Errors	71.3	66.9	3.00E-06	4.6	0.3	1.1	2.1

9.5. Appendix E: Finding Weibull Parameters

Weibull parameters were estimated using the usual method (e.g. Dodson [62]), the example of fitting non-irradiated α-SiC Vickers indentation data is included here.

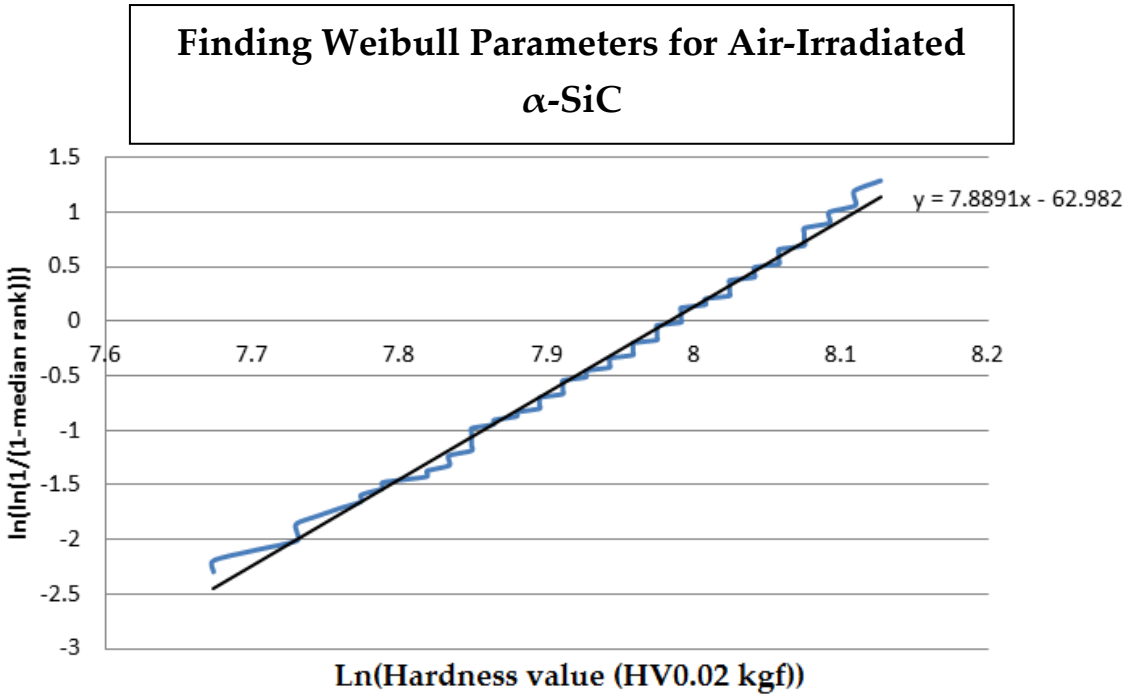

Figure xvii
Linear fit to extract Weibull parameters from irradiated α-SiC data removing the curved component of the lower x axis values.

$$\ln\left(\ln\left(\frac{1}{1-(Median\ Rank)}\right)\right) = \ln\left(\frac{x}{\alpha}\right)^{\beta} = \beta\ln(x) - \beta\ln(\alpha) = mx + c$$

$$m = \beta = 7.9;\ \ c = -\beta\ln(\alpha) = -63$$

$$\alpha = e^{\left(\frac{63}{\beta}\right)} = 2906$$

Equation i
The Weibull parameters can be extracted from the graph coefficients of figure xvii (m and c representing y=mx +c) using this method.

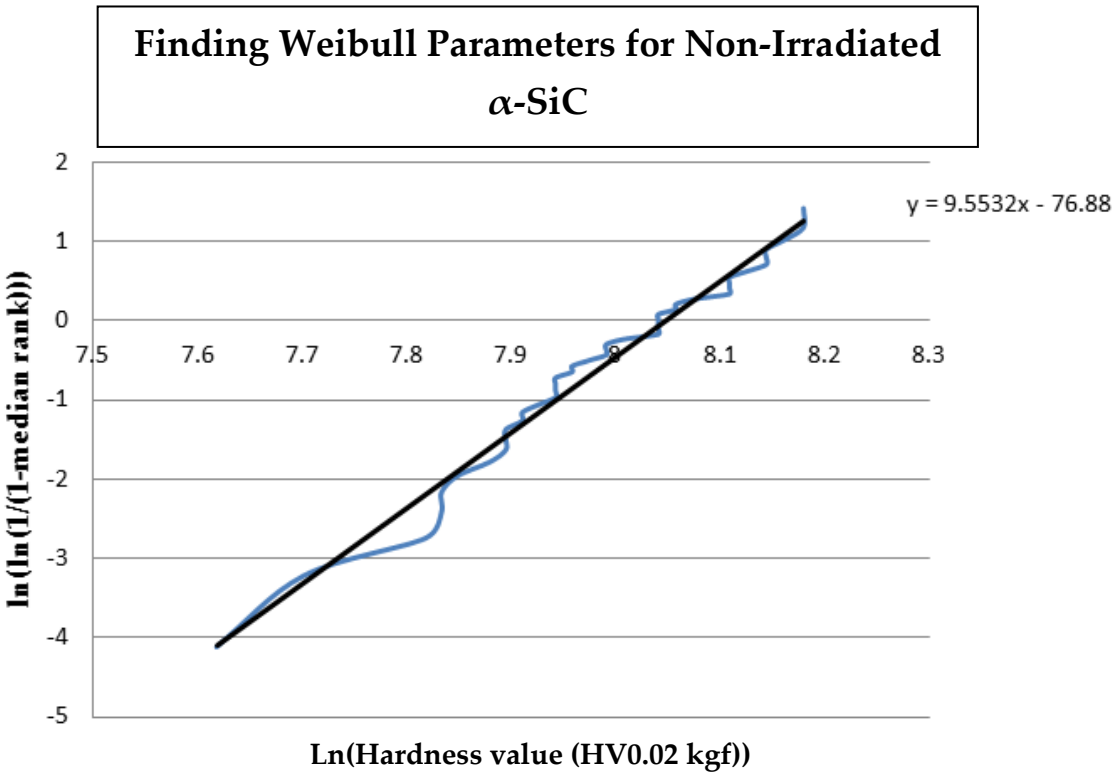

Figure xviii
Linear fit to extract Weibull parameters from non-irradiated α-SiC data.

$$\beta = 9.6;\ \beta\ln(\alpha) = 76.9$$

$$\alpha = 3012$$

Equation ii
Weibull parameters from figure xviii for non-irradiated α-SiC as per equation i.